DISSERTATION

Submitted to the
Combined Faculties for the Natural Sciences and for Mathematics
of the Ruperto-Carola University of Heidelberg, Germany

for the degree of
Doctor of Natural Sciences

Put forward by
M. Sc. Federico Amadei
Born in Sansepolcro, Italy
Date of oral examination: 25th July 2019

The physics of complex, biological interfaces and its role in the homeostatic regulation of the human gastrointestinal tract.

Referees: Prof. Dr. Motomu Tanaka
Prof. Dr. Rüdiger Klingeler

Zusammenfassung

Ziel dieser Doktorarbeit war die quantitative Untersuchung der physikalischen Zusammenhänge in den komplexen Darmgrenzflächen anhand klar definierter Modellsysteme und spezifischer experimenteller Techniken. Im Kapitel 4 wurde die Herstellung von für Nahrungsmittel geeigneten Kolloidpartikeln mittels der Vernetzung von negativ geladenem Natriumalginat durch die Diffusion von Ca^{2+} Ionen an der Öl/Wasser Grenzfläche modelliert. Durch den ersten beschriebenen Einsatz von Kleinwinkel-Röntgenstreuung mit streifendem Einfall (GISAXS-XPCS) auf diesem Gebiet wurde die zeitliche Entwicklung der Polymerkettendynamik während der Gelierung an der Wasser/Wasser Grenzfläche gemessen. Im Kapitel 5, um nachzuvollziehen, warum die an der Grenzfläche zwischen Darmschleimhaut und Lumen vorliegenden Lipidschichten größtenteils aus Phosphatidylcholin bestehen, wurde die Bedeutung grenzflächiger Wechselwirkungen zwischen verschiedenen Lipiden und Muzinproteinen durch die Kombination eines *in vitro* Schleimhautmodelles mit labelfreier Mikrointerferometrie quantitativ verglichen. Dies zeigte eindeutig, dass die Anreicherung von Phosphatidylcholin an der Grenzfläche Schleimhaut/Lumen durch die klassische Theorie elektrostatischer Wechselwirkungen nicht erklärbar ist.Im Kapitel 6 wurde der Adhäsionsmechanismus der probiotischen Bakterien an den Muzinen unter darmtypischen hydrodynamischen Scherkräften untersucht. Die dynamische Adhäsion probiotischer Bakterien wurde bei einer Schubsspannung von 0,3 Pa verbessert, was gut mit den *in vivo* Bedingungen übereinstimmt. Die erzielten Ergebnisse zeigten, dass die Kombination von *in vitro* Modellen und spezifischen experimentellen Techniken Erkenntnisse sowohl über die Strukturen, als auch die Dynamik und die an komplexen biologischen Grenzflächen stattfindenden Wechselwirkungen liefert.

Summary

The primary aim of this thesis was to quantitatively investigate the physics of complex, biological interfaces in intestines by the combination of well-defined model systems and unique experimental techniques. In Chapter 4, the formation of food colloids, *via* crosslinking negatively charged polyalginate by Ca^{2+} ions, was modeled at the o/w interface. The temporal evolution of the polymer chain dynamics during the gelation was detected by means of grazing incidence X-ray photon correlation spectroscopy (GI-XPCS) at the liquid/liquid interface for the first time. In Chapter 5, the significance of interfacial interactions between various lipids and mucin proteins was quantitatively compared by the combination of an *in vitro* mucus model and label-free microinterferometry. Remarkably, the enrichment of phosphatidylcholine at the mucus/lumen interface cannot be explained by the classical electrostatics. In Chapter 6, the mechanism of the adhesion of probiotic bacteria to the mucins was investigated under hydrodynamic shear mimicking the *in vivo* intestinal environment. The dynamic adhesion of probiotic bacteria is enhanced at the shear stress of 0.3 Pa, which showed a good agreement with *in vivo* conditions. The obtained results demonstrated that the combination of *in vitro* models together with unique experimental techniques yields the structures, dynamics, and interactions occurring at complex, biological interfaces.

„Measure what is measurable, and make measurable what is not so.”

-Galileo Galilei

To my beloved grandmother Gigliola
Wishing she were here on this special day.
To my beloved family
Sandro, Ana, Chiara, Gianluca, Viviana, and Laura.
You mean everything to me.

Affidavit for Dissertation

I hereby declare that this thesis was written only by the undersigned and without any assistance from third parties.

I hereby confirm that no sources were used, other than those indicated in the doctoral work itself.

Federico Amadei

Date: 25 July 2019

Table of Contents

Acknowledgements

There are so many people to be thanked and whom my gratitude goes to. My first and biggest "thank you" goes to my *Doktorvater* **Prof. Dr. Motomu Tanaka**. The word "supervisor" was written in German on purpose, because I have always found fascinating the way it includes the concept of "fatherhood". Indeed, **Prof. Dr. Motomu Tanaka** has been to me more than a mere supervisor: he has been a great mentor, always willing to guide me, every time I was lost; he has been a constant positive example of abnegation and a tangible evidence that hard work pays off; last but not least, he has been towards me supportive, generous, and kind, constantly encouraging me to make the best version of myself come true. To him goes my most wholehearted "thank you".

I would like to express my gratitude to my second referee **Prof. Dr. Rüdiger Klingeler** for the precious time he devoted to read, correct, and critically discuss this doctoral thesis. Together with him, I would like to thank the other members of the examination committee **Prof. Dr. Ulrich Schwarz** and **Prof. Dr. Reiner Dahint**, for the time they generously dedicated to be present today.

A very special thank goes to all my colleagues and friends from the *Arbeitskreis* Tanaka in Heidelberg, for easing my *Heimweh*:
- To **Dr. Stefan Kaufmann** for all the help he offered me in the laboratory every time I had no clue and for the good laughs we had talking about food and journeys.
- To **Dr. Maryam Eshrati**, for being such an amazing colleague and friend, with whom I have shared the sweet taste of success and the bitterness of failure, tears of joy and tears of despair. Thank you for all the great memories we collected during these four years.
- To **Dr. Wasim Abuillan**, for being a good friend, a constant source of inspiration, a great mentor and an awesome cook.
- To **Dr. Nataliya Frenkel**, **Dr. Agatha Korytovski**, **Dr. Viktoria Frank**, **Dr. Mariam Veschgini** and **Dr. Alexandra Becker**, for helping me to stand firmly on my legs, while inviting me to follow the "white rabbit" into the fascinating world of physical chemistry.
- To **Moritz Herrmann**, for being one of the greatest people I know.
- To **Dr. Benjamin Fröhlich**, **Dr. Sven Mehlhose**, **Dr. Salomé Mielke**, **Judith Thoma**, **Philipp Linke**, **Julian Czajor**, **Esther Kimmle**, **Ronja Rappold**, and **Maya Lotte** for all the good laughs, the positive vibes, the great moments we shared, and the activities we did together. My most wholehearted "Thank you" for each single time you turned my gloomy days into cheerful ones.
- To **Richard Morlang**, for his technical assistance in the lab.
- Last but not least, to **Frau Gabriele Fabry**, a tangible evidence that angels on Earth do exist.

A very special *Arigatou Gozaimasu* goes also to my colleagues and friends from the *Arbeitskreis* Tanaka in Kyoto, whom I was blessed to be able to spend two weeks with:

-To **Dr. Akihisa Yamamoto**, for being such a kind person and excellent host. I would like to express him my gratitude for travelling across the world to accompany me to Grenoble, for all the interesting discussions we had about science and other topics; for being a good friend.
-To **Dr. Ryo Suzuki**, for being such a nice person, who made my stay in Kyoto unforgettable.
- To **Shihomi Masuda**, for her free lessons of Japanese language and for her kindness.
-To **Mrs. Mieko Yoshida**, for helping me to organize my visit to Kyoto. For her smile and for her sweet thoughtfulness.

I would like to thank **Prof. Dr. Kenichi Yoshikawa**, **Prof. Dr. Suat Özbek**, **Prof. Dr. Wolfgang Stremmel** for their constructive scientific inputs during these 4 years of PhD and for the chance I was given to participate to challenging projects in a fruitful collaboration between our departments.

I also would like to express my gratitude to the members of the TROIKA02 at ID10 (ESRF, Grenoble, France). A very special thank goes to **Dr. Oleg Konovalov** and **Dr. Yuriy Chushkin**, for all the help I was given during the beam times and for making GI-XPCS at the liquid/liquid interface come true.

I also would like to acknowledge many other people that I have met during my studies at Heidelberg University:
- My dear friends **Dr. Theresa Bentele** and **Mariana Sontag-Gonzalez**, who are two incredible women, whom I had the fortune to work with on a challenging project, which eventually gave excellent results.
- My dear friend **Rebecca Wright**, for all the laughter and cheerful moments we had during lunch and coffee breaks.
- The members of the AK Spatz, our friendly neighbors, for the mutual help and support we gave each other. A special thank goes to **Dr. Tamás Haraszti**, **Dr. Chiara Zambarda**, **Dr. Rebecca Medda**, **Dr. Volker Martin** and **Dr. Carolina Diaz**, for the time they dedicated to teach me how to use new experimental instruments.
- My students **Nora Kipper**, **Sonja Christ**, **Christoph Jöst**, **Simon Büllmann**, **Rezisha Maskey**, **Iago Peters**, **Takeyuki Watanabe** and **Takaaki Kitano**, for all the good moments and knowledge we shared in the laboratory.

All of this would not have been possible without the support of the **European Union's 7th research framework program (EU FP7)**, through which I was awarded a prestigious scholarship, that granted me the honor to be part of the BIBAFOODs project as an Early Stage Researcher. I would like to express my gratitude to all the collaborators and organizers, who made BIBAFOODs come true, with a special mention to **Prof. Dr. Tommy Nylander** and **Prof. Dr. Stefan Ulvenlund** (University of Lund, Sweden), **Prof. Dr. Marité Cárdenas** (University of Malmö, Sweden), **Dr. Henriette Hansen** (University of Copenhagen, Denmark), **Prof. Dr. Björn Lindman** and **Prof. Dr. Maria Graça Miguel**

(University of Coimbra, Portugal), **Prof. Dr. Tom van de Wiele** (University of Ghent, Belgium) and **Dr. Gemma Montalvo Garcia** (University of Alcalá, Spain). Among all the people who make up the BIBAFOODs network, I would like to acknowledge:

-**Dr. Ana Rascón** (Aventure AB, Sweden), and **Dr. Ana Stenstam**, (CR Competence, Sweden), for hosting me for a period of two weeks in their companies, during which I learnt how brilliant scientific ideas can be turned into a successful business.

-**Prof. Dr. Andreea Pasc** and **Dr. Nadia Canilho** (University of Lorraine, France), for hosting me at their institution. Even if my stay was rather short, we had fruitful meetings and discussions, that helped me to get my project on track.

-**Prof. Dr. Jens Risbo** (University of Copenhagen), for hosting me in his department for a time period of two months. During this stay of intense work, I was able to deepen my knowledge, thanks to his constant guidance and mentoring.

- My dear friend **Dr. Fernanda Bianca Haffner**, for being such a smart, kind and strong woman.

- My dear friends **Dr. Çiğdem Yücel Falco** and **Dr. Francesco Cristino Falco**, for making Copenhagen become my third home.

- **Dr. Ileana Pavel**, for giving me the opportunity to come and discover the beauties of Romania.

- **Dr. Poonam Singh**, **Maria Valldeperas Badell**, **Racha El Hage**, **Dr. Surender Dhayal**, **Sofia Prazeres**, **Dr. Federica Sebastiani** and **Dr. Davide Gottardi** for the beautiful cultural exchange we had, during the winter schools across Europe.

Last but not least, this acknowledgement would be incomplete if I did not mention and express my gratitude to all my family members and friends:

-To **Ana**, **Sandro**, **Gianluca**, **Mario**, **Esperanza**, **Viviana**, **Marietto**, **Luisa**, **Laura**, **Massimo** and **Maria**.

-To **Barbara**, **Beatrice**, **Flavia**, **Giulia F**., **Giulia M**., and **Joo Yung**.

-To **Luciano**, **Evelina**, **Cristina**, **Daniela**, **Chiara**, **Udo**, **Patrick**, **Caterina**, **Janina** and **Noël**.

-To **Melih**, **Alexander**, **Sarah**, **Lalita**, **Felix**, **Angela** and **Aduh**.

Per ogni volta che ero colto dallo sconforto, e mi avete rincuorato;
Per ogni volta che ero pronto a gettare la spugna, e mi avete spronato a proseguire;
Per ogni volta che ero triste e affranto, e mi avete consolato;
Per essere stati presenti, ogniqualvolta ne avessi avuto il bisogno;
*Vi **ringrazio** dal **più profondo** del **cuore**.*

List of abbreviations

ρ	Density
η	Viscosity
Δ	Delta
Ω	Ohm
λ	Wavelength
ζ-potential	Zeta Potential
[…]	Concentration
°C	Degree Celsius
<d>	Average intermolecular distance
Å	Ångstrom
ACF	Autocorrelation Function
AFM	Atomic Force Microscopy
approx.	approximately
Au	Gold
Biotinyl Cap PE	1,2-dioleoyl-sn-glycero-3-phosphoethanolamine-N-(cap biotinyl)
BSA	Bovine Serum Albumin
Ca^{2+}	Calcium divalent cations
$CaCl_2$	Calcium Chloride
Caco2	Human epithelial colorectal adenocarcinoma cells
CFU	Colony Forming Unit
cm	Centimeter
d	Days
Da	Dalton
DAPI	4′,6-diamidino-2-phenylindole
DLS	Dynamic Light Scattering
DMEM	Dulbecco's Modified Eagle's Medium
DOPC	1,2-dioleoyl-sn-glycero-3-phosphocholine
DOPG	1,2-dioleoyl-sn-glycero-3-phospho-(1'-rac-glycerol)
DOTAP	1,2-dioleoyl-3-trimethylammonium-propane
e^-	Electron
Eq.	Equations
Eq.	Equation
ESRF	European Synchrotron Radiation Facility

FDA	Food and Drug Administration
Fig.	Figure
FITC	Fluorescein Isothiocyanate
GI-SAXS	Grazing Incidence Small Angle X-ray Scattering
h	Hours
H_2O	Water
H_2O_2	Hydrogen peroxide
HT29 MTX-(E12)	Human mucus-secreting goblet cells
Hz	Hertz
INA	Illumination Numerical Aperture
ITC	Isothermal Titration Calorimetry
keV	Kilo electron Volt
KWW	Kohlrausch-Williams-Watts
LGG	*Lactobacillus rhamnosus* GG
M	Molar Concentration
mg	Milligram
min	Minute
mL	Milliliter
mM	Millimolar
mol%	Mole percent
mrad	Milli radians
MRS	De Man, Rogosa and Sharpe agar
ms	Milli seconds
MSA	Mean Square Amplitude
M_w	Molecular Weight
NaCl	Sodium Chloride
ng	Nanogram
NH_4OH	Aqueous solution of ammonia
nm	Nanometer
NMR	Nuclear Magnetic Resonance
NP	Nanoparticle
Ø	Diameter
PA	Polyalginate
PBS	Phosphate Buffered Saline
PGPR	Polyglycerol Polyricinolate
PH	Phase Contrast
Pt	Platinum

PTFE	Polytetrafluoroethylene / Teflon
q *or* Q	Momentum Transfer Vector
QCM-D	Quartz Crystal Microbalance with Dissipation
R	Radius
r_e	Electron radius
RICM	Reflection Interference Contrast Microscopy
rpm	Revolution Per Minute
RT	Room Temperature
s	Second
SDS	Sodium Dodecyl Sulfate
SDS-PAGE	Sodium dodecyl sulfate-polyacrylamide gel electrophoresis
SiO_2	Silica (Oxide)
SLD	Scattering Length Density
TEER	Transepithelial Electric Resistance
TRIS	Tris(hydroxymethyl)aminomethane
v/v	Volume in Volume
vs.	versus
w/o	Water in Oil
WHO	World Health Organisation
wt %	Weight Percent
XPCS	X-ray Photon Correlation Spectroscopy
ZO-1	*Zonula occludens*-1
µL	Microliter

Chapter 1: Introduction

Within the entire digestive system, the human gastrointestinal tract is the largest organ in the body formed by a single layer of intestinal epithelial cells, possessing a surface area of 300 m^2.[1] The surface of gastrointestinal epithelia is exposed to an extremely high bacterial load, ranging from thousands to trillions of bacteria per mL of luminal contents from stomach to colon.[2] In intestinal epithelia, individual cells are connected by tight junctions and anchored on the basement membrane by hemidesmosomes.[3] The most abundant epithelial cells throughout the intestine are enterocytes serving as the primary surface for nutrients absorption, whose apical surface is covered with microvilli.[4] Enterocytes are interspersed by goblet cells,[5] which secrete high molecular weight glycoproteins, that are called mucins ($\sim 2 \times 10^6$ Da).[5] Mucin proteins possess one or several central domains enriched with O-linked oligosaccharides such as negatively charged sialic acid and sulfate residues, whereas the N- and C-termini are mostly non-glycosylated and even hypothesized to be hydrophobic.[6, 7]Among different mucin proteins, mucin 2 (MUC2) is a major constituent of the mucus layers that build up a protective barrier on the epithelial surfaces against pathogens and toxins.[3, 4, 8] It is notable, however, that mucin alone is not able to protect intestinal epithelia against the bacterial invasion. A mounting body of evidence has suggested that the layer of phospholipids actually serves as a protective barrier (Fig. 1.1).[9, 10] Among various phospholipids secreted in the intestinal mucus, phosphatidylcholine (PC) and lyso-phosphatidylcholine (lyso-PC) account for more than 90 %.[11] Recent studies have demonstrated that the secretion of PC and lyso-PC in luminal mucosa occurs as a result of the selective paracellular transport of PC/lyso-PC across the lateral tight junction between intestinal epithelia via cystic fibrosis transmembrane conductance regulator (CFTR).[12] Finally PC and lyso-PC bind to the surface of mucin2, which moves distally to the rectum.

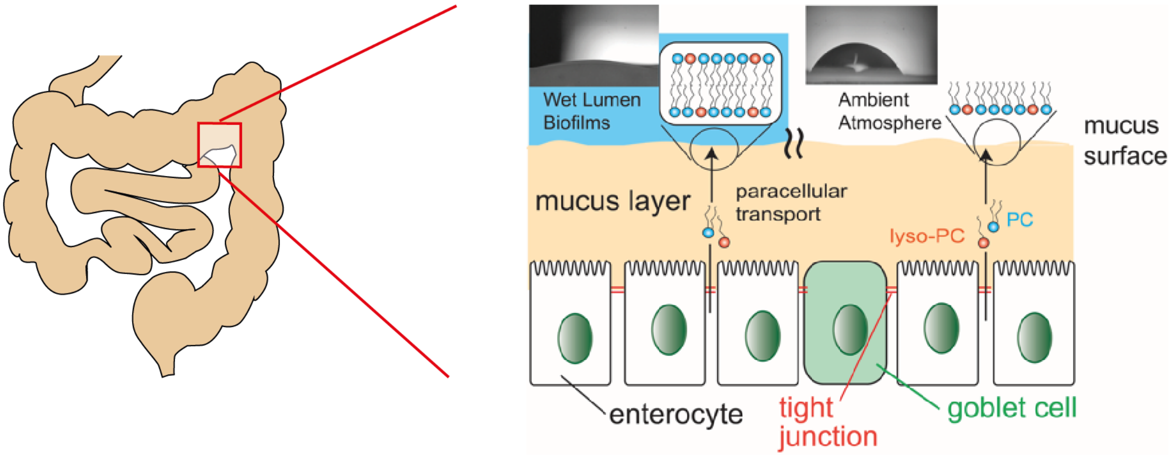

Fig. 1.1: The gastrointestinal mucus and the phospholipid barrier. The intestinal surface is coated with mucus layer, which consists of heavily glycosylated mucin proteins and lipid-based protective barriers against the attack of pathogenic bacteria. Transport of phospholipids through the tight junction in colon epithelia (goblet cells, enterocytes) and accumulation to the mucus layer surface is

schematically depicted. Establishment of the protection layer by amphiphilic lipids can be evidenced by simple contact angle measurements. The explant from rat colon epithelial tissue pre-treated with water (left) showed a very low contact angle ($\theta < 20$ °), suggesting the protection by a lipid bilayer in contact with wet lumen or biofilms. On the other hand, the same tissue exposed to an ambient atmosphere (right) exhibited a much higher contact angle ($\theta \sim 70$ °), implying the formation of a lipid monolayer. The Fig. was readapted from Korytovski et al.,[13] and Eshrati et al..[14]

It has been reported that, once the PC/lyso-PC coating is thinned or damaged by the enzymatic degradation of PCs by ectophospholipase in the colonic microbiota, these regions become the most vulnerable area for bacterial invasion.[9] In inflammatory bowel diseases, such as Crohn's disease and ulcerative colitis, PC secretion is intrinsically impaired, resulting in a 70 % reduction of its content in mucus.[11, 15] As a consequence, bacterial invasion and hence the mucosal inflammation start in the rectum and extend proximally. Moreover, although it has been reported that the supplementation of PCs by oral administration thanks to a diet rich in fats,[10] PC-releasing formulations,[16-18] or the suppression of ectophospholipase[19], re-established the physiological mucus-PC composition and inhibited mucosal inflammation, little is understood on how PC interacts with the damaged mucin. Thus, the systematic investigation of interactions between the phospholipid head groups and mucin is crucial to understand why PC/lyso-PC molecules are selectively accumulated on mucus surfaces. Recently Korytowski et al. investigated the interactions of DOPC with two preparations of mucin originating from porcine stomach, by means of DLS, ζ-potential measurement, and Langmuir isotherms, hinting that mucin was adsorbed onto the surface of DOPC vesicles. Furthermore, the enthalpy of mucin-PC interaction could be measured by ITC and it was found that the interaction between mucin and PC is strong. In order to shed light on the possible underlying mechanism to explain such a high affinity, the ITC measurements were repeated by varying systematically the net charges of the lipid polar heads. They concluded that the zwitterionic DOPC has the strongest binding affinity to mucin that *per se* cannot be explained within the framework of classical electrostatic interactions between charged molecules.[13]

Therefore, since the integrity of the whole mucus is sustained by the coating of mucin layer with phospholipid membranes, the quantitative study on the "interfacial interactions" between phospholipid layers and mucin on the mucus surface is more biologically relevant.

Together with the oral administration of an adequate amount of phospholipids, homeostasis of intestinal microbiota can be supported or improved by the oral uptake of probiotic organisms, whose metabolic activity promotes the host's health by blocking the binding sites for pathogenic bacteria[20], by secreting antimicrobial lactic acid, or by potentially displacing phospholipase-producing bacteria.[21] Since 1980s, probiotic microorganisms, such as *Lactobacillus* or *Bifidobacterium* have been used as food additives in commercial products.[22, 23] In medicine, nonpathogenic *Escherichia coli* Nissle 1917 has been used as a medical probiotics for the treatment of inflammatory bowel diseases.[24]

Towards the improvement of intestinal microbiota by the delivery of probiotics, one of the major criteria for the selection of probiotics is the adhesion to intestinal mucus surface. Although the effects of foods, digestion, and other microbiota are known to influence the adhesion *in vivo*,[25] it is relevant to quantitatively determine the adhesion strength of released probiotics to the intestinal mucus layer. To date, there have been several studies on the adhesion of probiotic bacteria to the extracted mucus.[26-29] In these studies, the mucin extracted from human fecal samples was immobilized onto the bottom of microtiter plates by physisorption at 4 °C, and the amount of radioactively labeled bacteria adherent to the surface was measured by a scintillation counter. Extending this line of investigations, it has been shown that the presence of probiotic microorganisms indeed caused a decrease in the adhesion of pathological bacteria.[30-32]

At the molecular level, a comparative genomic study suggested that LGG express pili containing a human-mucus binding protein.[33] Moreover, it has been shown that spaCBA-encoded pili play key roles in adhesion to mucin not only on extracted mucin[34] but also on the intestinal epithelia model differentiated from Caco2, which is the cell line used to mimic the enterocyte-like cells in *in vitro* studies.[35] In particular, SpaC subunit of pilus is responsible for the binding to the O-glycan of mucin,[36] as the primary SpaC pilus structure is rich of lectin-like binding domains to carbohydrates (Fig. 1).[33, 36] A more recent single molecule force spectroscopy study suggests that the interaction of LGG pilus with O-glycan is not only a simple spring-like binding, but the shear-induced unfolding strengthens the binding.[37] This finding seems plausible, as the primary structure of SpaC contains a von Willebrand factor-like domain that is known to be shear-dependent.[38] The shear-enhanced binding seems to explain how LGG can withstand the shear stresses in intestinal environments, which is typically in the range of 0.1 – 0.5 Pa.[39] However, previous adhesion studies, both on mucin physisorbed on plastic[26, 28, 29, 34] or intestinal epithelial cells,[35] have been performed in the absence of shear stresses.

Nevertheless, the delivery of probiotics via oral administration has been impeded by the substantial loss of bacterial viability due to the harsh conditions in the upper gastrointestinal tract, such as low pH in stomach and the exposure to bile acid and pancreatic phospholipases in duodenum. This problem can be overcome by microencapsulation of probiotics in polymer-based carriers have been developed using several techniques, including spray-drying, freeze-drying method, extrusion, and emulsification[40-44]

One of the most studied natural polymer capable of forming a hydrogel and therefore with a broad spectrum of applications as an encapsulating agent is sodium alginate.[45, 46] It is a natural anionic polymer extracted from marine brown algae, made of a linear chain of L-guluronic acid (G) and D-mannuronic acid (M) residues linked to each other by 1, 4-glycosidic linkages. In the presence of divalent cations (Ca^{2+}, Mg^{2+}), that act as cross-linkers, a 3D gel matrix is readily formed. To date, alginate has been used extensively in biomedicine, pharmacology and food industry.[47-52] For the latter, the development of alginate microcapsules as carriers for enzymes and microorganisms, such as probiotics, to design targeted delivery systems has been drawing increasing attention. To fulfill this purpose, several techniques have been developed. One of the most promising candidates was proven to be the emulsification technique, that has the advantages to minimize the damage inflicted to the microorganisms during the capsule synthesis and moreover to yield microcapsules with high-quality and specific standards, namely a small (ϕ ≤ 100 μm) and uniform size.[53, 54] In order to produce alginate microcapsule *via* emulsification, an aqueous solution of sodium alginate, which we refer to as the dispersed phase, is mixed into oil containing surfactant, which we refer to as the continuous phase, giving as result a w/o emulsion. In a second step, a solution containing cross-linkers, usually aqueous $CaCl_2$, is added to "break" the emulsion. This addition sets the onset of the external gelation process sustained by the fast diffusion of the Ca^{2+} ions to the interface of the alginate droplets in oil, that get entrapped within the G residues of sodium alginate and cause a dramatic increase of the bulk viscosity. Albeit the use of the emulsification technique has been extensively studied and applied for the production of sodium alginate microcapsules,[55, 56] little is known about the dynamics underlying the gelation process occurring at the w/o interface at a microscopic length scale. One explanation for this, is the intrinsic limitation in carrying out dynamic studies at the microscopic level and at the interface simultaneously. For instance, on one hand DLS studies of the turbid gel phase were impaired because of the multiple scattering effects taking place within the sample; on the other hand, X-ray studies were limited by the risk to induce radiation damage to polymer gel samples, that suffer of radiation sensitivity. Indeed, as Ruta et *al.* report,[57] these limitations have arisen as well in previous investigations conducted on other natural hydrogels, such as methylcellulose[58], due to the limited time window accessible by the experimental techniques that hindered the study of relaxation times below the order of a few seconds. Interestingly, while the structural evolution accompanying the gelation of sodium alginate in bulk and at the interface has been largely investigated via SAXS and MRI,[59-61] to the best of our knowledge, there are no studies that have been reported on the corresponding dynamics of the sol-gel transition of alginate at liquid/liquid interface at a nanometric scale.

In Chapter 4, a cutting-edge study of the out of equilibrium dynamics at the o/w interface by means of X-ray Photon Correlation Spectroscopy (XPCS) is presented, with the aim to provide new insights in the interfacial gelation of alginate.[62] To date there are no XPCS studies reported on soft materials conducted at the liquid-liquid interface, whose study still remains an open challenge. XPCS is the analogous of DLS but with coherent X-rays as those available at 3rd generation synchrotron sources. XPCS is a relatively recent technique which has already been extensively used to investigate slow dynamic processes down to nanometric and atomic length scales in complex materials like polymeric and colloidal gels,[63-66] glasses[67, 68] and concentrated colloidal suspensions[69, 70]. When applying XPCS to very soft material, such as polymeric gels and hydrogels, the major drawback is the undesired radiation damage caused by high energy X-ray beams. To circumvent the latter, a fast shutter was placed between the radiation source and the sample to reduce the source of radiation damage by drastically decreasing the exposure times. To further reduce the exposure times, silica nanoparticles were added in the alginate aqueous solution to increase the scattering signal. The use of nanoparticles as tracers of the matrix dynamics has been already successfully applied in the case of different soft materials.[57, 66, 71-74] To test the applicability of XPCS to the alginate hydrogel, first experiments in SAXS geometry were conducted to investigate the dynamics at a nanoscale level in bulk. Subsequently, a GISAXS configuration was used to test the interfacial gelation of alginate at the o/w interface. To slow down the reaction kinetics and thus to be able to follow the sol-gel transition at the o/w interface, a dispersion of $CaCl_2$ nanoparticles in vegetable oil was used. As the nanoparticles condense at the interface and the hydrogel is formed, the time evolution of the gelation kinetics was tracked.

In Chapter 5, the mechanism of how PC/lyso-PC molecules are selectively accumulated on mucus surfaces, where a barrier against colonic microbiota is generated, was investigated. To address this question, a quantitative *in vitro* model of intestine surfaces was fabricated by the coupling of mucin proteins on lipid membranes deposited on planar substrates (called supported membranes). After characterizing the model intestine surfaces, the vertical Brownian motion of 10 µm-large particles was monitored using label-free reflection interference contrast microscopy (RICM). From the height fluctuation of the particles, the effective interfacial interaction potentials and hydrodynamic frictions was calculated by analytically solving the Langevin equation of the particle fluctuation. The significance of interfacial interactions can be compared quantitatively using the spring constants, the second derivatives of potentials within the Derjaguin's approximation.[75] The first question that was addressed was whether electrostatic interactions modulate interfacial interactions at all. For this purpose, 10 µm-large latex microparticles bearing different surface charges were prepared, and it was found that the change in spring constants can be well explained within the framework of classical electrostatic interactions. Therefore, in the next step, the interaction of 10 µm-large silica particles coated with PC, cationic lipids (DOTAP), and PC membranes incorporating anionic lipids (DOPG) was examined.

In Chapter 6, the dynamic adhesion of LGG on two types of cell monolayers constituting intestinal epithelia, enterocytes and goblet cells, was investigated. Enterocytes share the most abundant population, while goblet cells play a major role in secreting mucin proteins. These two cell types were differentiated from the established cell lines, Caco2 and HT29 MTX, and the apical-basal polarization of cells by the formation of tight junctions was assessed. In the first step, we confirmed the differentiation of the two cell lines into confluent, polarized epithelial cell monolayers by transepithelial electrical resistance (TEER) measurements and the immunofluorescence staining of tight junction proteins (ZO1) using various porous polymer films as the substrates. Furthermore, the secretion of mucin by goblet cell-like HT29 MTX was also confirmed by immunofluorescence staining of MUC5AC. Since mucin is a heavily glycosylated protein forming gels, the dynamic adhesion of LGG under shear stresses is modulated not only by the specific SpaC-glycan interactions but also by the mechanical properties of mucin layers. Therefore, subsequently, we mechanically characterized the surface of cell monolayers by particle-assisted indentation, and found that the surface of goblet cell-like cells secreting mucin was approx. 30 times softer than that of enterocyte-like cells. Finally, we transferred the cell monolayer into a microfluidic chamber and investigated (i) the dynamic adhesion of LGG under physiological shear stresses and (ii) persistence of LGG adhesion against flow-induced detachment.

Chapter 2: Theoretical Background.

2.1.The human gastrointestinal tract

The digestive system of human beings consists of many and diverse organs that carry out different functions: the mouth (oral cavity and throat), esophagus, stomach, intestines (jejunum and ileum) and rectum. From a general perspective, they mainly serve to ingest, digest and transport the food through the body.[76] The biggest part of the digestive system is represented by the gastrointestinal tract (Etymology from Latin, *gaster* = stomach and *intestinum* = gut), where the digestion takes place at the greatest extent. During the passage in the gastrointestinal compartments, the food is decomposed enzymatically, nutrients and water get reabsorbed and indigestive components are excreted through the rectum.[77] The luminal pH changes within these segments from strongly acidic in the stomach (pH 1 – 2.5) to neutral or slightly alkaline in the small intestine (pH 6 – 7.9) to a slightly lower pH again in the large intestine (pH 5.2 – 7.0), as presented in Fig. 2.1.[47, 78]

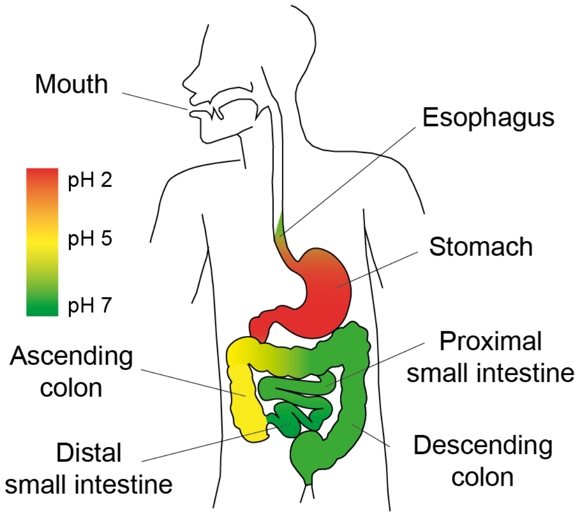

Fig. 2.1 The digestive system and its organs. The luminal pH values of the different sections making up the gastrointestinal tract are represented in a colored fashion. Fig. was adapted from Eshrati et al.,[43] Cook et al.,[47] and Khutoryanskiy et al..[78]

As shown in Fig. 2.2, the gastrointestinal wall consists of four different tissue layers: mucosa, submucosa, the muscular layer and serosa/adventitia.[79] The uppermost layer, which is the closest to the intestinal lumen, is formed by intestinal epithelial cells of mainly two types: the enterocytes and the goblet cells. On top of this epithelial tissue, a viscous substance, known as mucus, is present. The latter, plays a key role in maintaining the homeostasis of the gastrointestinal tract. The mucus is produced in the goblet cells, that are interspersed in the epithelium of the mucosa. Interestingly, the mucus is present in all organs, which are exposed and in direct contact with the external environment, for instance respiration (lungs) and digestion organs (stomach, intestine). In the intestines the mucus functions as lubricant for the transportation of substances over the intestinal membrane. Besides, it also acts as a physical barrier to protect the epithelial walls against the attack of pathogens, the degradation caused by digestive enzymes and the detriment induced by other harmful substances. However, nutrients are able to pass through the mucosa, which are eventually reabsorbed by the microvilli structure located at the apical side of the enterocytes.[80] Interestingly, over 90 % of the secreted mucus is known to be water, whereas only a small percentage consists of other substances such as salts, lipids, proteins and probiotic bacteria. The mucus flowing in the gastrointestinal tract mainly consists of glycoproteins known as mucins.[80, 81]

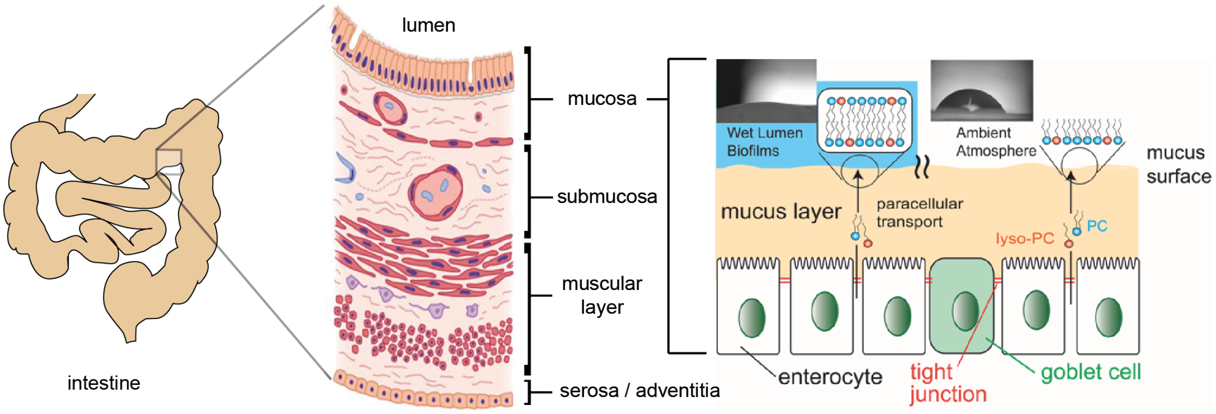

Fig. 2.2: The gastrointestinal wall and its composition. A schematic representation of the tissues that make up the gastrointestinal walls is presented. The structure of the mucosa layer, which is the most adjacent one to the lumen, is given in detail in the right-side of the Fig. It consists of a monolayer of enterocytes interspersed by goblet cells, which are responsible for the secretion of viscous proteins, that make up the mucus. The integrity of the mucus layer is sustained by the presence of a protective barrier, which is made of phospholipids. The latter adsorb to the mucus layer after paracellular transport through the tight junctions existing between adjacent epithelial cells. The Fig. was readapted from Kierszenbaum, Korytovski *et al.* and Eshrati *et al.*.[13, 14, 79]

2.1.1.The mucus and its building blocks: the mucins

The mucins are heavy macromolecules with a high molecular weight (0.5 – 29 MDa),[82] composed of a central protein, which several sugar side-chains via a glycosylic bond are attached to, as shown in Fig. 2.3. Those sugar side-chains make up around 80 % of the mucins molecular weight and besides they protect the protein against the enzymatic degradation caused by proteases (proteolysis).[83] The carbohydrate content is manly composed of N-acetylgalactosamine, N-acetylglucosamine, fucose, galactose, and sialic acid.[84] Therefore, the sugar side chains are rich in sialyl, sulfate, and hydroxyl groups that confer the mucins a strong anionic character, which is responsible for their high water binding affinity and thus their viscous and “bulky” consistence.[80] The central protein is composed of tandem repeats of serine, threonine and proline (STP repeats) and is bound through the oxygen atoms to the sugar side-chains (O-glycosylation). The amino and carboxyl terminals of the central proteins are only slightly glycosylated, but rich in cysteines, so that disulfide bridges between mucins are possible.[81] The latter enable the mucin monomers to crosslink with each other and to build, at first, dimers and afterwards more elongated and bulky structure through a series of dimerization reactions. Interestingly, each organism produces different types of mucins. To date, twenty human mucin genes have already been characterized in total.[85]

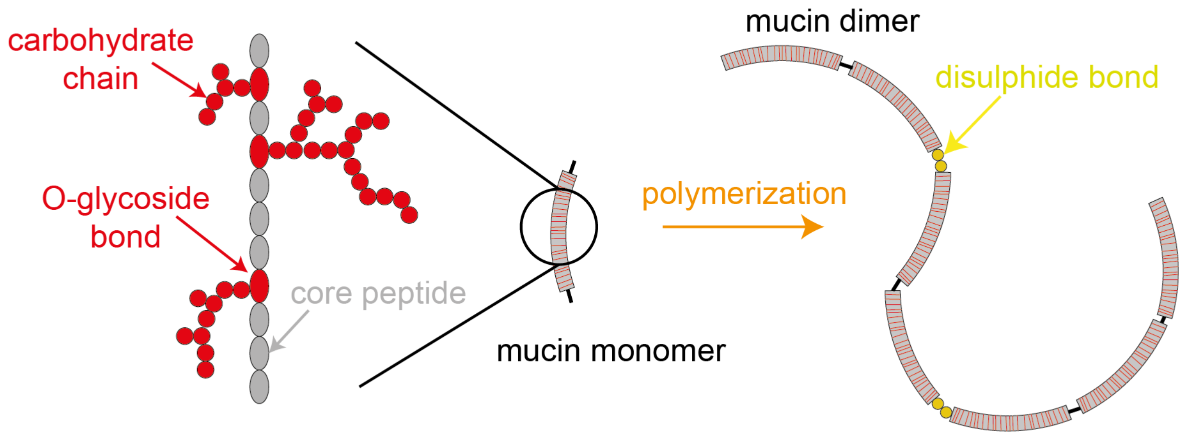

Fig. 2.3: **Schematic structure of mucin molecules**. The scheme illustrates a simplified arrangement of mucin glycoproteins, showing schematically their composition as monomers and dimers. In the monomer form, regions rich in carbohydrate chains are depicted as red diagonal lines, whose tight packing grants protection to the central peptide. Fig. was adapted from Nishiyama *et al.*.[86]

2.1.2.The gastrointestinal flora

Together with the enzymes, microorganisms as well were found to be involved in the digestive process.[87] More specifically, the intestine is populated with bacteria, archaea and eukaryotes, representing a complex and dynamic microbial ecosystem.[88] This ensemble is also known as the gut flora, which develops during the neonatal stage and grows as the human being, also referred to as “the host”, ages.[89] For a healthy human being of middle age the gut flora is basically comprised of anaerobic bacteria and bears up to 10^{12} cells per gram intestine. They cover the gastrointestinal wall, which surrounds the intestinal lumen.[90] Interestingly, in the nineteenth century the gut flora was first declared by Sir W. A. Lane to be a disease called “intestinal toxemia” or “autointoxication”, which could be cured by colonic irrigations or even surgically via removal of parts of the large intestine.[91] Nowadays, it is known that the microbial ensemble functions as a defense against pathogens, supports the digestion and stimulates the intestinal peristalsis.[92]

The gut flora represents a delicate symbiosis between bacteria and human beings.[93] Nowadays, modern lifestyles give more often rise to increased gut problems and diseases. Stress in the daily routine, hurried intake of fast food, long lasting antibiotic treatments and excessive hygiene measures lead to an altered gut flora, which can cause troublesome food intolerance or an irritable colon.[94]

Already in 1907 Élie Metchnikoff discovered that the choice of supplies has an influence on the gut flora and thus on the wellbeing of humans.[95] Back then, he postulated that Bulgarian farmers had a longer life due to the fact that they daily consumed yoghurt.[96] Therefore, he assumed that it was possible to change the gut flora in a positive way and replace pathogens by beneficial bacteria, like the lactic acid bacteria.[97] Finally in 1989, the term "probiotics" (Etymology from Greek, *pro* = for and *bios* = life) was coined. Roy Fuller defined it as an alive microbial food supplement, which improved the intestinal balance and thus had an advantageous effect on the living being.[98] Recently, probiotics were redefined in a more comprehensive way by World Health Organization (WHO) in 2001 as "live microorganisms that confer a health benefit on the host, when administered in adequate amounts".[99] Nevertheless, the scale of the effect exerted by probiotics is still rather disputed. For instance, probiotics were already successfully applied to treat or ease the consequences of many gastrointestinal diseases, such as enteropathy, diarrhea, constipation, etc., however their benefic effect could not be fully proved unequivocally. Probiotic cultures are, for example, also found in fermented dairy products. Nowadays, there are as well products like capsules or tablets containing probiotics. It is important to uptake them alive and ensure their survival and viability until delivery in the gastrointestinal tract.[100, 101] To achieve this, great effort must be made to mitigate the harmful effects of the gastric acid, which destroys most of the probiotics taken in orally, during the passage in the stomach. Therefore, in the past decades a great effort was made to design novel microencapsulation techniques to entrap probiotics or other beneficial food supplements in biocompatible polymer matrices and eventually to improve the release mechanisms for a targeted delivery in the intestinal tract.

In general microencapsulation has found broad applications in the fields of medical, pharmaceutical, and food additives industries. Its primary duty is the creation of delivery systems necessary to transport substances, active chemical compounds, or alive cells into the body ensuring the maintenance of their functionality throughout the passage in the gastrointestinal tract. To achieve this, a broad spectrum of materials, especially gel-forming polymers, can be used for example: ethyl cellulose, polyvinyl alcohol, gelatin and sodium alginate.[102, 103]

2.2.Sodium Alginate

Sodium alginate is a biocompatible, biodegradable, non-toxic and non-immunogenic biopolymer with a broad range of possible applications. It can be either produced from purification of algal particles originating from brown algae,[104] or alternatively by means of biosynthesis in order to satisfy the high industrial demand.[105]

Alginate polymer chains are made of two different monosaccharide subunits, α-L-guluronic acid and β-D-mannuronic acid, which are usually referred to as G- and M-blocks.[106] The latter are linked to each other *via* a 1,4-glycosidic bond; interestingly, the sequence of G- and M- blocks and the ratio between

G and M blocks depends exclusively on the type of algae, that were used to extract the polymer.[107] Note that homopolymeric M-blocks form long, flexible chains, whereas G-blocks form stiffer zigzag ones, as shown in Fig. 2.4.

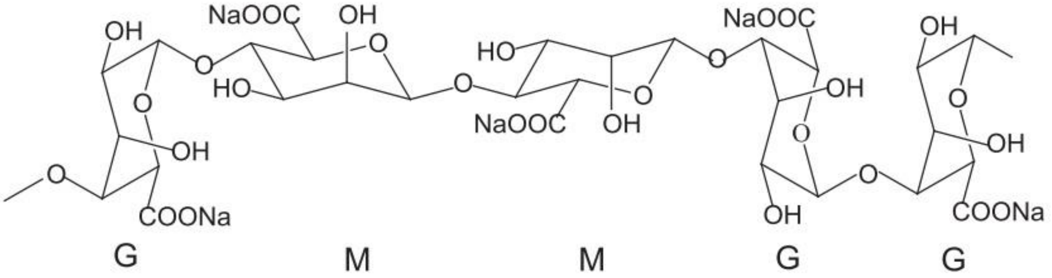

Fig. 2.4: Structure of alginate. Three possible di-block arrangements are shown, for instance a hetero GM or MG di-block, a homo MM di-block, and a homo GG di-block linked *via* a 1,4-glycosidic bond. Fig. was adapted from Yang *et al.*[106]

Because sodium alginate is an anionic polymer, it possesses the property to complex and entrap metal ions such as Calcium (II). For instance, four G-blocks can entrap a single calcium ion, which causes the polymer to stiffen and form a gel. This peculiar arrangement, namely of a calcium ion trapped within four guluronic acid units is known as the "eggbox-model", due to the similarity between the divalent ions, which appear to be sitting in square box-like cavities, and eggs packaged in egg cartons, as shown in Fig. 2.5.

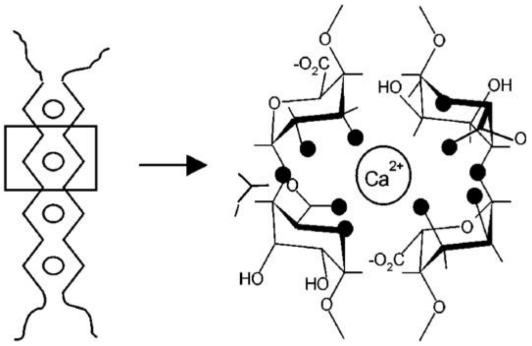

Fig. 2.5 The egg-box model and the complexation of calcium ions. Fig. was adapted from Braccini *et al.*[108]

Note that only the G-blocks are able to form complexes with Ca^{2+}, therefore different ratios between G and M blocks result in hydrogels possessing different stiffness. To be more precise, if the polymer chain is rich in G-blocks, the resulting hydrogel will possess an increased stiffness, due to the numerous calcium complexes that are formed. On the other hand, if we increase the number of more flexible M blocks, the resulting gel will be softer.

To conclude, thanks to its versatility and the capability of forming a hydrogel, sodium alginate has found many diverse fields of applications. For instance, the fact that this biopolymer is entirely biocompatible and non-toxic made sodium alginate appealing for industry and research to be applied in the medical field. In particular, the creation of alginate gel capsules and beads is of great interest, since these materials can be used as promising and novel smart drug delivery systems.

2.3.The mucus and the phospholipid barrier.

Mucus alone is not capable of protecting the underlying epithelial layer from the attack of pathogens that are part of the gut flora. As shown in Fig. 2.2, another key component of the gastrointestinal mucus comprises the phospholipids. For instance, when the latter are bound to the mucus, they form a hydrophobic layer that enhances the protective capacity of the mucus itself, by hindering the chance for pathogens to reach, attack and harm the underlying intestinal epithelial layer.[109]

Phospholipids are lipids that possess a polar head containing a phosphate group. Basically, they are constituted of two units, a hydrophilic head and two hydrophobic fatty acid chains, that confer them an amphiphilic character. Together with glycolipids and cholesterol, phospholipids are the major constituents of the cell membrane.[110] When the phospholipids headgroup is modified with an organic molecule, such as choline, phosphatidylcholines are obtained. Choline is a quaternary ammonium compound bearing a positive charge at the nitrogen atom, as shown in Fig. 2.5. Since phosphatidylcholines possess a negative charge at the phosphate group, together with the positive ammonium group they can be regarded as zwitterionic species. Interestingly, they make up to ca. ~ 90 % of the total amount of phospholipids in the mucus.[109] The group of phosphatidylcholines is also known as lecithin and it was first identified in 1847 in the yolk of chicken eggs.

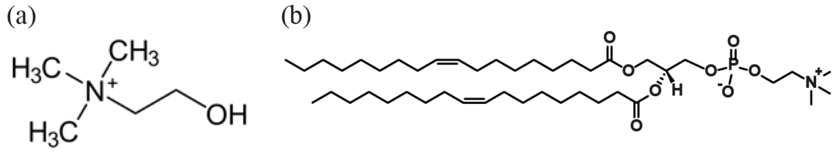

Fig. 2.5: Structure of choline and of DOPC. (a) Chemical structure of choline and (b) chemical structure of DOPC.

Among other important features, phosphatidylcholines possess remarkable emulsifying and lubricating features. Nonetheless, several crucial functions have been attributed to them, for instance their contribution in fat metabolism, in the constitution of biological membranes, in sustaining the high shear forces that result from friction in the joints,[111] and, last but not least, in supporting mitosis.[112] One important member of the phosphatidylcholine group is 1,2-dioleoyl-*sn*-glycero-3-phosphocholine (DOPC). Not only animal cells are rich in DOPC, which constitutes their permeable cell membrane, in addition to that, DOPC represents one of the most examined lipid model systems, because of its involvement in many biological processes and structures.[113]

2.4.(Phospho)lipids and self-assembly

Thanks to their amphiphilic character, when (phospho)lipids are dispersed in water they tend to self-assemble and spontaneously form micelles or vesicles as well as lipid bilayers, similar to what constitutes the cell membrane. The self-assembly is driven by the hydrophobic effect,[114] which is an entropic effect originating from the hydrogen bonded structure of water. This can be understood in terms of the change in Gibbs free energy as:

$$\Delta G = \Delta H - T\Delta S \tag{2.1}$$

For instance, if one lipid molecule is transferred into water, an ordered structure of water molecules must form around the hydrocarbon chains. Therefore, the entropy of transfer ΔS in this case must always be negative. On the other hand, the enthalpy of transfer is of less influence and can be either positive or negative.[114] Thus, the change in Gibbs free energy is overall positive and therefore the introduction of a lipid molecule in water costs free energy. To be more specific, the change in the free energy herein can be related to the change in the chemical potential due to the transfer of a lipid molecule from a standard state $\mu_{HC,ref}$ where we assume that the hydrocarbon chain is located in pure hydrocarbon environment into water $\mu_{HC,water}$:

$$\mu_{HC,ref} - \mu_{HC,water} = RTln\mathrm{X}_{HC,water} \tag{2.2}$$

where $X_{HC,\ water}$ corresponds to the mole fraction of lipids in water. Note that the difference in chemical potential can be determined experimentally, if the solubility of the hydrocarbon chains in water is known. McAuliffe et al. found that the solubility of hydrocarbon chains in water decreases linearly with the chain length.[115] More interestingly, they reported that each additional methyl group in the hydrocarbon chain corresponds to an energy cost of ~ 6×10^{-21} J. The latter must be paid because each new added group forces more water molecules to lie next to the hydrophobic chains and in terms of energy it corresponds to ca. 20% of a hydrogen bond, which is estimated to be $1 - 5 \times 10^{-20}$ J.[116]
However, according to the Gibbs phase rule, a lipid in water and a lipid in bilayer can be in equilibrium only at a fixed value of $X_{HC,\ water}$. This value is known as the critical aggregate concentration and it can be defined by rearranging Eq. (2.2) in a logarithmic form:

$$\mathrm{X}^*_{HC,water} = \mathrm{X}_{HC,bilayer}e^{\left(\frac{\Delta\mu}{RT}\right)} \tag{2.3}$$

To give an example, the critical aggregate concentration for single chain lipids, such as lyso-PC, is about $X^*_{lyso\text{-}PC,\ water} \sim 10^{-4}$ M whereas for double chain lipids, for example DPPC, $X^*_{DPPC,\ water} \sim 10^{-12}$ M.[117]
This small value indicates that even at very low concentrations, double chains lipids start to form micelles spontaneously.

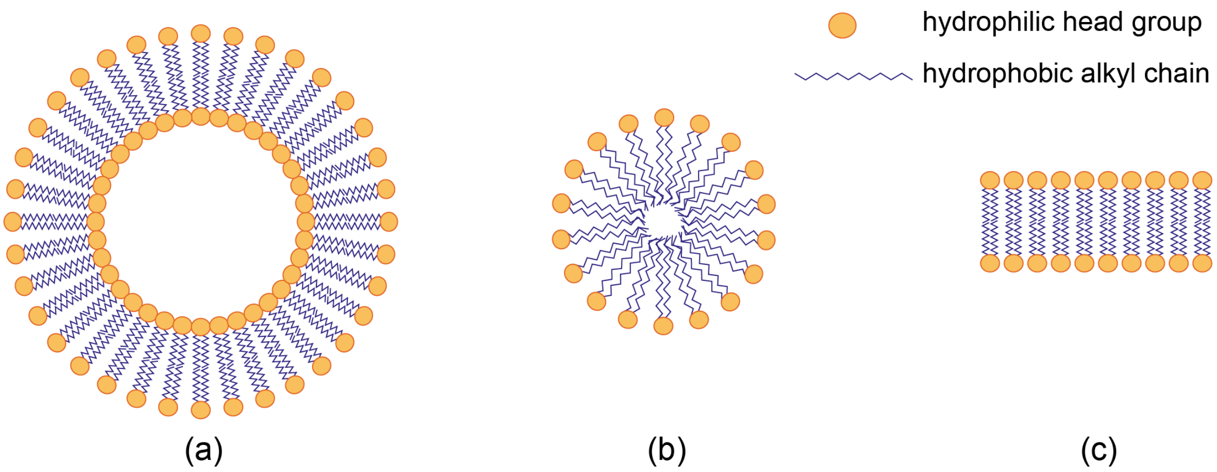

Fig. 2.6: (Phospho)lipids self-assembly configurations. (a) Vesicle, (b) micelle and (c) bilayer structure.

2.5.Solid-supported membranes as a model of cell surface

This section was written making use of the review article of Tanaka *et al.*,[118] who is one of the leading experts in this field and extensively used solid supported membranes as *in vitro* membrane model.

As it was mentioned in section 2.4, one of the most important key features of (phospho)lipids is the fact of being the major constituents of biological membranes. The latter are vital components of all living systems and they are responsible to form the outer boundary of living cells or of their organelles, which are defined as the internal cell compartments. The fact that lipids forming biological membranes assemble in lipid bilayer structures confer them a fluid character, which the expression "quasi two-dimensional fluid mosaic model" stem from. Various functional proteins, which can be classified into embedded, integral and peripheral depending on their position in the membrane and carbohydrates attached to the cell membrane surface facilitate communication and transport across it. These features enable membranes to act as important filters, therefore by keeping toxic substances outside the cell and by letting only specific nutrients to move across it and attain their destination. Last but not least, through complex interactions between peripheral and integral membrane proteins many important biological processes are regulated at cell membrane surface.

The reason why *in vitro* models have been developed to mimic biological membranes is because the intrinsic difficulty to make direct investigations of such a complex system consisting of conspicuous and diverse intra- and extracellular networks and interactions. For almost 20 years, the so-called solid-supported membranes, namely phospholipid bilayers deposited onto solid substrates have been the most widely used experimental cell-surface *in vitro* model. The latter are prepared by direct deposition of lipid vesicles on amphiphilic surfaces that spread and cover them to yield a large coverage area, up to the order of cm^2. Interestingly, when lipid bilayers are formed in this way they maintain an outstanding mechanical stability without any loss of their fluid nature.[119-121] The maintenance of mechanical stability together with membrane fluidity of solid-supported membranes allowed researchers to perform experiments and use analytical techniques that are difficult, if not impossible, to be applied to other model systems. For instance, methods such as total interference fluorescence,[122, 123] nuclear magnetic resonance (NMR),[124] Fourier-transform infrared spectroscopy,[125] surface plasmon resonance,[126] and X-ray and neutron scattering,[127-129] can all be used to probe the structural and dynamic properties of supported membranes. Overall, solid-supported membranes have allowed us to gain insight into immune reactions and cell adhesion[130-136] among other interesting phenomena of deep biological relevance.

It is easy to make solid supported membranes which can be functionalized by using membrane-associated proteins. In this case, let us first consider a functionalization using transmembrane proteins, such as ion channels or membrane-spanning receptors. This can be achieved in two ways. One straightforward method is to spread lipid vesicles containing reconstituted integral proteins onto planar substrates. The other one is to prepare supported membranes and embed ‘anchor’ molecules, such as biotin, which in a second step engineered or modified proteins are coupled to. Interestingly, the intermolecular distance between the anchor molecules can be tuned by regulating their molar fraction according to the relation:

$$\langle d \rangle = \sqrt{\frac{A_{lipid}}{\chi}} \tag{2.4}$$

where χ is the molar fraction of the anchor, for example of biotin, and is A_{lipid} is the projected area of the lipid polar head, which for DOPC is $\approx 65\ \text{Å}^2$.

The advantage of these *in vitro* methods, when used in combination with advanced protein engineering and bioorganic chemistry techniques, is the fact that they grant us the possibility to investigate complex processes, that would be impossible to be studied otherwise.

Supported membranes with embedded reconstituted proteins have already played a major role in providing information about several important biological processes. To give an example, an early study shed light on the recognition mechanism of antigen-carrying cells by T cells, that is a key step in order to trigger a specific immune response and that requires antigens to be associated with the major histocompatibility complex.[122] Later work,[135] revealed that initiation of the immune response depends on dynamic features of the recognition and interaction process that creates the immunological synapse, which is defined as the supramolecular contact between the T cell and the antigen-presenting cell. The preservation of the lateral fluidity of the lipids within the supported membranes, was the key factor that lead to a positive outcome of this investigation. This was indeed a proof-of-concept to validate the use of supportive membranes as artificial surrogate cell surfaces to study the dynamic aspects of membrane function. Moreover, using cells or vesicles in conjunction with supported membranes offers opportunities for examining cell adhesion.[137, 138] In addition to that, solid-supported membranes have been used in combination with semi-conductors devices to design novel electrochemical and optical biosensors, towards the transduction of smart biological functions intro electrical/optical readouts, that might have an impact in unraveling the interaction mechanisms of biologically and medically relevant small molecules with membranes.[139, 140]

However, solid-supported membranes have some fundamental drawbacks. The latter stem from the fact that the deposited lipid bilayer which mimics the artificial membrane is in the proximity of the bare solid surface onto which it is deposited. Therefore, the distance between them is usually not large enough to avoid direct contact between transmembrane proteins incorporated in the membrane and the solid surface. This issue becomes serious when working with systems, whose functional extracellular domains can extend to several tens of nanometers, for instance in case of cell-adhesion receptors. This problem can be overcome by separating the membrane from the solid substrate using soft polymeric materials that act as a cushion. In this way, the risk of protein denaturation caused by the frictional coupling between membrane-incorporated proteins and the solid support, is overall reduced.[121, 141-143]

2.5.1.Biotin

In the previous section, it was mentioned that one of the molecular anchors that can be doped into lipid supported membranes is biotin. Biotin (Fig. 2.7) is a water-soluble compound belonging to the group of B-vitamin complexes, which can be found in several foods in µg ranges. It is necessary for cell growth and plays an important role as prosthetic group of enzymes in the metabolism of fats, amino acids and carbohydrates. Moreover, biotin serves in the cell nucleus as epigenetic gene regulator,[144] therefore, even if in small amounts, it is needed. Since the 1940s, it is known that among other beneficial substances probiotic bacteria in the gut flora produce and accumulate biotin, of which certain amounts are reabsorbed and utilized by the host.[145, 146]

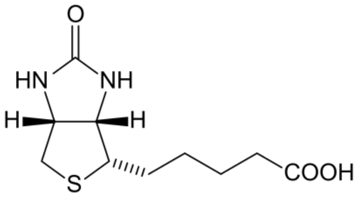

Fig. 2.7: Structure of biotin. Chemical structure of biotin.

In biochemistry,[147] biotin is a compound used as a covalent marker for proteins. Through the biotinylation process, biotin groups are covalently bound to the protein, without any loss of protein activity, because of biotin's small size. Following biotinylation, the strong biotin-avidin affinity is exploited in such a way, to functionalize the solid-supported membrane with our protein of interest.

2.5.2.Avidin

Avidin is a well-known glycoprotein having strong affinity to specifically bind biotin (dissociation constant $K_d = 10^{-15}$ M) and therefore the avidin-biotin complex is the strongest known non-covalent interaction between a protein and a ligand.[148] It is found in the egg albumen of bird eggs and is produced in oviducts. The glycoprotein exists as tetramerous compound and therefore is able to bind four biotin molecules at the same time. Interestingly, 10 % of the components of avidin consist of carbohydrates, such as mannose and N-acetylglucosamine residues.[149] As a consequence, consuming raw eggs, that means avidin, can lead to an insufficient absorption of biotin by the gastrointestinal tract and thus can cause a lack of biotin. Only by cooking the egg albumen the binding affinity of avidin to biotin can be jeopardized.[150] Nevertheless, avidin has become an important tool in biotechnology and biochemistry. The strong affinity towards biotin is exploited in several applications, such as Western Blot or ELISA. The specific interaction can as well be used for means of purification or labeling of substances.[151]

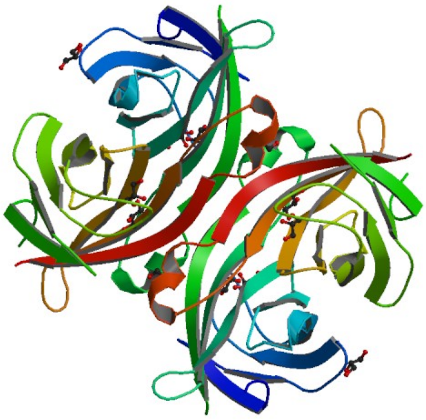

Fig. 2.8: Crystal structure of Avidin. Three-dimensional structure of Avidin in its tetrameric form. Fig. was adapted from Repo *et al.*.[152]

Because of the high bonding affinity between biotin and avidin, the bond formation takes place very rapidly, and afterwards it is unaffected even in the presence of extreme conditions of pH, temperature, organic solvents and other denaturing agents.[149] NeutrAvidin is the deglycosylated version of avidin. Note that the cleavage of the carbohydrates doesn't affect the binding affinity to biotin because they do not play any role in the binding formation. Similar to avidin, NeutrAvidin is a tetramer as well that can accommodate up to four biotin molecules with the same dissociation constant as avidin.[153] On the other hand, different with respect to avidin, whose high isoelectronic point is at pH = 10.5, neutrAvidin has a near-neutral one at pH = 6.3.[154] The combination of the lack of carbohydrate groups together with a neutral isoelectronic point reduces drastically the non-specific interactions of NeutrAvidin with charged surfaces. Therefore, the high biotin-binding affinity and low non-specific binding make NeutrAvidin the most ideal biotin-binding protein.

2.6.Reflection Interference Contrast Microscopy (RICM)

In biophysical chemistry, the development of methods to investigate the inter-surface interactions including the dynamics of colloidal beads close to a surface or the adhesion strength of vesicles and cells on soft interfaces is of great interest. These interactions are not trivial; on the contrary, they are found to be complex processes, in which adhesion and repulsion dominant roles are exemplified by specific and unspecific bonding forces.[155]

To date, a number of various techniques are known, that allow quantitative measurements down to molecular distances.[156] However, most of these techniques are not applicable to investigate cells, because on one hand they are not suitable for dynamic studies and on the other hand they can only measure relative changes in the distance between cells and the substrate.[157, 158] Herein, Reflection Interference Contrast Microscopy (RICM), an optical technique known since 1958,[159] was found to be suitable for investigations of inter-surface interactions with the advantage of being able to follow the dynamics, without making use of any invasive fluorescent labeling.[160] This technique was used successfully for the first time in 1964 to investigate cell adhesion on glass surfaces and to measure the thickness of cell membranes.[161]

Subsequently, in the 1980s Sackmann *et al.* demonstrated that the distance between a spherical object, such as colloidal beads, hovering over a planar transparent substrate could be quantified by RICM.[162] Afterwards, in 1992 Sackmann et al. examined the interactions between spherical vesicles and lecithin monolayers.[155] Last but not least, seven years later, they could as well measure the height of latex beads hovering over polyelectrolytic films by analyzing the Brownian motion of the beads.[162] In other recent studies, RICM has been applied to successfully investigate the elastic properties of pH-responsive gels,[163] and the effect of ionic strength on the conformation of polymer brushes.[164] This was achieved by solving analytically the equation of motion and calculating the interfacial potentials of latex beads hovering over the substrates.

The principle of RICM is based on detection of interference patterns, which arise from light reflections at interfaces with different refractive indices. For example, in case of a system with two interfaces, the reflected intensity I under quasi-normal incidence is given by,[160]

$$I = I_1 + I_2 + 2\sqrt{I_1 I_2} cos[2kh(x,y) + \phi] \tag{2.5}$$

where $k = 2\pi n_1/\lambda$, ϕ is the phase shift, $h(x,y)$ corresponds to the vertical distance which separates the two interfaces at the lateral position (x,y) and I_1 and I_2 represent the reflected intensities at interface 1 and 2, respectively. Therefore, it is sufficient to record the two-dimensional intensity pattern with a CCD camera to calculate the distance separating our probe, for example a cell or a colloidal particle, and the substrate.

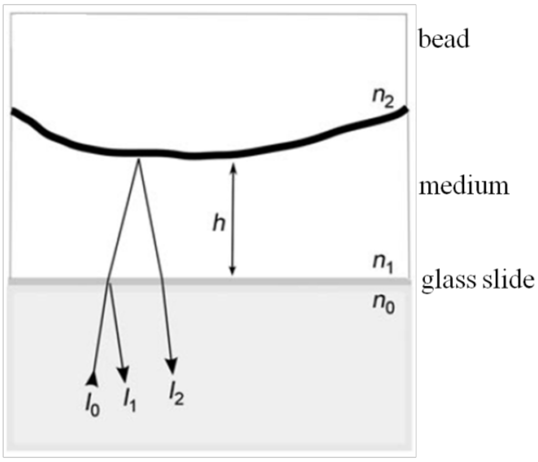

Fig. 2.9: Working principle of the RICM technique. The situation described by Eq. 2.5 is schematically illustrated. Fig. was adapted from Limozin *et al.*. [160]

2.6.1.RICM instrumental setup

The RICM setup is made of an inverted microscope which is coupled to a partial incoherent, monochromatic light source and is provided with an oil-immersion antiflex objective, as shown in Fig. 2.10 (a). The presence of an aperture and field diaphragm together with a collector lens makes the optical equipment suitable for Köhler illumination.[165] A great improvement of the image quality was achieved when Ploem developed the antiflex technique,[166] which relies on the insertion of three additional optical components in the light path compared to an inverted microscope standard setup: A polarizer, a λ/4-plate and an analyzer. At first, the polarizer filters out random polarized light to let only linear polarized light with a preferred direction pass. Subsequently, the built-in λ/4-plate of the objective transforms the linear polarization to a circular one and its reflection at interfaces with different refractive indices causes a phase shift of π of the two electrical field components (perpendicular and parallel). When the reflected light with a phase shift of π passes once again through the λ/4-plate, the polarization is converted back to linear. Finally, the analyzer filters out all other illumination sources and lets only the reflected light with a linear polarization state to be detected by the camera; the result is an image with high contrast. Temporal and spatial coherences are additional prerequisites, that are necessary for the visibility of interference patterns. The former describes the correlation between rays observed at different time intervals. In RICM, a metal halide lamp in combination with an interference filter emits a quasi-monochromatic green light with a wavelength distribution of $\lambda = 546 \pm 10$ nm, which guarantees a high temporal coherence. On the other hand, the latter is based on the correlation between rays at different points in space. Since the spatial coherence length for a metal halide lamp corresponds approximately to 200 μm, which is much bigger than the typical measured distances with RICM, this prerequisite is satisfied as well. However, note that because of the finite extension of the light source, full spatial resolution can never be achieved.

As the light source is considered as point source, the illuminated area has different degrees of coherence. Full spatial coherence occurs at an illumination area with a diameter *d* of

$$d \leq \frac{0.16\lambda}{n\,sin(\alpha)}0.16 \tag{2.6}$$

where λ is the light source wavelength, n is the refractive index of the medium and α is the incident angle of the incoming beam.

The size of the light source plays also a key role in setting the interplay between the lateral resolution and focus depth and it can be controlled by different opening "degrees" of the aperture diaphragm. In case of an opened aperture diaphragm, the illumination aperture INA,

$$INA = n\sin{(\alpha)} \tag{2.7}$$

is increased. As a result, a high lateral resolution with a limited depth in focus is obtained.

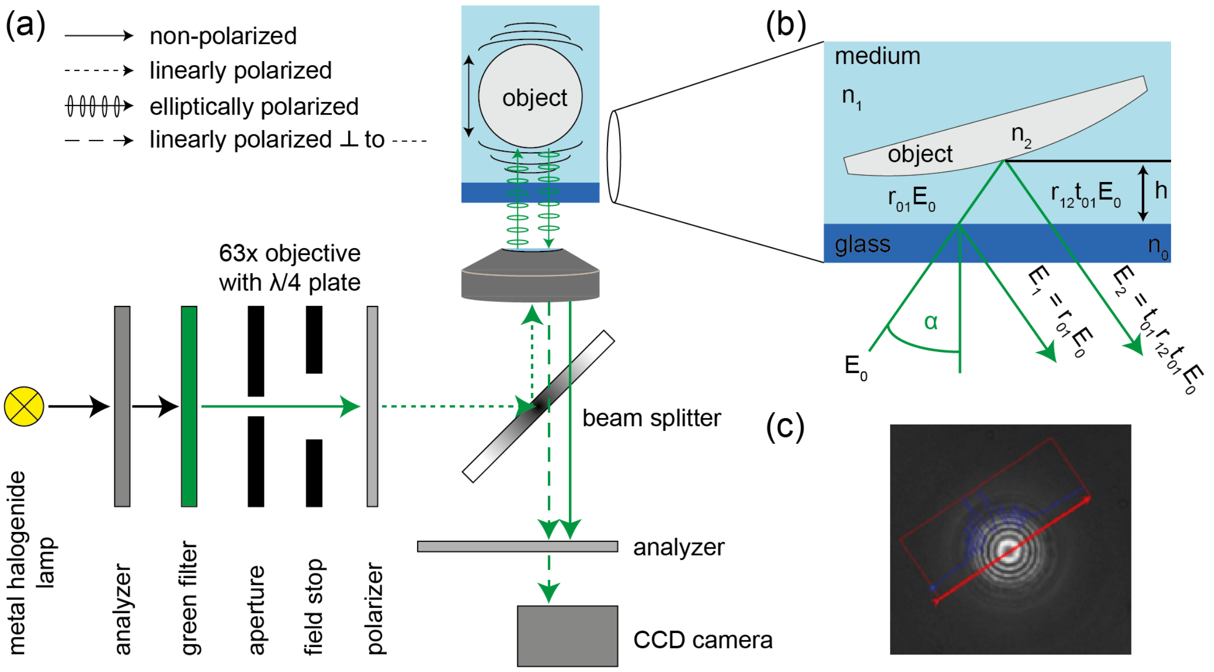

Fig. 2.10: RICM experimental setup. (a) Schematic illustration of the experimental setup, that includes a bandpass filter (λ = 546 ± 10 nm), two adjustable diaphragms, a polarizer, an analyzer and a 63x objective with built-in λ/4 plate, allowing Köhler illumination under quasi-normal incidence of light. (b) Monochromatic incident rays are reflected at interfaces with different refractive indices and can interfere constructively and destructively leading to the formation of Newton fringes, according to Eq. 2.5. (c) Example of Newtonian fringes formed by a spherical object, in this case a silica particle. Fig. was adapted from Burk.[167]

2.6.2.Image formation

The image formation relies on the detection of interference patterns formed by constructive and destructive interferences of reflected rays due to their differences in the optical path lengths δ. Subsequently, contrast variations of the recorded image can be reconducted to the separation distance between the sample and the substrate underneath, for example a glass slide, typically in the order of tens of nanometers. Typical patterns from various objects are depicted in Fig. 2.11. The sequence of dark and bright rings, which we refer to as Newtonian rings, correspond to minimal and maximal intensities, following the principle of destructive and constructive interference, respectively. The mathematical description of image formation in RICM was described by Wiegand *et al.*.[168] The intensity of the incident light experiences multiple reflections and refraction at interfaces of layers with different refractive indices *n*. The reflected intensity *I(x,y)* corresponds to the average of the squared electric field *E(r,t)* and is related to the phase $\phi(r)$ as given by:

$$I(x,y) = \langle E^2 \rangle_t$$
$$E(r,t) = E(r,t) \cdot e^{[i(\phi(r)+\omega t)]} \tag{2.8}$$

The electric field vector E_r includes the sum of all the electric field vectors, $E_r = \sum_i E_{r,i}$,of the reflected light at different layers of the specimen and can be expressed as a function of the electric field vector E_0 of the incident light.

$$E_r = r_{01}E_0 + (1 - r_{01}^2)r_{12}E_0 e^{(-ik\delta_1)} + \cdots +$$
$$= RE_0 \tag{2.9}$$

r_{ij} corresponds to the reflection coefficient which relies on the Fresnel coefficients r_{ij}^p and r_{ij}^s which can be expressed in terms of to the refractive indices of the successive layers n_i and n_j and of the angle of incidence α as given by:

$$r_{ij}^p(\alpha) = \frac{n_j cos\alpha_i - n_i cos\alpha_j}{n_j cos\alpha_i + n_i cos\alpha_j} \tag{2.10}$$

$$r_{ij}^s(\alpha) = \frac{n_i cos\alpha_i - n_j cos\alpha_j}{n_i cos\alpha_i + n_j cos\alpha_j} \tag{2.11}$$

p and *s* denote the polarization of the reflected wave parallel or perpendicular to the plane of incidence, respectively. The transmission coefficient, t_{ij}, is described by the following equation:

$$t_{ij} = \sqrt[2]{1 - r_{ij}^2} \tag{2.12}$$

The phase shift caused by the reflection of light at layer *I* is a product of the wave number $k = 2\pi/\lambda$ and the optical path length δ. The resulting reflection coefficients of all interfaces can be summarized in an effective reflection coefficient *R*, which is defined as

$$R = r_{01} + \sum_{i=1}^{m} \left[\prod_{s=1}^{i} (1 - r_{s-1,s}^2) e^{-ik\delta_s} \right] r_{i,i+1} \,,$$
$$I(x,y) = R^* R E_0^2 = R^* R I_0 \,, \tag{2.13}$$

where *m* corresponds to the number of layers. This assumption is only valid if multiple reflections are small and negligible. The optical path length δ_i of the reflected ray traversing layer *i* is given by:

$$\delta_i = 2n_i d_i(x,y) \,, \tag{2.14}$$

where $d_i(x,y)$ represents the thickness of layer *i* at its position (x,y).

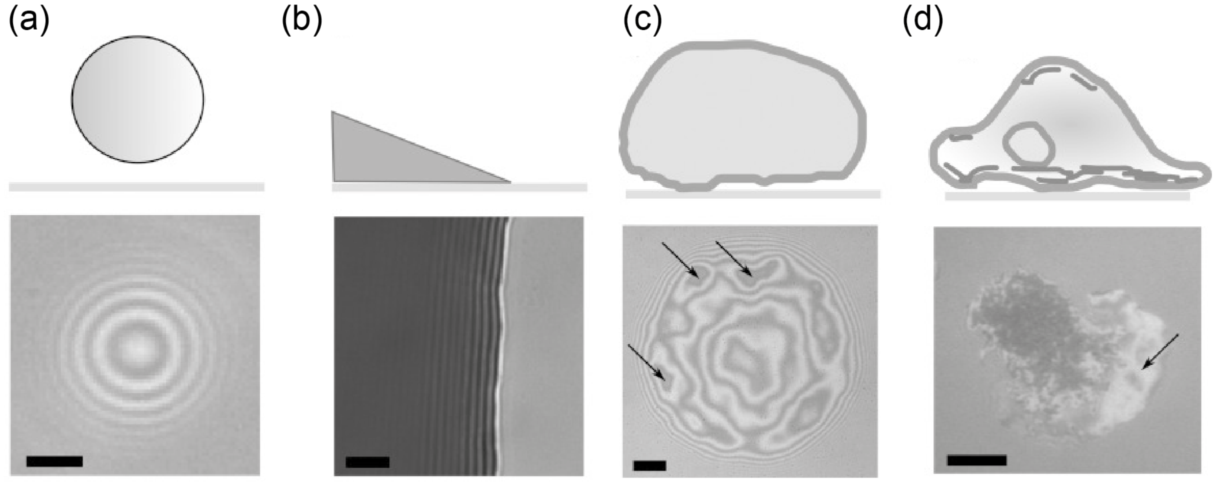

Fig. 2.11: Examples of RICM patterns with different geometries. The Fig. illustrates some examples of RICM patterns reflecting characteristic geometries: (a) a spherical object, (b) a triangular-shaped layer coated on a glass substrate, (c) a vesicle displaying unspecific binding to a substrate, and (d) an adherent cell. Fig. was adapted from Sengupta *et al.*.[165]

2.6.3.RICM for a latex particle

In Chapter 5, the interfacial interactions between phospholipids and mucin were investigated by means of RICM. For this purpose, the fluctuations of spherical silica and latex microparticles over substrates functionalized with mucin were recorded. The theoretical description of the vertical motion of a latex particle was given by Raedler and Sackmann,[155] and was adopted from Higaki *et al.* and Amadei *et al.*.[164, 169]

The general Langevin equation describes the equation of motion for a spherical latex particle undergoing a vertical Brownian motion as follows:

$$m\frac{\partial^2 \Delta h}{\partial t^2} + \gamma\frac{\partial \Delta h}{\partial t} + \frac{\partial V}{\partial \Delta \mathrm{h}} = F_{stoch} \tag{2.15}$$

where m is the mass of a particle, γ the friction coefficient, Δh the relative particle position, $V(\Delta h)$ the interfacial potential, and F_{stoch} the stochastic force of the thermal noise. The second term corresponds to the frictional force F_{fric} that can be written in terms of the Reynolds equation:[170]

$$F_{fric} = \gamma\frac{\partial \Delta h}{\partial t}, \quad \text{where} \quad \gamma = 6\pi\eta_{eff}\frac{R^2}{h}, \tag{2.16}$$

where $\frac{\partial \Delta h}{\partial t}$ is the relative velocity, η_{eff} the effective shear viscosity of the system, and h the absolute distance between the particle and the surface. Considering that the bead radius $R \approx 5$ µm, $\frac{\partial \Delta \mathrm{h}}{\partial \mathrm{t}} \approx \frac{10^{-8}}{0.03}$ m/s, the density of latex particle $\rho_{latex} = 1.04$ g/cm^3, and the viscosity of water $\eta_{\mathrm{w}} = 1$ mN·m^{-2} · s, the Reynolds number Re of the system can be estimated to be,[170] $\mathrm{Re} \leq R\left(\frac{\partial \Delta \mathrm{h}}{\partial \mathrm{t}}\right)\rho\eta_{\mathrm{w}}^{-1} \sim 10^{-4}$ that is far below 1. Therefore, the particle movement is overdamped, and consequently the first acceleration term in the Langevin Eq. (2.15) can be crossed out.[171] Furthermore, if the amplitude of the height fluctuations is small, the effective interfacial potential can be approximated as harmonic:[75]

$$V(\Delta h) = \frac{1}{2}\frac{\partial^2 V}{\partial \Delta h^2}\bigg|_{\langle h\rangle_t} (\Delta h - \langle \Delta h\rangle)^2 = \frac{1}{2}V''\Delta h^2 \tag{2.17}$$

Since the fluctuations amplitude in our experimental system is $\Delta h \leq 30$ nm, this enables one to analytically solve the Langevin equation. The autocorrelation function of the height fluctuations can be calculated within the framework of the fluctuation−dissipation theorem:

$$\langle \Delta h(\delta t)\Delta h(0)\rangle \approx \langle \Delta h^2(0)\rangle e^{-\delta t/\tau}, \quad \text{where} \quad \tau = \frac{\gamma}{V''} = \frac{6\pi\eta_{eff}R^2}{\langle h\rangle V''} \tag{2.18}$$

Here the mean squared amplitude can be derived from the equipartition theorem:

$$\langle \Delta h^2(0)\rangle = \frac{k_B T}{V''}. \tag{2.19}$$

Under thermodynamic equilibrium, the effective interfacial potential $V(\Delta h)$ can also be calculated from the probability function of fluctuation amplitude of the particle $P(\Delta h)$, following Boltzmann's distribution:[162, 172, 173]

$$P(\Delta h) \propto \exp\left(-\frac{V(\Delta h)}{k_B T}\right) \text{ and thus } V(\Delta h) = -k_B T \ln\big(P(\Delta h)\big) + \text{const.} \tag{2.20}$$

2.7.X-ray scattering

In this section, a few basic concepts of X-ray scattering theory are introduced, that are propaedeutic to the description of the experimental technique X-ray photon correlation spectroscopy, that will be extensively discussed in the next sections. For this purpose, the following textbooks were used as sources: *X-ray and neutron reflectivity: principles and applications* of Daillant, J. and Gibaud, A.[174], and *Elements of modern X-ray physics* of Als-Nielsen, J. and McMorrow, D..[175]

2.7.1.X-ray interaction with matter

X-rays is a form of electromagnetic radiation being part of the wide electromagnetic spectrum which propagates and interacts with matter in the form of oscillating electric and magnetic fields. Most X-rays have a wavelength ranging from 0.01 to 10 nanometers, corresponding to frequencies in the range 30 petahertz to 30 exahertz (3×10^{16} Hz to 3×10^{19} Hz) and energies in the range 100 eV to 100 keV. X-ray wavelengths are shorter than those of UV rays and typically longer than those of gamma rays.[176]
The interactions between an X-ray beam hitting any type of matter are essentially of two types: in the first case, the electric field of the incident wave interacts with the electrical charges; in the second case, the magnetic field of the incident wave can interact with the magnetic moments, also defined as spin, of the matter. If we take a closer look to the first case, in the event of a photon hitting an atom, three events can take place as described as follows (Fig. 2.12): elastic scattering, also known as Rayleigh scattering, where the energy of the scattered photon remains unchanged; inelastic scattering, also known as Compton scattering, where part of the energy is lost due to the collision with an electron; photoelectric adsorption in which a photoadsorbed photon transfers all its energy to the electron with which it interacts, thus ionizing the atom. The electron that was bound can produce a photoelectron that is likely

to ionize more atoms in its path. Note that an electron from an upper energy level can fill the vacancy in the atom. This process is combined with an emission of an X-ray fluorescent photon. However, the X-ray fluorescent photon can be reabsorbed in a secondary process by a valence electron causing the ejection of the electron from the atom, which is then defined as Auger electron.

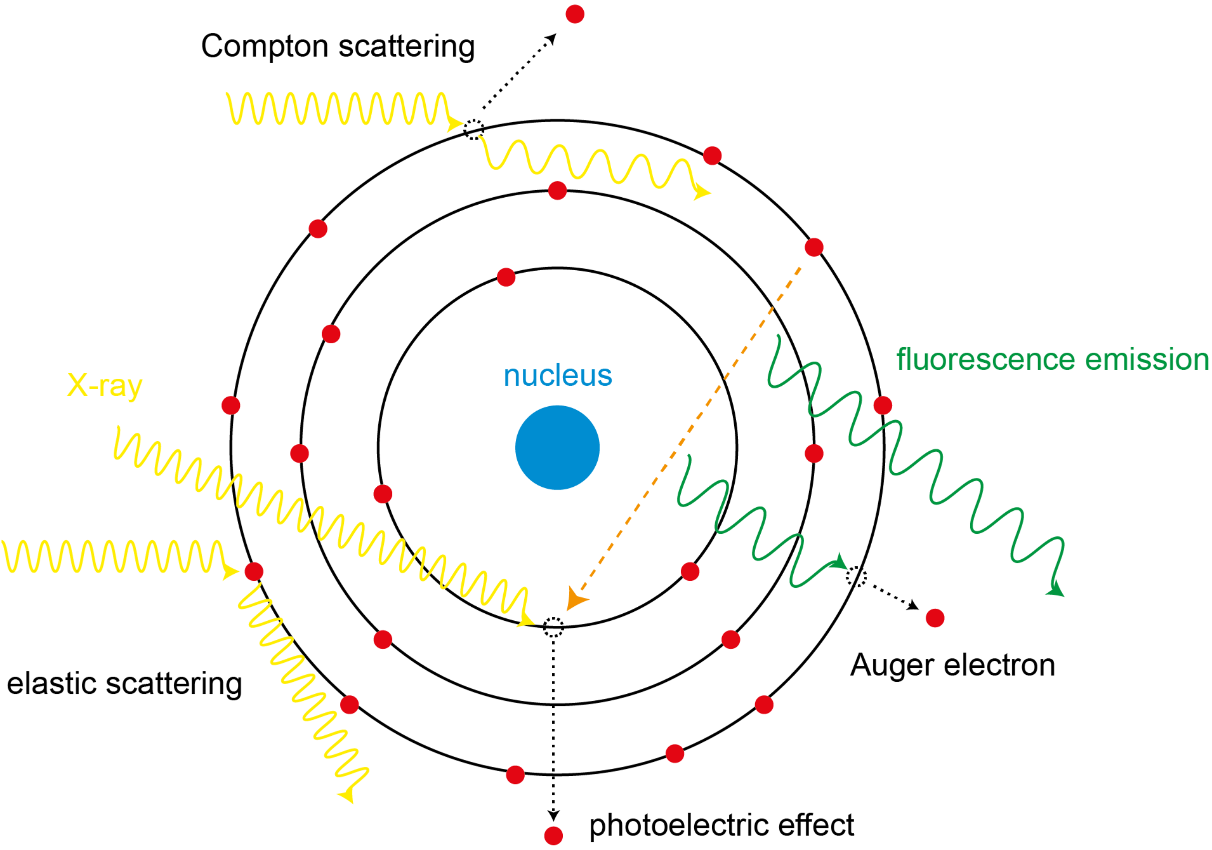

Fig. 2.12: Possible interactions between X-rays and matter. The Fig. illustrates schematically the three possible ways through which an X-ray photon can interact with an atom: (i) elastic or Rayleigh scattering, (ii) inelastic or Compton scattering, and (iii) photoelectric effect. Fig. was adapted from Abuillan.[177]

Since the wave oscillation amplitude of the elastically scattered photons is inversely proportional to the mass of the "scattering object", which from now it will be referred to as "scatter", electrons are the main responsible in the scattering process, by possessing a mass that is 1836 times smaller than the protons one. Furthermore, the scattering amplitude depends on the number of electrons per atom and consequently on the atom type. Besides, the far-field amplitude of the scattered photons, where constructive and destructive interference take place, depends on the relative positions of the scatters. Therefore, the elastic scattering of X-rays contains information about the structure and the arrangement of atoms within the sample whereas the inelastic scattering gives an insight about the vibrations within the atoms. Last but not least, the absorption process is usually used to study the fine structure, type and environment of the matter at the atomic scale.

2.7.2.Basics of X-ray scattering

The basic principle of X-ray scattering experiments assumes that every single electron, that makes up the atomic electron cloud, scatters the X-rays in an elastic manner. Moreover, the scattering process is defined as coherent, if the incoming beam and the scattered one show no phase change or if the latter depends exclusively on the path length difference. With this assumption, the scattering process can be treated as the sum of individual scattered rays, each of them produced by a single electron building up the electron cloud. Let's take a look at an illustrative example, which can be treated in the framework of classical electrostatics, of an X-ray scattering process, known as Thompson scattering, where a single electron is involved.

Assume that a single electron at rest in the origin is hit by a plane wave travelling in the positive x-direction and polarized in the z-axis, the same as the direction of the electric field, as shown in Fig. 2.13. The interaction between the electric field and the point charge causes the electron to oscillate in z-direction, as described by applying Newton's 2nd law:

$$m\ddot{z} = -e \cdot E_{in} \tag{2.21}$$

As we know, a point charge moving in space generates a localized current that consequently radiates a spherical wave whose intensity as a function of the radial distance R is given by:

$$E_{sc} = E_{in} b \frac{e^{ik\cdot r}}{R} \tag{2.22}$$

where *b* is the defined as the scattering length and it is also a measure of the scattering power. Note that in the case of a single electron, the scattering length is equal to $r_e = 2.818 \times 10^{-5}$ Å, where r_e is the classical radius of the electron, also known as Thompson radius. Through the integration of the scattered intensity, $|E_{sc}|^2$, over all directions, the scattering cross section $\sigma = 8\pi r_e^2/3 = 0.665$ barn (1 barn = 10^{-28} m^2) is defined. From the point of view of the experimental realization of scattering experiments, the scattered intensity is recorded by means of a detector under a solid angle $d\Omega$, thus, in the end the measured quantity is $d\sigma/d\Omega$, defined as the differential scattering cross section. Therefore, since in every experiment the scattering geometry and in turn $d\Omega$ are well defined, the challenge is to express the differential scattering cross section in an adequate theoretical way.

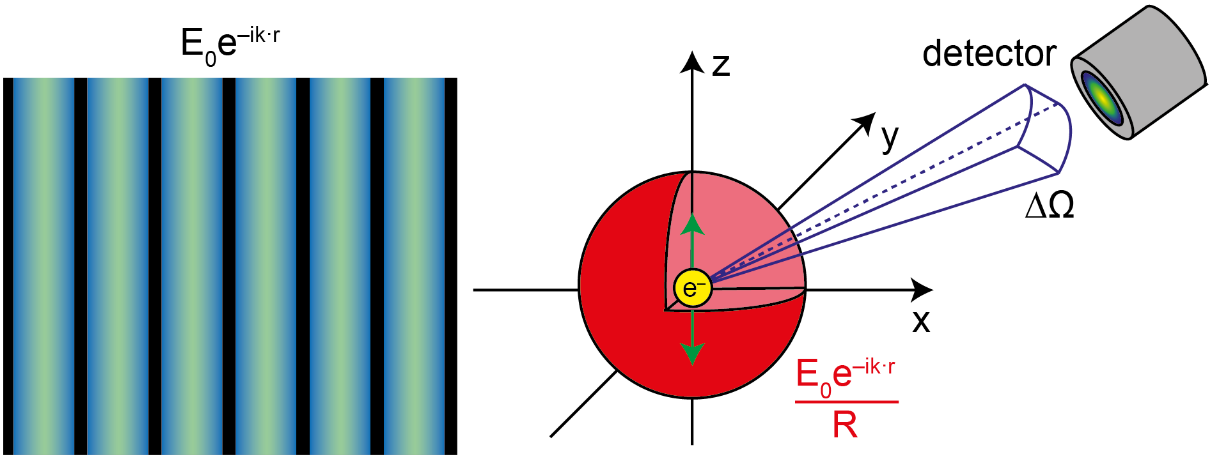

Fig. 2.13: A classic example of X-ray scattering: Thompson scattering. A plane wave travels in the positive x-direction and hits an electron at rest in the origin, which scatters a spherical wave, whose amplitude can be recorded by a moveable detector. Fig. was adapted from Abuillan.[177]

If we consider again the case of electrons bound to the nucleus, one can assume that the electrons are independent scatters and that the resulting scattered radiation is the sum of all scattered amplitudes added coherently. However, there two aspects that should be considered: on one hand, the positions occupied by the electrons in the electron cloud; on the other hand, the fact that the latter may cause interference phenomena. One possible way out is the application of the Born approximation that states, that the total scattering length can be expressed as $b = r_e \cdot f(q)$, where $f(q)$ is the atomic form factor, namely the Fourier transform of the electron density $f(q) = F(\rho(r))$, and q is the corresponding momentum transfer, defined as $q = 4\pi/\lambda \sin 2\theta$, where λ corresponds to the wave wavelength and θ is the scattering angle. A spring constant κ, which describes the binding strength to the nucleus, and a coefficient γ, which considers the damping caused by the surrounding electrons, can be added and Eq. 2.21 can be rewritten as:

$$m\ddot{z} + \gamma\dot{z} + \kappa z = -e \cdot E_{in} \tag{2.23}$$

The solution of this differential equation for the scattering length reads:

$$b = r_e(f + f' + if'') \tag{2.24}$$

where the two terms f' and f'' can be seen as a correction in the case of anomalous scattering. The first term f depends weakly on q and it corresponds to the atomic number Z at $q = 0$. f' and f'' are a correction to the real part and the adsorption term, respectively, and they are both wavelength dependent.

2.7.3.Refractive index

Following the definition of dielectric susceptibility from a point of view of classical electrostatics, the latter is proportional to the applied electric field, $P = \varepsilon_0 \cdot \chi \cdot E$, where χ is defined as the dielectric susceptibility and ε_0 is the electric permittivity of free space. Thus, if we substitute these terms in the differential Eq. 2.23 and solve it, an expression for the dielectric susceptibility can be derived as follows:

$$\chi = \frac{\rho_e e^2 E}{\varepsilon_0 m \omega^2} \tag{2.25}$$

From equation 2.25, the refractive index can be defined as follows, $n = (1+ \chi)^{1/2}$, and since χ is smaller than one, one can rewrite the refractive index as:

$$n = 1 - \frac{r_e \lambda^2 \rho_e}{2\pi} \tag{2.26}$$

In this case, the absorption is neglected. The connection between the electron density and the scattering length density (SLD) can be seen from equation 2.24. If one divides the scattering length, *b*, by the unit cell volume, then the refractive index can be written as:

$$n = 1 - \delta + i\beta \tag{2.27}$$

$$\text{with } \delta = \frac{r_e \lambda^2 \rho_e}{2\pi} = \frac{\lambda^2 SLD}{2\pi} \text{ and } \beta = \frac{\lambda\mu}{2\pi} \tag{2.28}$$

where δ and β are the real and the imaginary part of the refractive index, respectively, and μ is the linear absorption coefficient. The real part δ is related to the dispersion that characterizes the interaction strength between material and radiation. The imaginary part β is related to the attenuation coefficient (μ^{-1}) of the X-ray wave in the sample. To give an example, the electron density and the SLD of water (H_2O) can be estimated from its mass density (1 g/ml) that leads to a molecular volume of 29.9 $Å^3$ per one H_2O molecule. By dividing the number of electrons in a molecule of water by the molecular volume, the electron density of water is readily obtained to be 0.335 $e^-/Å^3$. Finally, by multiplying the classical radius of the electron, r_e, with the electron density of water, the SLD can be easily determined ($SLD_{water} = 9.45\times10^{-6}$ $Å^{-2}$). Since for most materials δ and β lie in the order of ~ 10^{-5} and ~ 10^{-8}, respectively, the refractive index in the X- ray region is slightly less than one. On the other hand, note that n is equal to unity in vacuum or air. Interestingly, the speed of light travelling through the material is defined as c_0/n which in this case would be larger than the speed of light propagating in vacuum. Indeed, this applies only to the phase velocity, defined as ω/k, whereas the group velocity, defined as dω/dk, which is the one responsible to carry the information, remains smaller than the speed of light in vacuum.

2.7.4.Reflection from a single smooth interface

As depicted in Fig. 2.14, consider an incident plane wave hitting a smooth interface between two media possessing refractive indices n_0 and n_1. Typically, two distinct phenomena will take place: in the first place, the incident beam is reflected from the interface back to medium 0 with a reflection angle $\alpha_f = \alpha_i$; secondly, the incident beam is refracted and propagates in medium 1 with a refraction angle α_t.

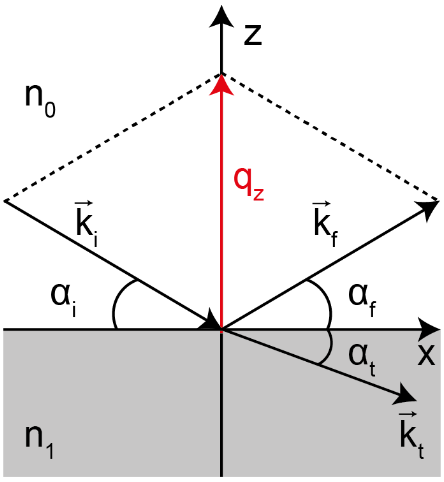

Fig. 2.14: Reflection and refraction of a wave on a smooth interface: Snell's law. The events taking place at the interface between two media possessing different refractive indexes is illustrated schematically. The Fig. was adapted from Abuillan.[177]

If we focus on the refraction of the incident beam at the interface, the phenomenon is well described by Snell's law as:

$$n_0 cos\alpha_i = n_1 cos\alpha_t \tag{2.29}$$

In case $n_1 < n_0$, we find that $\alpha_t < \alpha_i$, which means that the refracted beam moves away from the line normal to the surface. This means that as the incident angle of the incoming beam is further lowered, the refracted beam comes closer to the interface, until it becomes parallel to the interface and thus $\alpha_t = 0$. Therefore, the incident wave is totally reflected into medium 0. Under this circumstance, the incidence angle is called "critical angle" α_c. If the incidence angle α_i becomes smaller than α_c, the incident beam will eventually undergo a total external reflection. By applying the above-mentioned conditions and substituting into Eqs. 2.27 and 2.28, an expression of the critical angle is readily obtained as:

$$\alpha_c \approx \sqrt{\frac{2(\delta_1 - \delta_0)}{1 - \delta_0}} \approx \left(\frac{\lambda^2 r_e}{\pi}\right)^{\frac{1}{2}} \sqrt{\rho_{e_1} - \rho_{e_0}} \tag{2.30}$$

If we look carefully at Equation 2.30, one can deduce that the critical angle of total external reflection is directly proportional to the electron density difference between the two media, defined as "contrast". If we assume that medium 0 corresponds to air, then $\alpha_c \approx (2\delta_1)^{+1/2}$. If the typical value of δ for most materials is plugged-in ($\delta \sim 10^{-5}$), the critical angle for most materials is found to be in the range of mrad. To give an example, let's consider a slab of silicon, with an electron density of $\rho_{e,\,\mathrm{silicon}} = 0.71$ $e^{-}/Å^3$, hit by an incident wave whose wavelength is 1Å. In this case, the critical angle is $\alpha_c = 0.145°$.

From a theoretical point of view, in order to describe the propagation of a reflected wave from an interface one has to start from the Helmholtz equation that describes the propagation of waves in a medium with a certain dielectric constant i.e. refraction index as:

$$[\nabla^2 + k_0^2 n^2(r)]E(r) = 0 \tag{2.31}$$

The result of a wave hitting an interface between two media is again a plane wave of the form:

$$E_j = A_j e^{i(\omega t - k_j \cdot r)} \tag{2.32}$$

where A is the wave amplitude and the index j can be assigned the labels i, f and t, which refer to the incident, reflected and transmitted waves, respectively. By applying the conditions of the continuity of the electric and magnetic fields at the interface, where $z = 0$, one finds that the amplitudes of the electric field are determined by:

$$A_i + A_f = A_t \text{ and } A_i \overrightarrow{k_\imath} + A_f \overrightarrow{k_f} = A_t \overrightarrow{k_t} \tag{2.33}$$

By taking the ratios between the amplitudes of the reflected, transmitted, and incident beams, one can retrieve the reflection and transmittance coefficients, defines as $r_{01} = A_f/A_i$ and $t_{01} = A_t/A_i$, respectively. Furthermore, by expressing the wave vectors as $k_{z,j} = k_0 \cdot n_j \cdot \sin(\alpha_j)$ and by substituting them into equation 2.33, the reflection and transmittance coefficients can be rewritten in the form of the Fresnel coefficients:

$$r_{0,1}^F = \frac{k_{z,i}-k_{z,f}}{k_{z,i}+k_{z,f}}, \; t_{0,1}^F = \frac{2k_{z,f}}{k_{z,i}+k_{z,f}} \tag{2.34}$$

By taking the square modulus of the reflection, the reflectivity (R) is easily defined. As for the definition of the transmittivity (T), one can simply apply the conservation of energy which states that R + T = 1. In principle, the wave polarization , i.e. transverse or perpendicular, should be considered while deriving the expression of the Fresnel coefficients, because it leads to different definitions, as we found in the RICM section for Eq. 2.10 and 2.11. For instance, this applies when dealing with electromagnetic waves in the spectrum of visible light; on the contrary when dealing with X-rays, both polarizations yield the same outcome.

2.8.Introduction to X-ray photon correlation spectroscopy.

The aim of this section is to provide a general introduction to the experimental technique XPCS, that was extensively used for the investigations whose results are presented in Chapter 4. For this purpose, the following review articles were used as main sources: *Correlation spectroscopy with coherent X-rays* of Grübel G. and Zontone F., [62] and *Beyond simple exponential correlation functions and equilibrium dynamics in X-ray photon correlation spectroscopy* of Madsen *et al.*.[65]

The possibility of performing advanced techniques such as XPCS was made possible by the development of third generation synchrotron radiation sources that generate coherent X-ray beams whose intensity is several orders of magnitude higher than those previously available. The reason why scattering with coherent X-rays is of a great appeal is because it opens up the possibility for performing correlation spectroscopy with atomic resolution, to investigate complex dynamics in disordered systems on length- and time scales, that otherwise are beyond the capability of other techniques.

Consider a disordered system that is illuminated by an incoherent light source. The former will scatter the incoming radiation to form a random diffraction pattern, which is typically only an ensemble average of the correlations within the system. On the contrary, when the same disordered system is illuminated by a coherent light source, the system will scatter a random or "speckle-like" diffraction pattern, that carries precise information about the spatial arrangement of the disorder. If the speckle diffraction pattern is recorded over time, any fluctuation must reflect a modification in the spatial arrangement of the disorder, that can be connected to the direct measure of the underlying dynamics. In other words, the key feature of XPCS is its capability to investigate the dynamic properties of disordered systems by examining the temporal correlations of the photons scattered by the sample. The range of dynamics that can be investigated by XPCS spans typically in the low frequency domain from 10^6 Hz to 10^{-3} Hz and in the Q range from typically 1×10^{-3} Å^{-1} up to several Å^{-1}. In Fig. 2.15 a schematic overview of the frequency-wavevector range accessible to XPCS is presented in comparison to other techniques, that are often applied to investigate the complex dynamics in disordered systems.

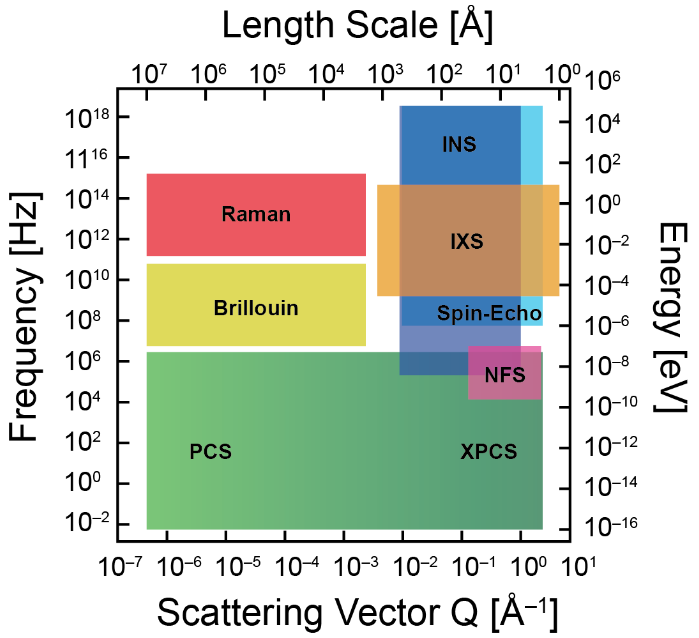

Fig. 2.15: Frequency.scattering vector accessible to XPCS compared to other techniques. The following complementary techniques were considered: photon correlation spectroscopy with visible coherent light (PCS), Raman and Brillouin scattering, inelastic neutron (INS) and X-ray scattering (IXS), neutron spin-echo and nuclear forward scattering (NFS). Fig. was adapted from Grübel *et al.*.[62]

2.8.1.Scattering with coherent X-rays

The discrete spectrum of intense synchrotron radiation is the result of the insertion of periodic magnet devices known as undulators, which are placed in the straight sections of a synchrotron storage ring. If we define F_c the fraction of the undulator flux that is transversely coherent, the latter is given by:[178]

$$F_c = \left(\frac{\lambda}{2}\right)^2 B \tag{2.35}$$

where B is the brilliance of the source whose unit is photons/s/mrad^2/mm^2/0.1% bandwidth. As discussed in the previous sections, a fundamental aspect of coherent scattering is the definition of a spatial and a temporal coherence. For instance, if the visibility of the interference fringes for a uniform monochromatic disk source of size s is bigger than 50 %, V > 50%, the transverse coherence length ξ_t of the photon beam is given by:[179]

$$\xi_t \approx \left(\frac{\lambda}{2\Delta\Theta}\right) = \left(\frac{\lambda D}{2s}\right) \tag{2.36}$$

Nowadays, the transverse coherence lengths to be usually found at third generation sources are 10 μm (horizontally) and 100 μm (vertically) for λ = 1 Å and a distance D ≈ 45 m from a source with angular source size ΔΘ = s/D. On the other hand, the temporal coherence of the beam can be defined by means of the longitudinal coherence length ξ_l which is strictly connected to the “degree” of monochromaticity of the beam and is given by:

$$\xi_l \approx \lambda\left(\frac{\lambda}{\Delta\lambda}\right) \tag{2.37}$$

To give an example and a general overview, in Table 2.1 the typical values for the relative bandwidth, longitudinal coherence length and the coherent flux for different optical configurations are presented.

	$\Delta\lambda/\lambda$	ξ_l (μm) (λ = 1 Å)	F_c ($B = 10^{20}$)
Si(220)	6×10^{-5}	1.7	1.5×10^{10}
Si(111)	14×10^{-5}	0.7	3.5×10^{10}
U (n = 3, N = 35)	1×10^{-2}	0.01	2.5×10^{12}

Table 2.1: Examples of typical bandpass, $\Delta\lambda/\lambda$, longitudinal coherent length, ξ_l, and coherent flux, F_c. The values are reported for different monochromators Si(220), Si(111) and a configuration using the intrinsic bandwidth $\Delta\lambda/\lambda = 1/nN$ of the third (n = 3) harmonic of an N = 35 periodic undulator. The Table was adopted from Grübel *et al.*[62]

In order to perform scattering experiments in which the sample is illuminated coherently, one of the requirements that must hold it that the maximum path length difference (PLD) of the waves going through the sample has to be equal or smaller than the longitudinal coherence length ξ_t. The maximum path length difference is defined as follows:

$$PLD \approx 2\mu sin^2\Theta \text{ or } PLD \approx 2W sin^2\Theta + \mathrm{d}\sin 2\Theta \tag{2.38}$$

in reflection or transmission geometry, respectively. Here μ is the adsorption length, W is the sample thickness, $\mathrm{d} \leq \xi_t$ is the beam size and Θ is the scattering angle. Note that Equation 2.38 sets a limit for the maximum wavevector transfer $Q_{max} = (4\pi/\lambda)\sin\Theta_{max}$ that is compatible with coherent illumination.

2.8.2.Disorder under coherent illumination.

In the introductory part of this section, it was mentioned that when a disordered system is illuminated by coherent light, this might give rise to a diffraction pattern, whose aspect appears to be random, which is usually referred to as 'speckle' pattern. To further elucidate this concept, let us consider the following scenario, in which a disordered sample is illuminated by a coherent beam of cross section ξ_t^2 and incident wave vector $\mathbf{k}$, and a scattered one with outgoing wave vector $\mathbf{k}'$. If we take into consideration any given point in the far field, we can express the instantaneous intensity as the square of a total field E($\mathbf{Q}$, t) as the following:

$$I(\boldsymbol{Q}, t) = |E(\boldsymbol{Q}, t)|^2$$

$$I(\boldsymbol{Q}, t) = \left|\sum\nolimits_n e^{i\boldsymbol{Q}\cdot\boldsymbol{r_n}(t)} f_n(\boldsymbol{Q})\right|^2 \tag{2.39}$$

Where, $f_n(\mathbf{Q})$ is the scattering amplitude of the n-th scatter located at position $\mathbf{r}_n(t)$, and $\mathbf{Q} = \mathbf{k}' - \mathbf{k}$ is the momentum transfer (in analogy with the momentum transfer q_z as shown in red in Fig. 2.14). Note that, the sum over n considers only the scatters included in the coherence volume, which is spanned by the transverse and longitudinal coherence lengths. Furthermore, we rely on the assumption that the beam is fully coherent. In order to avoid confusion, the Lorentz factor and the Thomson scattering length r_o^2 in Eq. 2.39 were omitted. It is straightforward that any measurement of the scattered intensity corresponds to a time average of the intensity $\langle I(\mathbf{Q}, t)\rangle_T$ recorded over the acquisition time T, however the latter does not imply the performance of any statistical ensemble average. In the case the acquisition is taken for a non-ergodic system, which possesses a static random disorder, $\langle I(\mathbf{Q}, t)\rangle_T$ will definitely show distinct and sharp 'speckles' as a function of $\boldsymbol{Q}$, whose angular size is defined as λ/ξ_t. On the other hand, when we are dealing with an ergodic system, in case the fluctuation time scales are very short compared to the counting time, the measured time average and the ensemble average, denoted by $\langle I(\mathbf{Q}, t)\rangle$, are perfectly equivalent to each other and can be exchanged one another. However, the only piece of information that can be retrieved from the recorded diffraction speckles are time averaged correlations within the sample, which are similar to those one would obtain by performing a scattering experiment using incoherent radiation, in other words they are featureless. To give an example, Fig. 2.16 shows a static speckle pattern from a porous silica gel (aerogel) taken with a CCD detector with a 22 μm pixel size and using an E = 8.2 keV coherent X-ray beam.

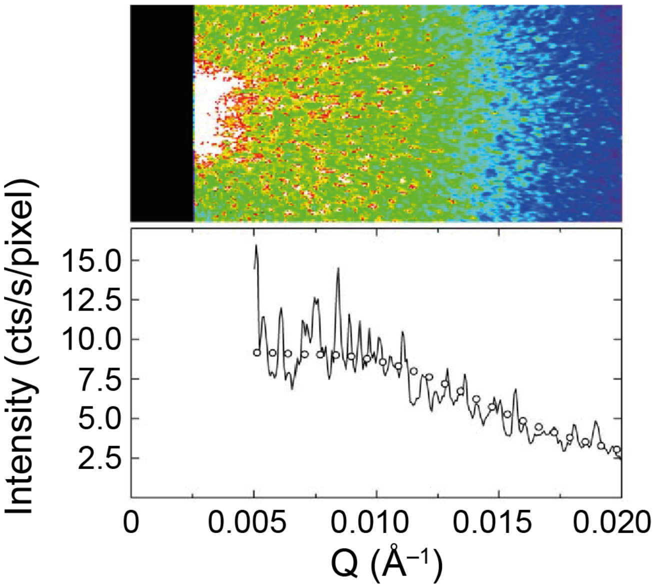

Fig. 2.16: Example given of a speckle pattern from a porous silica gel. The Fig. illustrates the random nature of the scattering intensity represented by the intensity variations (horizontal cut through the pattern; solid line) which are significantly beyond counting statistics. The open symbols indicate the ensemble averaged scattering $\langle I(\mathbf{Q}, t)\rangle$, calculated from the speckle pattern by radial averaging to yield the number of counted photons per second. Fig. was adapted from Grübel *et al.*,[62] and Abernathy *et al.*[180]

2.8.3.X-ray photon correlation spectroscopy (XPCS)

During the acquisition in an X-ray scattering experiment, the speckle pattern will change over time, reflecting the spatial rearrangement of the scatters within the sample, whose underlying dynamics is strictly connected to the intensity fluctuations of the speckles.

As hinted in Fig. 2.15, it is important to remark that an experiment performed by X-ray photon correlation spectroscopy recording the temporal intensity correlations is identical to a photon correlation spectroscopy experiment carried out with a visible coherent light (PCS), which is a well-documented technique in the literature. In order to extract information about the dynamics of the system, the normalized intensity correlation function $g_2(\mathbf{Q}, t)$ can be calculated from the temporal correlations. As we mentioned in the previous sections, in case the system is ergodic one can express the time averaged intensity correlation function in terms of the ensemble averaged time correlation functions of the scattered field ($\langle I(\mathbf{Q}, t)\rangle$):

$$g_2(\boldsymbol{Q},t) = \frac{\langle I(\boldsymbol{Q},0)I(\boldsymbol{Q},t)\rangle}{\langle I(\boldsymbol{Q})\rangle^2}$$

$$= 1 + A(\boldsymbol{Q})\frac{\langle E(\boldsymbol{Q},0)E(\boldsymbol{Q},t)\rangle^2}{\langle I(\boldsymbol{Q})\rangle^2} \tag{2.40}$$

where $A(\mathbf{Q})$ is defined as the contrast, which depends on the experimental the set-up. For instance, when performing scattering experiments using perfectly coherent chaotic light, A is equal to 1. On the other hand, the contrast becomes zero, $A \approx 0$, if one of the following occurs: in case the scattering is incoherent, for instance if the coherence volume << scattering volume, or alternatively if the detector used does not provide enough spatial resolution to discriminate at the angular scale of the speckles.

By applying the Siegert relation, the expression of the time correlation function $g_2(\mathbf{Q},t)$ in Eq. 2.40 can be formulated in terms of the normalized intermediate scattering function $f(\mathbf{Q},t)$ as follows:

$$g_2(\boldsymbol{Q},t) = 1 + A(\boldsymbol{Q})[f(\boldsymbol{Q},t)]^2 \tag{2.41}$$

where

$$f(\boldsymbol{Q},t) = \frac{F(\boldsymbol{Q},t)}{F(\boldsymbol{Q},0)} \tag{2.42}$$

and the expression of the intermediate scattering function, which is equivalent to the dynamic structure factor in the time domain, can be expanded as given by:

$$F(\boldsymbol{Q},t) = \frac{1}{Nf^2(\boldsymbol{Q})}\sum_n\sum_m \langle f_n(\boldsymbol{Q})f_m(\boldsymbol{Q})e^{i\boldsymbol{Q}[\boldsymbol{r}_n(0)-\boldsymbol{r}_m(t)]}\rangle \tag{2.43}$$

Where, N is the number of scatters, $\boldsymbol{r}_n(t)$ is the position of the nth scatter at time t, and the brackets imply an ensemble average and $F(\mathbf{Q},0)$ can be interpreted as the static structure factor.

It is important to highlight that the correlation function can be rewritten in terms of a simple exponential, in case the scatters motion follows free diffusion, which in other words means that their mean-square displacement is proportional to time, as follows:

$$g_2(\boldsymbol{Q},t) - 1 = Ae^{-2\Gamma t} \tag{2.44}$$

where $\Gamma(\mathbf{Q})$ is defined as the relaxation rate and $\Gamma(\mathbf{Q})^{-1} = \tau_c$ as the relaxation time. Note that, the factor 2, which appears in the exponent, takes into consideration the homodyne detection scheme, which requires that the scattered intensity is not mixed with a reference wave.

To give an example, let's consider a sample consisting of monodisperse, spherical particles undergoing Brownian motion. With the assumption that there is no interaction between particles, this means that their positions are uncorrelated and the cross terms ($n \neq m$) in Eq. 2.43 average to zero and $F(\mathbf{Q},0) = 1$. By recalling that the mean square value of the displacement for a free particle undergoing Brownian motion is $\langle[\mathbf{r}(0) - \mathbf{r}(t)]^2\rangle = 6D_o t$, where D_o is the free particle diffusion coefficient, which is given by:

$$D_o = \frac{k_B T}{6\pi\eta R} \tag{2.45}$$

where η is the shear viscosity of the surrounding medium. Thus, 2.42 simply becomes:

$$f(\boldsymbol{Q},t) = e^{-D_o Q^2 t} \tag{2.46}$$

The latter holds only in the absence of a particle-particle interaction. In case it exits an interaction between particles, one has to replace D_o in Equation 2.46 with a time- and wavevector-dependent diffusion coefficient, $D(\mathbf{Q},t)$. The latter is related to the initial slope $\Gamma(Q)$, that can be extracted from the measured intermediate scattering function $f^M(Q,t)$, as given in Eq. 2.47:

$$\Gamma(Q) = \lim_{t\to 0}\frac{d}{dt}[ln f^M(Q,t)] = -D(Q)Q^2 \tag{2.47}$$

and

$$f(\boldsymbol{Q},t) = e^{-D(Q)Q^2 t} \tag{2.48}$$

In Fig. 2.17 an example of a typical intermediate scattering function, previously normalized to the contrast is given.

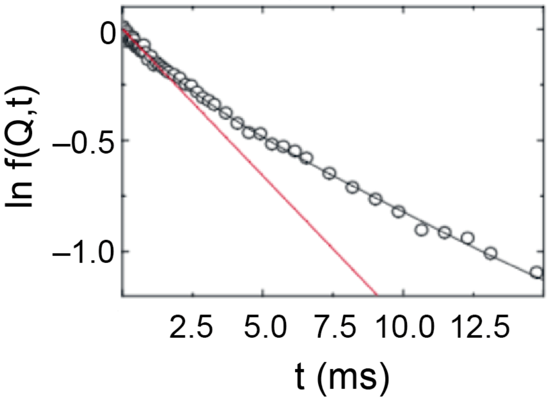

Fig. 2.17: Example of an intermediate scattering function and the extrapolation of $\Gamma(\mathbf{Q})$. The data was acquired for a concentrated suspension of colloidal poly(methyl methacrylate; PMMA) particles and were fitted with the cumulant expansion using up to fourth order terms (solid black line). The behavior at very short times is described by the first cumulant $\Gamma(Q)$ (solid red line) and it was extracted as given in Eq. 2.47. Fig. was adapted from Grübel *et al.*[62]

The way correlation functions can be calculated is by coupling a point detector to a digital autocorrelator that provides fast access to the correlation function over a wide range of correlation times (10^{-6} to 10^{3} s) at a single Q value. The data acquisition can be further improved by using two-dimensional position-sensitive detectors with appropriate spatial resolution (e.g. direct illuminated CCD cameras with 20 μm pixel size and about 40 % quantum efficiency) in order to obtain of a complete speckle pattern including the full range of Q values. From this complete speckle pattern, one can extrapolate the correlation functions for each pixel by taking the ensemble average over equivalent Q values. This aspect and how it is related to the dynamics in non-ergodic systems will be further explored in Chapter 3.

2.8.4.Example of XPCS applied to systems that deviate from simple diffusive behavior: colloidal gels.

For complex dynamics in condensed matter, diffusive motion obeying Eq. 2.44 is often the exception rather than the rule. Other systems, including capillary wave motion, collective diffusion near the colloidal glass transition and the dynamics in disordered soft solids such as gels and emulsion, have shown a process of slow, hyper-diffusive motion characterized by compressed, faster-than exponential correlation functions. All of these systems have in common an important feature, namely their out-of-equilibrium behavior. For these phenomena, the correspondence between $g_2(Q,t)$ and $f(Q,t)$ does not necessarily hold. Therefore, the characterization of the coherent scattering fluctuations beyond $g_2(Q,t)$ can provide important new insights in exploring complex dynamics of disordered systems.

One of the hot topics in recent XPCS research has been the microscopic dynamics in disordered soft solids, such as colloidal gels and concentrated emulsions. In these cases, the faster-than-exponential correlation functions that were observed were well approximated by a modification of Eq. 2.44, whose form is known as the Kohlrausch-Williams-Watts (KWW) function:

$$g_2(\boldsymbol{Q},t) - 1 = Ae^{-2(\Gamma t)^{\beta}} \tag{2.49}$$

with $\beta > 1$. Interestingly, a distinctive mark of these dynamics is a relaxation rate that depends approx. linearly on the wave vector, $\Gamma \sim Q$, implying hyper-diffusive, convective-like motion, in contrast to what was discussed in the previous section where we found that $\Gamma \sim Q^2$. Since this tendency has been observed in many different disordered soft materials, research scientists suggest the presence of a generic underlying mechanism that governs this peculiar hyper-diffusive motion, although no clear consensus about its microscopic origin has come to light. We report here two possible scenarios that can explain the dynamic behavior described by Eq. 2.49 of hyper-diffusivity. The first one makes use of a continuous time Lévy flight model with a power-law distribution of waiting, that enables β to become either $\beta < 1$ (compressed exponential) or $\beta > 1$ (stretched exponential). As a matter of fact, the hyper-diffusive dynamics came upon in a wide assortment of systems for which β has a Q-dependence that is accurately captured by the Lévy flight model.[71, 181] The second one considers a process of stress relaxation in which point-dipole stress fields create a distribution of strain velocities.[182] In this case as well, there are several systems for which $\beta \approx 1.5$ to support this scenario; interestingly, the latter was predicted by models invoking such stress relaxation.[183]

By now, it has been pointed out many times that these disordered soft solids exhibiting an out-of-equilibrium behavior, can increase the degree of difficulty to analyze the XPCS data to extract the correlation function. To be more specific, it shall be highlighted once more that the calculation of $g_2(\mathbf{Q},t)$ by means of Eq. 2.40 strictly requires that the dynamics is stationary over the entire acquisition process; in other words, no information is lost by performing a time-averaging of the quantities, because this is equivalent to the ensemble one, which is indicated by the angular brackets $\langle ... \rangle$.For out-of-equilibrium systems this implicit assumption might not hold; in this case, the correlation analysis must be carried out explicitly as a function of time, or 'age', and the time average in equation 2.40 must be replaced by an ensemble average performed using equivalent Q vectors. For this purpose, the use of an area detector with high spatial resolution is required.

Last but not least, in the framework of a multi-speckle time-correlation scheme, one can substitute the time-averaged correlation function with a two-time correlation function to explore the age dependence of the dynamics, as given by:

$$G(\boldsymbol{Q}, t_1, t_2) = \frac{\langle I(\boldsymbol{Q}, t_1) I(\boldsymbol{Q}, t_2) \rangle_\phi}{\langle I(\boldsymbol{Q}, t_1) \rangle_\phi \langle I(\boldsymbol{Q}, t_2) \rangle_\phi} \tag{2.50}$$

where the subscript ϕ specifies that the averaging is carried out on the ensemble of pixels included in the range of wave vectors, $|\mathbf{Q}| = Q \pm \Delta Q$, in which it is expected that the correlations exhibit negligible variations. The first research scientists, who made use of this two-time method coupled to XPCS, were Sutton and co-workers. For instance, this approach was applied on materials with non-stationary dynamics, such as alloys undergoing phase separation. Most remarkably, their efforts opened the way to prove that plotting the instantaneous correlations represents a reliable method for recognizing and characterizing rapidly evolving dynamics. For instance, this made the tests of critical scaling possible.[184]

Note that, one can retrieve the time correlation function in Eq. 2.40 simply by taking the average of $G(Q, t_1, t_2)$ at fixed delay time, $t = t_1 - t_2$

$$g_2(\boldsymbol{Q}, t) = \langle G(\boldsymbol{Q}, t_1, t) \rangle_{t_1} \tag{2.51}$$

As a conclusion to this Chapter, a representative example of the stress relaxation analysis in an aerogel is given. For more details about the experimental realization of the measurements, the reader is encouraged to consult the original paper of Madsen *et al.*.[65]

As presented in Fig.s 2.18 and 2.19, the multi-speckle technique was put in place to calculate the two-time correlation function, according to Eq. 2.50, and the time-averaged correlation functions, according to Eq. 2.51. Interestingly, the measurements were performed at two different time points ($\Delta t_1 = 5$ min and $\Delta t_2 = 180$ min) during stress recovery, which was induced by sectioning the sample, with the aim to investigate whether the sample "age" affects the underlying relaxation dynamics of the microscopic domains. If we take a look at the two-time correlation function, $G(Q, t_1, t_2)$ in the top-left panel, the colors represent the value of the point (t_1, t_2), with red being the maximum value ($G \approx 1.2$) and blue the smallest ($G \approx 1$), corresponding to those of the time-averaged correlation function, $g_2(Q, t)$ in the bottom-left panel. To better interpret the graph of $G(Q, t_1, t_2)$, one can define a delay time and a sample age as $t = t_1 - t_2$ and $\tau = (t_1 + t_2)/2$, respectively. This means, that the "main" diagonal spanned from the lower left to the upper right corner corresponds to $t = 0$ and all the other lines parallel to it are iso-t lines. By moving from the lower left to the upper right side of an iso-t line, the age τ increases linearly. On the other hand, in the normal direction of the iso-t lines, t varies, while τ remains constant. By looking at the left-upper panel, one can conclude that in these cases, the dynamics was rather stationary over the whole measurement.

As it was mentioned, $G(Q, t_1, t_2)$ can be time-averaged to yield $g_2(Q, t)$, as presented in the bottom left panel, where the Q-dependent time correlation functions were fitted (solid lines) using the KWW empiric model (Eq. 2.49). The fit parameters Γ and β are presented in the upper-right and lower right panels, respectively. At this point, several remarks should be made. In the first place, it is remarkable that the relaxation rate, Γ, decreased by more than a factor of 5 in the older sample. Secondly, the relaxation rate Γ appears to be linearly dependent on Q, as it was often observed for colloidal systems out-of-equilibrium. Last but not least, the shape of the time-averaged correlation functions appears to be highly compressed, which is reflected in the fact that $\beta > 1$, but in contrast to Γ it does not show any Q-dependency whatsoever. The fact that $\beta \approx 2$ for the entire Q-range and that it is independent from the sample's age, suggests that additional theoretical investigation is needed to explain the behavior of the underlying dynamics.

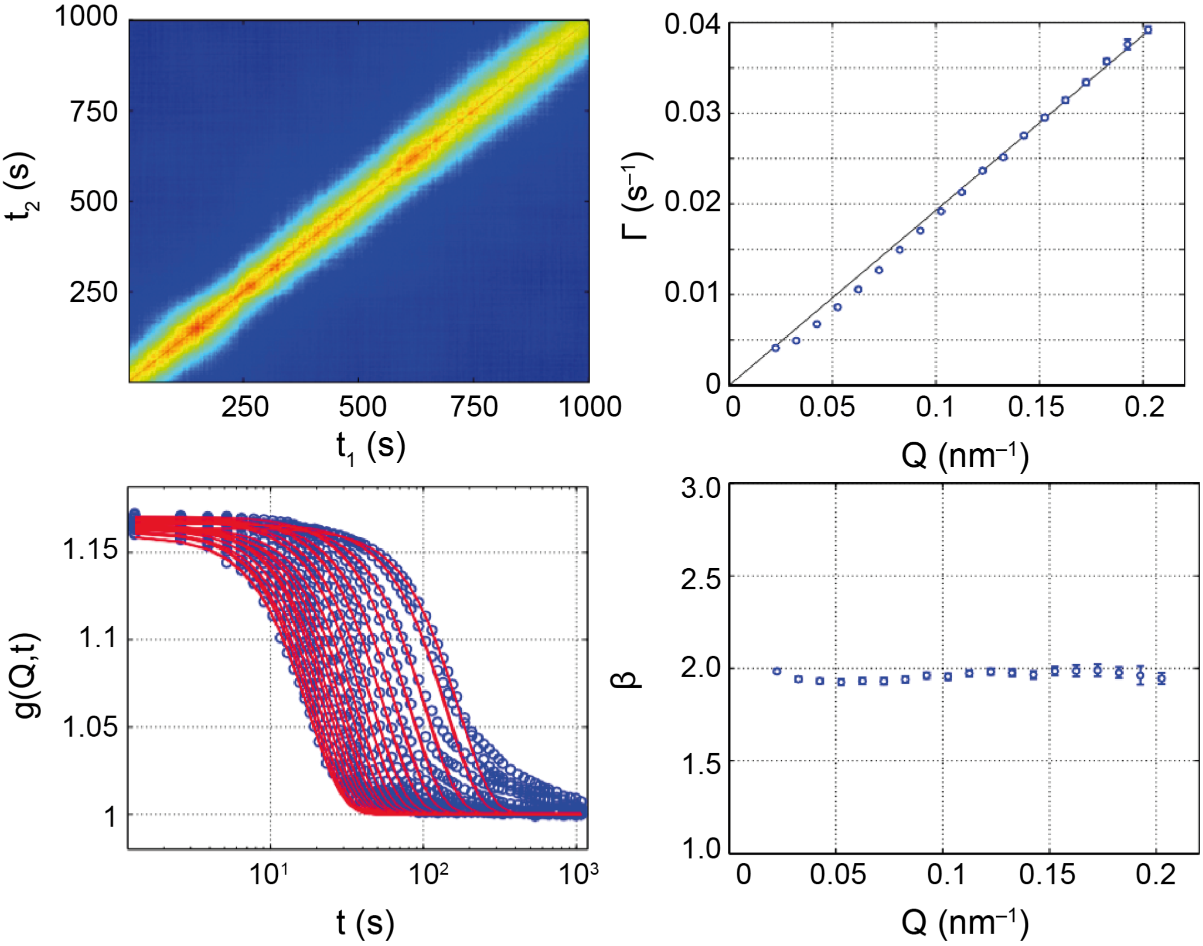

Fig. 2.18: Stress relaxation in an aerogel after Δt = 5 min stress induction time. Top-left panel: two-time correlation function $G(Q, t_1, t_2)$ for $Q = 3.25 \times 10^{-2}$ nm^{-1}; bottom-left panel: time-averaged correlation function over full Q-range. Solid lines represent fits with the KWW function. Top-right panel: fit results of the relaxation rate Γ, showing a linear Q-dependency ; Bottom-right: fit results of the KWW shape factor β, which remains close to 2 for the entire Q-range.

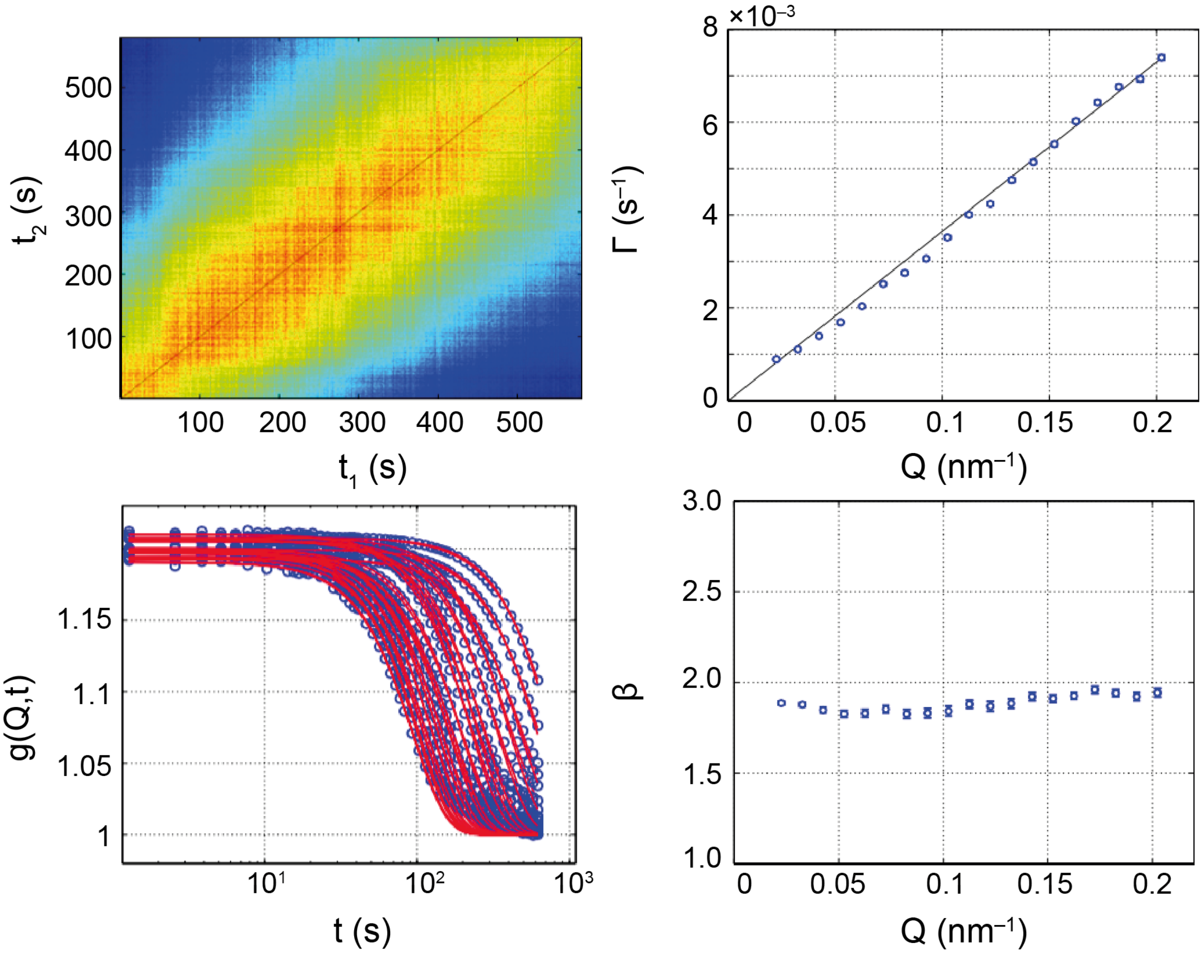

Fig. 2.19: Stress relaxation in an aerogel after Δt = 180 min stress induction time. Top-left panel: two-time correlation function *G*(Q, t_1, t_2) for Q = 3.25 × 10^{-2} nm^{-1}; bottom-left panel: time-averaged correlation function over full Q-range. Interestingly, the relaxation time increased almost by a factor 5 compared to the "young" gel. Solid lines represent fits with the KWW function. Top-right panel: fit results of the relaxation rate Γ, showing a linear Q-dependency ; Bottom-right: fit results of the KWW shape factor β, which remains close to 2 for the entire Q-range.

Chapter 3: Experimental Section

3.1.Materials

3.1.1.Chemicals

Unless stated otherwise, all other chemicals were purchased either from Sigma-Aldrich (Munich, Germany) or Carl Roth (Karlsruhe, Germany), and were used without further purification. Ultrapure water from a Milli-Q water purification system (Millipore, Molsheim, France) was used throughout all studies.

3.1.2.Proteins

Mucin protein from porcine stomach was purchased from Sigma-Aldrich: mucin type III (M1778) is a partially purified preparation following the previously reported protocol.[185] It should be noted that the nomenclature, following that of the manufacturer, has no correlation with the mucin type e.g. MUC2. Mucin type III from porcine stomach was biotinylated by NHS-ester coupling using EZ-Link NHS-PEG$_4$-Biotin (Thermo Scientific, Waltham, MA, USA).

NeutrAvidin was purchased from Invitrogen Molecular Probe (Darmstadt, Germany).

3.1.3.Lipids

Chloroform solutions of lipids were purchased from Avanti Polar Lipids (AL, USA): DOPC (1,2-dioleoyl-*sn*-glycero-3-phosphocholine) as zwitterionic (±), DOTAP (1,2-dioleoyl-3-trimethylammonium-propane) as cationic (+), DOPG (1,2-dioleoyl-*sn*-glycero-3-phospho-(1'-rac-glycerol)) as anionic (–) lipids, TexasRed-DHPE (1,2-dihexadecanoyl-sn-glycero-3-phosphoethanolamine) and Biotin Cap DOPE (1,2-dioleoyl-sn-glycero-3-phosphoethanolamine-N-(cap biotinyl)).

3.1.4.Polymers and surfactants

Chitosan (M_W = 50 – 190 kDa, degree of deacetylation 75 – 85 %) and sodium alginate (low viscosity) were purchased from Sigma Aldrich.

Polyglycerol polyricinoleate (PGPR) was obtained from DANISCO GmbH (Niebuell, Germany).

3.1.5.Enzymes

Protease from S*treptomyces griseus* was purchased from Sigma-Aldrich and neuraminidase (sialidase) from *Vibrio cholerae* was purchased from Roche (Basel, Switzerland).

3.1.6.Primary and secondary antibodies for immunofluorescent assays

Wheat germ agglutinin conjugated with Texas Red (WGA-Texas Red) were purchased from Thermo Fisher Scientific (Waltham, MA, USA). Rabbit monoclonal antibody to ZO-1 and goat anti-rabbit IgG conjugated with Alexa Fluor 594 were purchased from Abcam (Cambridge, United Kingdom), DAPI (4′,6-diamidino-2-phenylindole) from Roche Diagnostics (Mannheim, Germany), and mouse monoclonal antibody to gastric mucin and goat anti-mouse IgG conjugated with FITC from Sigma Aldrich.

3.1.7.Beads and particles

Kromasil 300-10-SIL silica particles (Ø ≈ 10 μm)) were purchased from Akzo Nobel (Amsterdam, the Netherlands).

Latex particles (Ø ≈ 10 μm) from Macherey-Nagel (Düren, Germany) and latex beads functionalized with carboxyl groups (COO^- latex, $\Phi \approx 10$ μm) were purchased from Polysciences Inc. (Warrington, PA, USA).

Silica nanoparticles (Ø ≈ 490 nm) that were used as tracers for SAXS experiments were a kind gift Y. Chushkin. Silica nanoparticles (Ø ≈ 25 nm) that were subjected to silanization and used for GISAXS experiments to increase the scattering signal at the o/w interface were purchased from C.I. Kasei Co, Tokio, Japan.

3.1.8.Chambers and membranes

Ibidi μ-Slides $VI^{0.4}$ were purchased from Ibidi (Martinsried, Germany).

Transwell inserts (∅ = 12 mm) equipped with porous membranes (ø = 0.4 μm) of polycarbonate (for Caco2) or polyester (for HT29 MTX) were purchased from Corning (NY, USA).

Polycarbonate membrane with a pore size of 50 nm for lipid vesicles extrusion was purchased from Avestin (Mannheim, Germany).

3.1.9.Bacteria and cells

Lactobacillus rhamnosus GG originated from human intestine was obtained from ATCC (Hørsholm, Denmark).

Cell lines HT29 MTX and Caco2 were obtained from Sigma-Aldrich and DSMZ (Braunschweig, Germany), respectively.

3.1.10.Buffers and cell culture media

TRIS buffer (20 mM TRIS, 150 mM NaCl, pH 7.4), Ca^{2+}- buffer (2 mM $CaCl_2$, 20 mM TRIS, 150 mM NaCl, pH 7.4) and PBS buffer (0.1 M NaH_2PO_4, pH 7.2) were used as electrolytes.

De Man, Rogosa and Sharpe (MRS) agar, Dulbecco's Modified Eagle's Medium (DMEM) w/Glutamax and Modified Eagle's Medium (MEM) were purchased from Sigma-Aldrich (Munich, Germany) and used without further purification. Silicon nitride cantilevers coupled to silica particles were purchased from NanoAndMore (Wetzlar, Germany).

3.2.Methods

3.2.1.Interfacial stress rheometry.

The description of the ISR technique was adapted from Herrmann *et al.*,[186] where the same experimental equipment was used.

The viscoelastic properties of the sol/gel transition of sodium alginate at the oil/water interface were studied by an interface stress rheometer (CIR-100, Camtel Inc. UK). In brief, a small De Nouy ring made out of Pt wire (cross-sectional diameter of 0.28 mm, ring diameter of 13 mm) was brought in contact with the water subphase and the position was recorded. Afterwards, the De Nouy ring was fully immersed into the subphase to wet it and subsequently it was raised back to the recorded position at the air/water interface. Sunflower oil containing $CaCl_2$ nanoparticles was spread drop-by-drop onto the subphase and measurements were started.

A defined oscillatory shear stress can be applied to a film at the interface by driving the ring's rotation at controlled frequency ω and driving amplitude γ. The amplitude and phase shift of the ring's resulting rotation is then monitored, from which the dynamic surface modulus, $G^*(\omega) = G'(\omega) + iG''(\omega)$, is deduced as a complex function of ω. The real part of G^* (the shear storage modulus, G' [mN m^{-1}]) is a measure of the elastic properties, and the imaginary part (the shear loss modulus, G'' [mN m^{-1}]) represents the viscous properties. G^* of the sodium alginate gel can be represented by the damping (D) and elastic (K) response of the instrument in the presence (D, K) and absence of the monolayer (D_0, K_0), respectively:

$$G' = -\frac{C_sC_0}{RA}(K - K_0) \tag{3.1}$$

$$G'' = \frac{C_sC_0}{RA}(KD - K_0D_f) \tag{3.2}$$

A is a geometric shape factor, C_s is the sensor constant, and C_0 and R are the galvanometric constant and the resistance of the instrument, respectively. For each measurement the corresponding reference signal of the o/w interface from the pure phases, i.e., the aqueous subphase and sunflower oil, was subtracted. The reference was measured with identical ring immersion depth. The rheology experiments were carried out at 293 K, and the frequency and amplitude of the oscillation was set constant at $\omega = 7$ Hz and $\gamma = 1$ mrad throughout this study, after confirming that the system remains within the linear response regime.

3.2.2.X-ray photon correlation spectroscopy.

Low viscosity sodium alginate was dissolved in Milli-Q water buffered with 20 mM Hepes. After complete dissolution, impurities were removed by filtration (pore size 0.45 µm).

For SAXS experiments, silica nanoparticles (Ø ≈ 490 nm) were dispersed in polyalginate 1.7 wt% aqueous solution to increase the scattering signal. Aqueous $CaCl_2$ was added to form the hydrogel, that was transferred and sealed into a 2 mm borosilicate capillary.

GISAXS experiments were performed in a sample chamber for liquid/liquid interfaces designed by O. Kolovanov, filled with alginate solution. To increase the scattering signal at the o/w interface, silanized silica nanoparticles in chloroform, were spread onto the surface. Following chloroform evaporation, a suspension of food-grade $CaCl_2$ nanoparticles in vegetable oil, synthesized as described elsewhere,[187] was added on top of the polyalginate 1.5 wt% aqueous phase.

Multispeckle X-ray photon correlation spectroscopy (XPCS) experiments were performed at the beamline ID10 at the European Synchrotron Radiation Facility (ESRF) in Grenoble, France. An X-ray beam was produced by three undulators tuned on third harmonic. The higher harmonics were suppressed by reflection from a double mirror with Pd coating. The monochromatic radiation of $E_{SAXS} = 21$ keV and $E_{GISAXS} = 22$ keV, $\lambda_{SAXS} = 0.59$ Å and $\lambda_{GISAXS} = 0.56$ Å was selected by a Si(1,1,1) monochromator (energy bandwidth $\Delta E/E \sim 10^{-4}$). The beam was then focused by Be compound refractive lenses. The spatially coherent part of the beam was selected by roller-blade slits opened to 10 × 10 µm, placed ~ 0.18 m upstream of the sample. The parasitic scattering produced by the beam-defining slits was removed by carefully adjusting a set of guard slits a few cm upstream of the sample. The resulting incident flux on the sample was $\sim 10^{10}$ photons per s per 100 mA.

A scheme of the experimental setup at ID10 is presented in Fig. 3.1.

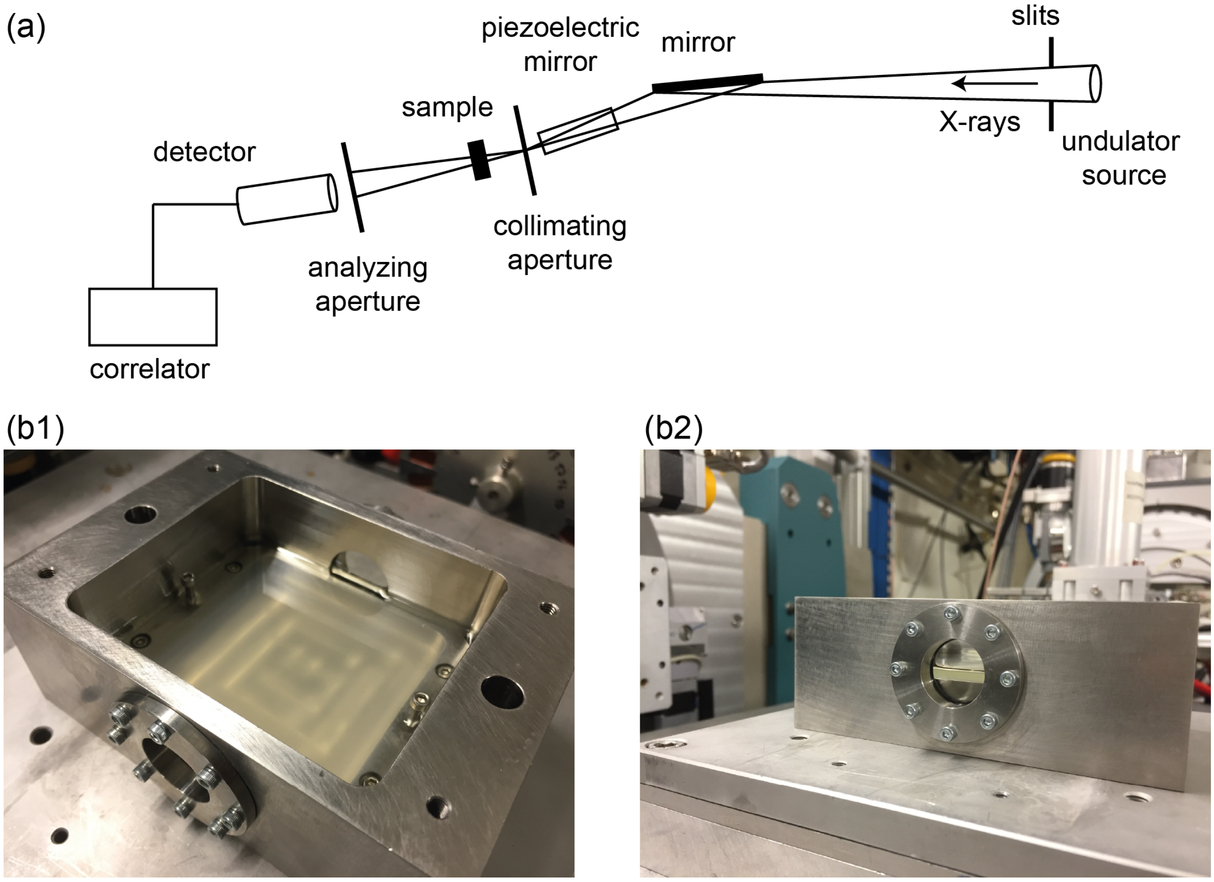

Fig. 3.1: GI-XPCS experimental setup at ID10. (a) Schematic setup of the ID10 beamline at ESRF for coherent X-ray scattering. Scheme was adopted from Grübel *et al.*[62].(b1) Top and (b2) side view of the metal trough designed by Dr. Konovalov to perform GI-SAXS experiments at the liquid/liquid interface.

Two-dimensional X-ray scattering speckle patterns were recorded using a photon counting area detector (Maxipix,[188] 55 µm pixel size with CdTe sensor) placed at distances $L_{SAXS} = 5.28$ m and $L_{GISAXS} = 4.23$ m. For SAXS, the sample-detector distance was chosen in order to cover the scattering intensity in a scattering vector range q of 0.02 – 0.94 nm^{-1}, where $q = 4\pi/\lambda \sin(2\theta/2)$ is the magnitude of the scattering vector, and 2θ and λ the scattering angle and the wavelength of the X-ray beam respectively.

For GISAXS experiments, the sample was illuminated at an incident angle of $\alpha_i = 0.0165°$, which is slightly below the critical angle of total reflection of the o/w interface ($q_{c,\ water} = 0.0217$ Å^{-1}, $q_{c,\ oil} = 0.0195$ Å^{-1}) $\alpha_c = 0.02°$ (beam footprint 0.01 × 3.4 mm^2, in the direction perpendicular and along the beam, respectively). The two-dimensional detector readout in angular coordinate (α_f, θ) can be transferred to a reciprocal space (q_z, q_y) map by

$$q = \begin{pmatrix} q_x \\ q_y \\ q_z \end{pmatrix} = \frac{2\pi}{\lambda} \begin{pmatrix} \cos(\alpha_f)\cos(2\theta) - \cos(\alpha_i) \\ \cos(\alpha_f)\sin(2\theta) \\ \sin(\alpha_f) + \sin(\alpha_i) \end{pmatrix} \tag{3.3}$$

where the weak q_x-dependence ($q_x << q_z$) is neglected.

A fast shutter, in synchronization with the area detector, was positioned before the sample to reduce the occurrence of beam radiation effects. The fact of having a fast shutter increased the achievable time scale of the measurement altogether because of the possibility to set 'sleeping times' between each time frame. On the other hand, by implementing these sleeping times the accessible short time scale was limited. For SAXS geometry, short scans were taken with an exposure time of 0.003 s up to 1000 frames, whereas long scans were performed by setting a sleeping time of 0.2 s between images. Several measurements were performed at different sample positions in order to check the consistency of the results. For GISAXS experiments, short scans were taken with an exposure time of 0.005 s up to 60000 frames, whereas long scans were performed by increasing the exposure time up to 0.1s and by reducing the number of frames to 40000.

3.2.3.XPCS analysis

As discussed in Chapter 2, XPCS makes the quantification of the temporal fluctuations of the microscopic reorganization at nanometric length scales possible. The quantity that can be extrapolated from the scattering patterns is the time averaged autocorrelation function, which can be calculated from the intensity fluctuations in the scattered signal, as given by:

$$g_2(\boldsymbol{q},t) = \frac{\left\langle \langle I_p(\boldsymbol{q},t_1) I_p(\boldsymbol{q},\ t_1+t)\rangle_p \right\rangle_{t_1}}{\left\langle \langle I_p(\boldsymbol{q},t_1)\rangle_p \right\rangle_{t_1} \left\langle \langle I_p(\boldsymbol{q},\ t_1+t)\rangle_p \right\rangle_{t_1}} \tag{3.4}$$

where $I_p(q, t_1)$ and $I_p(q, t_1 + t)$ correspond to the intensities measured on pixel p at time t_1 and $t_1 + t$, $\langle\ldots\rangle_p$ is the ensemble average over all the pixels of the detector which correspond to the same scattering vector q, and $\langle\ldots\rangle_{t1}$ is the temporal average over all times t_1. Note that at small and large delay times Eq. 3.4 becomes:

$$\lim_{t\to 0} g_2(\boldsymbol{q},t) = \frac{\left\langle \langle I_p(\boldsymbol{q},t_1)\rangle_p^{\ 2} \right\rangle_{t_1}}{\left\langle \langle I_p(\boldsymbol{q},t_1)\rangle_p \right\rangle_{t_1}^{2}} = 1 + A(\boldsymbol{q}) \tag{3.5}$$

$$\lim_{t\to \infty} g_2(\boldsymbol{q},t) = 1$$

respectively. As discussed in Chapter 2, A is the contrast and depends strongly on the ratio between the coherent and the scattering volume.[62] Furthermore, the intensity ACF reflects the underlying dynamics, since it is connected to the intermediate scattering function *via* the Siegert relation $g_2(\boldsymbol{q},t) = 1 + A(\boldsymbol{q})|f(\boldsymbol{q},t)|^2$. The condition under which this relation holds demands that the temporal average is equal to the ensemble average. For out-of-equilibrium systems, such as polymer gels, this requirement can be satisfied thanks to the use of area detectors.[189, 190] This in turn enables the correct sampling of the intensity distribution by taking the average over all the pixels that correspond to the same scattering vector. For a given $\boldsymbol{q}$ the ensemble average in eq. (3.2) was calculated by including all pixels of the detector that deviated less than $\boldsymbol{\delta q} = 2 \times 10^{-2}$ nm^{-1} from the nominal $\boldsymbol{q}$ value. In practice, one can picture that a correlation function is averaged over all pixels contained in a ring centered at the direct beam position with radius ~ $\lambda Lq/2\pi$ and thickness ~ $\lambda L\delta q/2\pi$ for SAXS or a rectangle with thickness ~ $\lambda L\delta q$ for GISAXS.

Autocorrelation functions were fitted using the Kohlrausch–William–Watts (KWW) model function

$$g_2(\boldsymbol{q},t) = B + Ae^{\left(-2\left(\frac{t}{\tau}\right)^{\beta}\right)} \tag{3.6}$$

where τ is the structural relaxation time and corresponds to the decay of $g_2(q, t)$, β is the shape parameter of the exponential function, B is the baseline and A is the contrast.[62]

The analysis of the XPCS data was performed using a program written by Dr. Yuriy Chushkin, a beamline scientist and member of the research group TROIKA02, that currently carries out its research activities at the ID10 of ESRF (Grenoble, France). The program, called *multitau*, can calculate the intensity autocorrelation functions following Eq. 3.4. *Multitau* receives as input the frames acquired during one run. As schematically presented in Fig. 3.2, the user can define which geometry has been used (SAXS or GISAXS), a region of interest in the scattering data by applying a mask, and finally can set an interval and the step size of the scattering vectors $\boldsymbol{q}$ to be analyzed. Once all the inputs are given, the correlator is started and calculates the autocorrelation functions for all $\boldsymbol{q}$ values of interest.

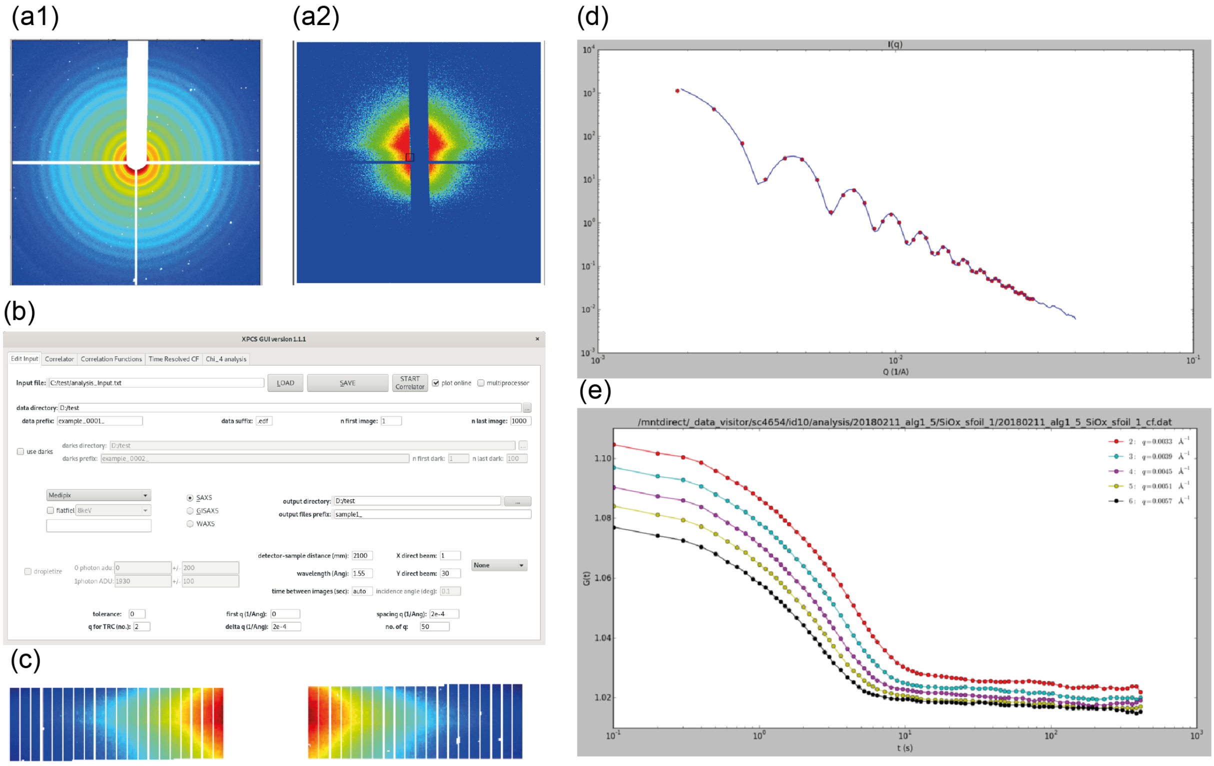

Input file: C:/test/analysis_Input.txt
☑ plot online ☐ multiprocessor
data directory: D:/test
data prefix: example_0001_
data suffix: .edf
n first image: 1
n last image: 1000
☐ use darks
darks directory: D:/test
darks prefix: example_0002_
n first dark: 1
n last dark: 100
Medipix
☐ flatfiel 8keV
● SAXS
○ GISAXS
○ WAXS
output directory: D:/test
output files prefix: sample1_
☐ dropletize
0 photon adu: 0 +/- 200
1photon ADU: 1930 +/- 100
detector-sample distance (mm): 2100
X direct beam: 1
None
wavelength (Ang): 1.55
Y direct beam: 30
time between images (sec): auto
incidence angle (deg): 0.1
tolerance: 0
q for TRC (no.): 2
first q (1/Ang): 0
delta q (1/Ang): 2e-4
spacing q (1/Ang): 2e-4
no. of q: 50

Fig. 3.2: Analysis of the collected XPCS data. Examples of the scattering pattern recorded for (a1) gelation of PA in bulk assessed *via* SAXS and (a2) gelation of PA at the liquid/liquid interface investigated *via* GISAXS. (b) User interface of the *multitau* software written by Dr. Chushkin. (c) Masked data set for which regions of constant $\boldsymbol{q} + \boldsymbol{\delta q}$ are defined where $g_2(q,t)$ is calculated according to Eq. 3.4. (d) Static intensity scattering function *vs.* $\boldsymbol{q}$ (e) Calculated time-averaged autocorrelation functions $g_2(q,t)$ for different scattering vectors.

3.2.4.Biotinylation of mucin.

Mucin type III (30 mg) was dissolved in a 3 mL portion of PBS buffer, mixed vigorously, and stored on ice. EZ-Link NHS-PEG4-Biotin (2 mg) was dissolved in a 170 µL portion of cold PBS. The latter solution (75 µL) was added to mucin solution, and the mixture was left on ice for 2 h. Afterwards the solution was transferred in a Slide-A-Lyzer 3200 MWCO dialysis cassette (Thermo Fisher Scientific) and dialyzed for 24 h by exchanging buffer every 6 h to remove all reagents in excess. During the dialysis process, the PBS buffer, in which the biotinylated protein was initially dissolved, was exchanged with TRIS buffer. After the removal from the dialysis cassette, the biotinylated mucin was stored at – 20 °C.

3.2.5.Vesicle preparation.

Stock solutions of lipids dissolved in chloroform were mixed at the desired molar ratio, and the mixture was dried in a stream of nitrogen. The remaining solvent residues were removed in vacuum over night at room temperature. The dried lipids were dissolved in TRIS buffer and sonicated for 45 min using a Misonix Sonicator 3000 (Farmingdale, NY, USA). Afterwards, the solution was centrifuged at 13.6 × 103 rpm for 10 min at 4 °C to remove the metal particles from the sonicator tip. The vesicle size was checked via DLS using a Zetasizer Nano ZS (Malvern, Malvern, UK).

3.2.6. Coating of silica particles with lipids.

Silica particles (83.8 mg) were washed three times with 1 mL TRIS buffer. The washed silica particles were incubated with a 1 mL portion of vesicle suspension (3.9 mg/mL) in an overhead rotator for 1 h at room temperature. Finally, the sample was washed 8 times with 1 mL TRIS buffer to remove free vesicles in supernatants.

3.2.7. Coating of COO^- latex beads with chitosan.

Chitosan (300 mg) was dissolved in 80 mL of a 1% v/v glacial acetic acid solution which was stirred until a clear solution was obtained. pH was adjusted to 5.7 using 1 M NaOH and the total volume was adjusted to 100 mL. A 16 µL portion of COO^- latex suspension was incubated with 0.3 wt% chitosan solution (1 mL) for 2 h, washed 3 times with TRIS buffer, and kept at 4 °C for further use.

3.2.8. ζ-potential.

ζ-potential measurements were performed in TRIS buffer using a Malvern Zetasizer Nano ZS (Malvern Instruments Ltd., UK) equipped with a He-Ne laser with a wavelength of 632.8 nm with a backscattering geometry at a constant scattering angle of 173°. Values for viscosity, refractive index and dielectric constant of TRIS buffer were chosen from the manufacturer's database (viscosity 1.0021 cP, refractive index 1.330 and relative dielectric constant 80.4). A refractive index of 1.45 was used for mucin proteins. After a short equilibration time (2 min) at 20 °C, the sample in a folded capillary cell was subjected to the measurement under a constant voltage (150 mV). Zeta potential measurements were repeated 3 times each consisting of 100 to 500 runs with a single run duration of 30 seconds. The zeta potential ζ was analyzed according the the Smoluchowski equation,[191] using the software provided by the manufacturer: $\zeta = \mu\eta\varepsilon^{-1}$, where μ is experimentally determined electrophoretic mobility, η viscosity and ε dielectric constant.

3.2.9. Immobilization of mucin on supported membranes.

The substrate was incubated with a 180 µL portion of DOPC/Biotin Cap PE vesicle (98/2) suspension (0.5 mg/mL) for 45 min at 40°C, and the unbound vesicles were removed by the rigorous rinsing with TRIS buffer. Following the incubation with NeutrAvidin solution (0.95 mg/mL) for 2 h, finally the sample was incubated with biotinylated mucin solution (2 µL) for 1 h, and the unbound mucin was removed by rinsing. To verify the enzymatic digestion of mucin, we also immobilized biotinylated mucin to membrane supported by SiO_2 particles (Ø ≈ 10 μm).[192] SiO_2 particles (20 mg) were mixed with a 1 mL portion of DOPC/Biotin Cap PE vesicle (98/2) suspension (3.9 mg/mL) for 1 h at room temperature in an overhead rotator. After rigorous washing, the particle-supported membranes were incubated with NeutrAvidin and biotinylated mucin solution, as described above. The successful immobilization of mucin was checked by incubation of BSA-passivated particles with WGA-Texas Red for 30 min at 37 °C.

3.2.10.Quartz Crystal Microbalance with Dissipation (QCM-D).

The silica crystal sensors were cleaned as previously described.[193] Prior to the measurement, the crystal surface was activated in an ozone cleaner for 30 min. Lipid vesicles were extruded through a polycarbonate membrane with a pore size of 50 nm to obtain small unilamellar vesicles. QCM-D measurements were performed at 37 °C using a Q-SENSE E4 system (BiolinScientifc AB, Sweden), recording the fundamental resonance frequency (5 MHz) and six overtones (3rd, 5th, 7th, 9th,11th and 13th). The flow rates were 20 μL/mL for the incubation with vesicles and proteins and 50 μL/min for rinsing. The changes in the resonant frequency Δf and dissipation ΔD were fitted with the Voigt model.[194] The solvent density (993 kg/m^3), the solvent viscosity (0. 69 mPa·s), and the protein layer density (1050 kg/m^3)[195] were set constant.

3.2.11.Enzymatic degradation of mucin.

To model the damage to mucin in intestinal bowel diseases, we enzymatically digested mucin coupled to supported membranes in two steps:[83] (1) sugar side chains were firstly shaved off by incubating the sample with a neuraminidase solution (1 U/mL) for 3 h at 37 °C, then (2) the protein core was digested by incubating the sample with a protease solution (30 U/mL) for 12 h at 37 °C. The digestion of mucin was monitored by QCM-D. The enzymatic digestion was further verified by subjecting the mucin coupled to particle-supported membranes to SDS-PAGE. Particle-supported membranes were incubated with (i) a neuraminidase solution (1 U/mL), (ii) a protease solution (30 U/mL), and (iii) a mixture of both for 12 h at 37 °C, followed by the centrifugation for 10 min at 5000 rpm. Laemmli buffer (65 mM TRIS, SDS 3.3 wt%, glycerin 5% (v/v), bromophenol blue 0.005 wt%, 5% 2-mercaptoethanol (v/v), pH 6.8) was added to membrane pellets (60 μL) and to the supernatant (1:1), and the samples were heated for 6 min at 95 °C. After cooling down, both membrane pellets and supernatants were subjected to SDS-PAGE (Mini-PROTEAN, BioRad, München, Germany) at 120 V (PowerEase500, Invitrogen, Waltham, MA, USA) for 90 min. The protein bands were detected following the silver staining protocol.[196]

3.2.12.Reflection Interference Contrast Microscopy (RICM).

All the micro-interferometry experiments were carried out at 37 °C, using an Axio Observer Z1 microscope (Zeiss, Oberkochen, Germany) equipped with an oil immersion objective lens (NA 1.25, 63

×, PH 3). A monochromatic light from a high-pressure metal halide lamp (λ = 546 nm) was selected with a band-pass filter for the observation. Two polarizers were inserted into the light path in orthogonal arrangement: one was placed in the illumination and the other in the detection path. A quarter-wave plate was inserted behind the front lens of the objective, and the Illumination Numerical Aperture (INA) was adjusted to 0.48 to record multiple interferences. 1000 consecutive images were recorded with an Orca-Flash4.0LT camera (Hamamatsu Photonics, Herrsching, Germany) at an exposure time of 30 ms, and subjected to the analysis.

The artifact from the lateral drift of particles was minimized by applying an edge detection filter to each image. After the radial integration, two consecutive maximum/minimum positions (E1, E2) closest to the center were selected. Under a quasi-normal light incidence, the simplified theory can be applied to perform the conversion of intensity I to relative height Δh_{pp} for all pixel positions (pp) in between E1 and E2:[197]

$$\frac{2I_{pp}-(I_{E1}+I_{E2})}{I_{E1}-I_{E2}} = \cos\left(4\pi n_{buffer}\frac{\Delta h_{pp}}{\lambda}\right). \tag{3.7}$$

In Fig. 3.3, the analysis process of the recorded videos is schematically illustrated, where the theoretical tools described in section 2.6.3 were used.

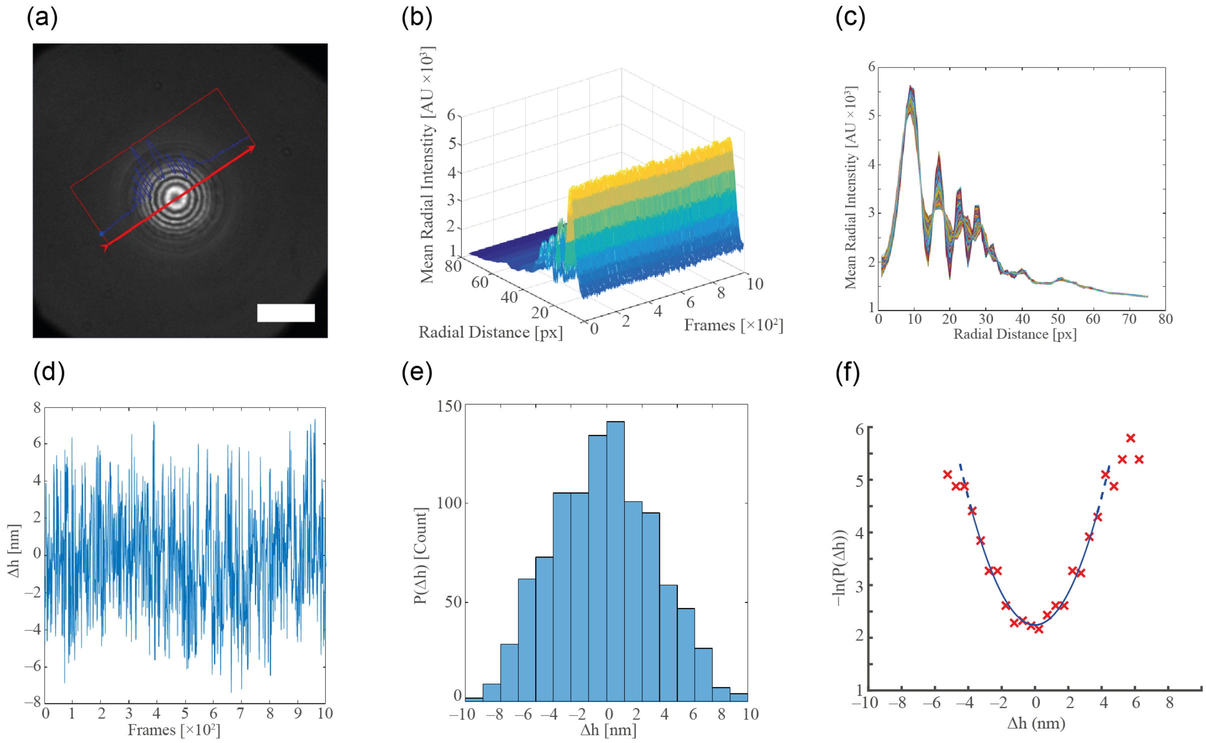

Fig. 3.3: Analysis of the RICM data. (a) Example of a typical RICM pattern observed for a latex or a SiO_2 microparticle. (b) The intensity of the Newtonian fringes is integrated radially and its evolution can be plotted over time. (c) For each time frame, the sine function is approximated in the linear interval between two adjacent maximum and minimum points, according to Eq. (3.7). (d) The height fluctuations of the pixels included in the chosen linear region are plotted *vs. t*, by subtracting the average height

value: $\Delta h = \Delta h_{pp} - \langle \Delta h_{pp} \rangle$. (e) A probability histogram of finding one pixel at a certain Δh, P(Δh), is constructed (f) Thanks to Boltzmann's inverse work functional theorem, the interaction potential between particle and substrate can be related to the probability P(Δh) *via* $\frac{V(\Delta h)}{\kappa_B T} = -\ln\big(P(\Delta h)\big) + const.$. In case of a weak, non-specific interactions, V(Δh) can be approximated with a harmonic potential of the form $V(\Delta h) = \frac{V''}{2}\Delta h^2$ where $V'' = 2\kappa_B T \frac{\partial^2 \ln\,(P(\Delta h))}{\partial h^2}\Big|_{\langle \Delta h \rangle_t}$ The latter can be interpreted as the spring constant of a harmonic potential and it is an indicator of how sharply the object is confined in a potential well.

3.2.13. Microfluidic experiments: wash-off and adhesion.

The shear stress generated at the bottom and in the center of a rectangular channel by a steady and laminar flow can be calculated as:[198]

$$\tau(x = 0, y = -h) = \eta \frac{\Phi}{q}\left\{\sum_{n=0}^{\infty} \frac{(-1)^n b\pi}{(2n+1)^2}\left(\frac{2}{\pi}\right)^3 tanh\left[(2n+1)\frac{\pi h}{2b}\right]\right\} \tag{3.8}$$

where *η* is the viscosity of the fluid, *Φ* is the total flow through the channel, *h* is the height of the channel, *b* is the half depth of the channel and *q* can be expressed as:

$$q = \frac{4}{3}hb^3 - 8b^4\left(\frac{2}{\pi}\right)^5\left\{\sum_{n=0}^{\infty}\frac{1}{(2n+1)^5} tanh\left[\frac{(2n+1)\pi h}{2b}\right]\right\}. \tag{3.9}$$

For the rectangular gaskets (*h* = 250 μm, *w* = 10 mm), the formula can be further simplified:

$$\tau(x = 0, y = -h) = \frac{12 \cdot \eta \cdot \Phi}{h^2 w}. \tag{3.10}$$

In Chapter 5, as an additional measure for the evaluation of interactions between particles and mucin layers, wash-off experiments were performed using microfluidic channels with a rectangular cross-section (ibidi μ-Slides VI$^{0.4}$). In brief: after incubating the silica particles coated with lipid membranes with supported membranes functionalized with mucin for 30 min, the shear stress was elevated from 0.03 to 0.34 Pa by pumping 5 mL TRIS buffer at increasing flow rates using a syringe pump (55-2316, Harvard Apparatus, Holliston, MA, USA). Snapshots were collected from 8 positions along the channel axis and subjected to the analysis.

In Chapter 6, the dynamic adhesion of LGG under flow and the flow-induced detachment of LGG under controlled shear stresses were quantitatively evaluated by transferring the porous polymer membrane covered with a cell monolayer into a microfluidic chamber with a rectangular gasket (Warner Instruments, Hamden, CT, USA).

To observe the dynamic adhesion of LGG on a "blank" cell monolayer, called "adhesion experiments" in the following chapters, DAPI-stained LGG were diluted in cell medium to a concentration of 4.7 × 10^7 cells/ml. Afterwards, 5 ml of medium containing bacteria cells were pumped into the chamber at increasing flow rates using a syringe pump (55-2316, Harvard Apparatus, Holliston, MA, USA). After each measurement, the sample was replaced by the new one. For the flow-induced detachment of the "pre-occupied" cell monolayer, called "wash-off experiments" in the following chapters, the DAPI-stained LGG were incubated on the cell monolayers for 30 min. Subsequently, the shear stress was elevated step-wisely from 0.03 to 1.2 Pa by pumping 5 ml of cell medium at increasing flow rates. Snapshots were collected from 8 positions along the channel axis and subjected to the analysis.

3.2.14.Cell culture.

LGG were cultured for 18 h at 37 °C in MRS broth, harvested by centrifugation at 3500 g for 15 min and washed three times in phosphate buffered saline (PBS, pH 7.4). For quantitative determination of CFU, 100 μl of a serial diluted bacteria suspension were plated on MRS broth agar dishes, incubated for 48 h at 37 °C in an anaerobic jar, and the number of colonies were determined by the plate count method. For the experiments in microfluidic chambers, LGG were fluorescently stained with DAPI (1:200) and incubated for 20 min at room temperature. Caco2 cells and HT29 MTX were seeded in 12 wells Transwell culture dishes at 7.5×10^4 cells/well and cultured in DMEM containing 5 wt% fetal calf serum (Life Technologies, Carlsbad, CA, USA). The cells were cultured for 21 d to allow apical-basal polarization and establishment of tight junctions, which was confirmed by measuring TEER.

3.2.15.Immunofluorescence staining.

Prior to the immunofluorescence staining, the porous polymer membranes supporting the cell monolayer were cut from the Transwell inserts, and transferred to a 6 wells plate. The cells were fixed with 4 wt% formalin (20 min), then treated with 0.1 wt% TRITON 100X (20 min) and 3 wt% BSA (2 h) at room temperature. BSA in excess was removed down to 1 ml and Tween20 was added to 0.01 wt% together with the primary monoclonal antibodies, anti-mucin (1:100) and anti-ZO-1 (1:200). Cells were incubated overnight at 4 °C. Subsequently, the samples were washed with 0.1 wt% Tween20, followed by incubation with the dye-conjugated secondary antibodies for 1 h at room temperature. Cell nuclei were stained by incubation with DAPI (1:200) for 10 min. After the whole staining procedure, the polymer membranes were mounted on glass slides, and subjected to the imaging with a Nikon C2 Plus confocal microscope (Düsseldorf, Germany). It should be noted that the immunofluorescence staining of tight junction proteins requires the removal of mucin by the treatment with N-acetyl cysteine before fixation, in order that the access of anti-ZO-1 is not blocked by the mucin layer.[199]

3.2.16.Particle-Assisted AFM indentation.

The elasticity of intestinal epithelial monolayer was determined by indentation of cell monolayers using a NanoWizard AFM50 (JPK Instruments, Berlin, Germany). Since mucin forms a hydrogel with unknown characteristic mesh sizes, we used the cantilevers (spring constant: 0.08 N/m) coupled to SiO_2 particle ($\varnothing$ = 10.2 μm) in order to minimize artifacts generated by indenting the voids and defects. Porous polymer membranes covered by cell monolayers were excised from the culture well and glued onto round glass coverslips (Ø = 25 mm). All the experiments were performed in a sterile medium at 37 °C. Indentation curves ($N > 50$) were measured at different positions with an indentation speed of 2 µm/s. The effective bulk elastic modulus E of the cell surface were calculated by fitting the force–indentation curves using the Hertz model for a spherical indenter:[200]

$$F = \frac{4E\sqrt{R}}{3(1-\nu^2)}\delta^{3/2}. \tag{3.11}$$

F is the force, δ the indentation depth, ν the Poisson ratio (0.5), and R the radius of SiO_2 particles (5.1 µm). The results of the fitting are presented by the median and the standard errors.

Results and Discussion

In the next three Chapters, the results obtained during the course of the doctoral studies will be presented and discussed.

Chapter 4: Interfacial gelation dynamics of sodium alginate at the o/w interface probed by GI-XPCS.

The majority of the data presented in this chapter was summarized in an article to be submitted to a peer-reviewed journal:

Title:

"Liquid/liquid interface dynamics probed by grazing incidence XPCS"

Federico Amadei[1], Wasim Abuillan[2], Akihisa Yamamoto[4], Judith Thoma[1], Esther Kimmle[1], Julian Czajor[1], Yuriy Chushkin[3], Oleg Konovalov[3] and Motomu Tanaka[1,4]

[1] Physical Chemistry of Biosystems, Institute of Physical Chemistry, Heidelberg University, D69120 Heidelberg, Germany

[2] Department of Fundamental Engineering, Institute of Industrial Science, The University of Tokio, 4-6-1 Komaba, Meguro, Tokyo 153-8505, Japan

[3] European Synchrotron Radiation Facility, CS 40220, 38043, Grenoble, France

[4] Center for Integrative Medicine and Physics, Institute for Advanced Study, Kyoto University, 606-8501 Kyoto, Japan

Author Contributions:

F.A. performed all aspects and data analysis of the experiments presented in this chapter. W.A., A.Y., J.T., E.K., J.C. helped during the stay at the beamlime ID10 at ESRF to perform the X-ray scattering experiments. W.A. and A.Y. especially gave an intellectual contribution to the interpretation and discussion of the results. Y.C. contributed crucially to the realization of the experiment at the beamline ID10 and also wrote the program to analyze the acquired data. O.K. designed the sample chamber to perform GI-XPCS at the liquid/liquid interface. M.T. participated in the conception and design of the experiments described here and was involved in manuscript writing.

4.1.Summary

Albeit the structural evolution accompanying the sol-gel transition of sodium alginate has been largely investigated, no studies have been reported on the corresponding dynamics of interfacial gelation at the o/w interface. Several pioneering studies suggested that grazing incidence X-ray photon correlation spectroscopy, GI-XPCS, is one of the new challenges to shed light on the dynamics of soft interfaces. In this study, interfacial gelation of sodium alginate at the o/w interface and the temporal evolution of the underlying dynamics at the nanometric length scale were investigated by means of GI-XPCS. In a first step, the sol-gel transition of alginate was detected in bulk (SAXS-XPCS) by looking into the dynamics of silica nanoparticles used as tracers in the polymer matrix. The results clearly indicate that the characteristic relaxation time calculated from the autocorrelation functions of the silica tracers strongly depends on the cross-linker concentrations. Subsequently, interfacial stress rheometry was used to monitor the dynamics at the interface, in which the change in storage and loss moduli of sodium alginate at the o/w interface was monitored *vs* delay time, after the injection of $CaCl_2$ nanoparticles suspended in oil. The crossing of the storage modulus over the loss modulus was a clear indication that $CaCl_2$ nanoparticles condensed at the interface and induced the gelation of sodium alginate, that reached the saturation level after approx. 10 h of reaction. Once the time window of the experiments at the o/w interface was set, GI-XPCS was performed by spreading hydrophobic SiO_2 nanoparticles that remained confined at the o/w interface and increased the scattering signal. The autocorrelation functions calculated from the scattering intensities at different times after cross-linker injection clearly indicated a significant change in the characteristic relaxation time over one order of magnitude. The obtained results served as a proof of concept with respect to GI-XPCS applied to soft liquid-liquid interfaces. Further investigations are necessary to shed light on the kinetics of interface gelation from the viewpoint of interface dynamics.

4.2.Results and Discussion

4.2.1.Gelation of polyalginate in bulk.

Prior to the measurements to investigate the gelation of PA at the liquid/liquid interface, the gelation in bulk via SAXS-XPCS using glass capillaries was tested, where silica nanoparticles were used as tracers, as illustrated in Fig. 4.1. Interestingly, in the absence of cross-linkers (0 mM, turquoise curve) the dynamics of the system is too fast and the initial plateau cannot be captured due to the mechanical constraints of the opening and closing times of the fast shutter placed between the X-ray source and the sample, that cannot be decreased beyond a threshold of 2 ms. Nevertheless, the autocorrelation function could be fitted using the KWW empirical function (Eq. 3.6) and the characteristic decay time was found to be $\tau_{0\ \mathrm{mM}} = (4.8 \pm 0.1) \times 10^{-2}$ s. Similar to the previous case, the dynamics of alginate gel prepared with a low concentration of cross-linkers (10 mM, light blue curve) is fast although a shoulder-like feature starts appearing and the characteristic decay time is almost twice as much as the one in the sol state, $\tau_{10\ \mathrm{mM}} = (9.5 \pm 0.2) \times 10^{-2}$ s. However, when the polyalginate gel was prepared with a high concentration of cross-linkers (100 mM, dark blue curve) the dynamics slows down dramatically and the decay time of the autocorrelation function increases of a factor approx. 200, $\tau_{100\ \mathrm{mM}} = 22.8 \pm 0.3$ s. Interestingly, this increase is accompanied by an increase in the form factor β from $\beta_{10\ \mathrm{mM}} = 0.95 \pm 0.03$ to $\beta_{100\ \mathrm{mM}} = 1.42 \pm 0.03$, denoting a crossover from a stretched ($\beta < 1$) to a compressed ($\beta > 1$) evolution of the decay of the ACFs. A similar crossover has been detected in bulk for other polymer gels such as methylcellulose.[57]

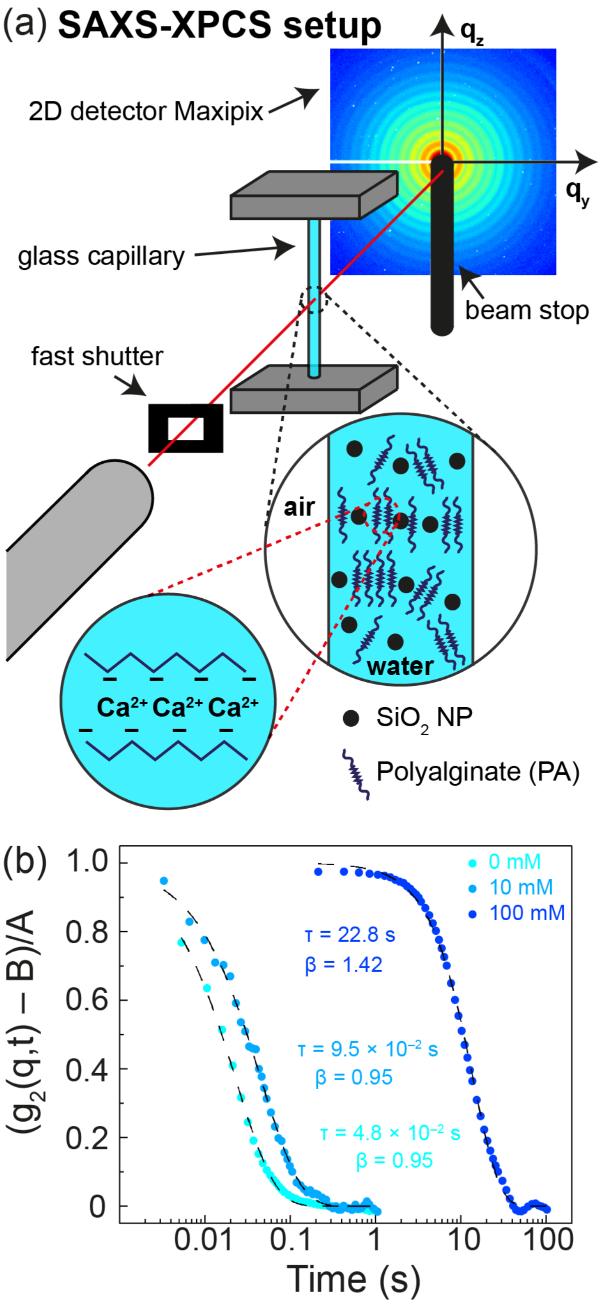

Fig. 4.1: Gelation in bulk of PA 1.7 wt% proved by SAXS-XPCS. (a) Scheme of the experimental setup, where SiO_2 nanoparticles were used as tracers for gelation. (b) Selection of intensity autocorrelation functions (ACFs) in the absence (turquoise), low concentration (light blue), and high concentration (dark blue) of cross-linkers. The increase in decay time τ and shape parameter β is dependent on cross-linkers concentration and is a clear sign of the gel formation in bulk.

4.2.2.Gelation of PA at the o/w interface investigated by means of ISR.

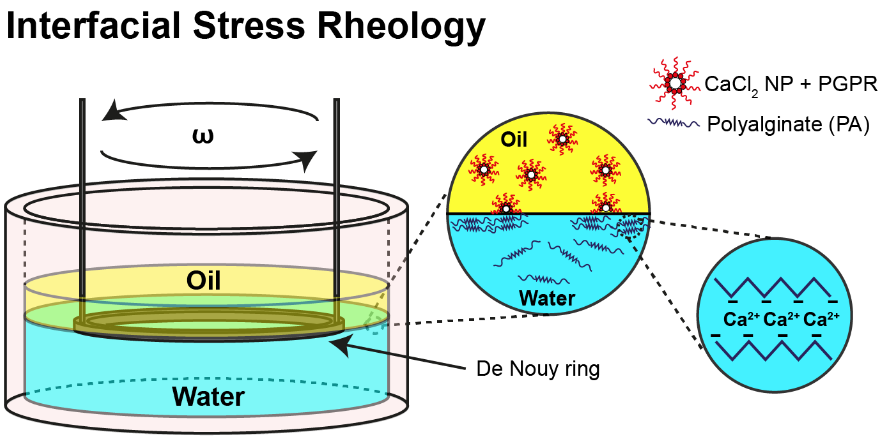

Fig. 4.2: ISR experimental setup. The experimental setup of ISR to investigate the gelation of PA at the o/w interface is schematically illustrated. A De Nouy Pt ring placed at the o/w interface oscillates with frequency $\omega = 7$ Hz and amplitude $\gamma = 1$ mrad. The zoom-in inset displays the condensation of the $CaCl_2$ NP at the interface.

In Fig. 4.2 the experimental setup of the ISR technique which was used to investigate the gelation of polyalginate at the liquid/liquid interface is presented. To be able to follow it over hours, the gelation of polyalginate was slowed down by adding $CaCl_2$ nanoparticles suspended in oil, therefore making it a diffusion-limited process, where the nanoparticles condense at the interface, driven by the action of the surfactant. To determine a time window during which the gelation of polyalginate at the o/w interface must be followed, the interfacial stress rheometry experiments were first put in place, whose results are reported in Fig. 4.3. After the addition of the cross-linkers suspended in oil, the formation of a gel at the liquid/liquid interface was observed by naked eye as shown in panels (a1) and (a2). For instance, a turbid and milky layer was formed above the liquid/liquid interface, that in the camera pictures was highlighted with a dotted line, after 12 h of delay time.

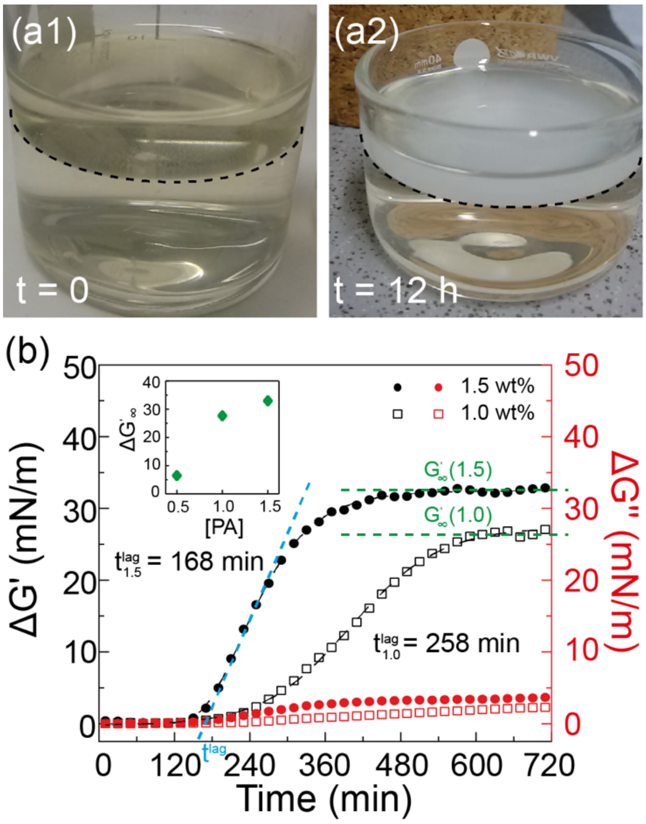

Fig. 4.3. Interfacial gelation of PA unraveled by ISR. Camera snapshots of the sample before (a1, t = 0 h) and after the gelation (a2, t = 12 h). PA gel can be identified as a turbid layer near the o/w interface indicated by a black broken line in (a2) (b) Change in dynamic elastic modulus ($\Delta G'$, black) and viscous modulus ($\Delta G''$, red) plotted as a function of time. [PA] = 1.0 wt% (squares) and 1.5 wt% (circles). Black lines correspond to sigmoidal fits to $\Delta G'$(t), while the blue line shows the linear extrapolation yielding the lag time t^{lag}. The inset shows the saturation levels ($\Delta G_\infty'$) vs. [PA].

To gain further insight, not only qualitatively but also quantitatively, the gelation of PA prepared at different concentrations (1.5 and 1.0 wt%) was monitored via ISR and the experimental results are presented in Fig. 4.3 (b). The fact that after an initial lag time the elastic modulus $\Delta G'$ increased and went beyond the level $\Delta G''$ was in both cases a clear sign of a sol-gel transition. To extrapolate the kinetic parameters, the curves were analyzed using the model reported by Shoffner et al.[201], which is a modified sigmoidal function that takes into account the curve asymmetry, as given by:

$$\Delta G'(t) = \Delta G'_0 + \frac{\Delta G'_\infty}{(1 + v exp^{-k(t-t_m)})^{1/v}} \tag{4.1}$$

where $\Delta G'$(t) is the magnitude of the difference in the elastic modulus at time t, $\Delta G'_0$ is the baseline level of the lag phase, $\Delta G'_\infty$ is the saturation level (plateau) of the progress curve, t_m is the inflection time at which the growth rate reaches its maximum, v is a parameter that alters the asymmetry of the curve and k is the rise rate. The lag time can be then extrapolated in terms of the empirical parameters by:

$$t_{lag} = t_m - \frac{1 + \nu}{k} \tag{4.2}$$

Interestingly, it was found that the lag time was inversely proportional to the polymer concentration, for instance $t_{lag\ 1.5\%}$ = 168 min and $t_{lag\ 1.0\%}$ = 258 min. On the other hand, the saturation level was directly proportional to [PA], namely $\Delta G'_{\infty\ 1.5\%} = 32.4 \pm 0.1$ mN/m and $\Delta G'_{\infty\ 1.0\%} = 27.7 \pm 0.3$ mN/m. Both findings can be explained and understood if one considers that the number of crosslinking points, where the entrapment of the Ca^{2+} ions in the guluronic acid blocks takes place, is directly proportional to the polymer concentration, therefore making the gelation process faster and the resulting gel “stiffer”. Furthermore, thanks to these findings, the time window for the GI-XPCS measurements could be set up to 600 min, time after which the gelation process at the interface is saturated.

4.2.3.Gelation of PA at the o/w interface unraveled *via* GI-XPCS.

In Fig. 4.4, the experimental setup of the GI-XPCS is presented. Following the idea used for SAXS-XPCS, SiO_2 NP were used to increase the scattering signal at the interface; however, in this case chemically modified NP, that were confined at the o/w interface because of their hydrophobic surface, were put in place.

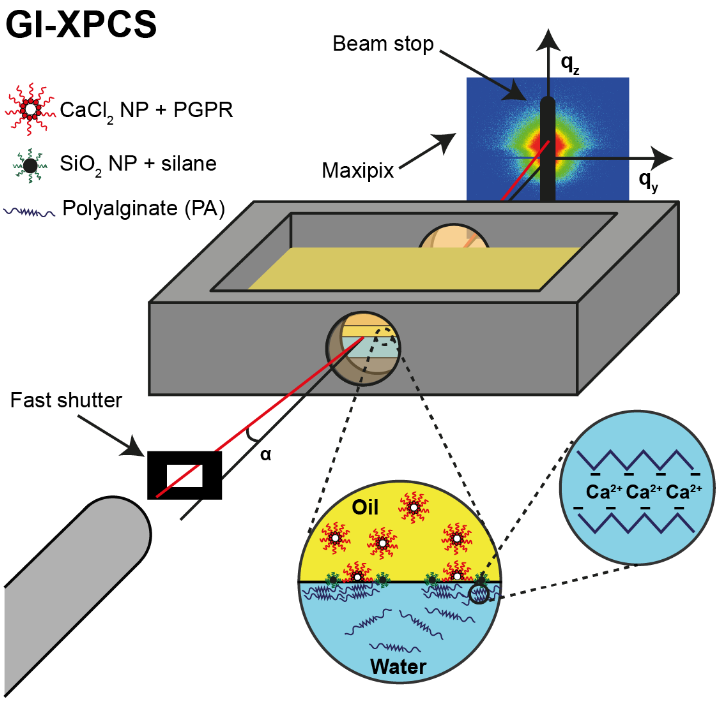

Fig. 4.4: GI-SAXS experimental setup. The experimental setup of GI-SAXS to investigate the gelation of PA at the o/w interface is schematically illustrated. The trough designed by Dr. Konovalov for experiments at the liquid/liquid interface was used. The trough was filled with a solution of aqueous

PA, on top of which SiO_2 NP were spread to increase the scattering signal. Finally, $CaCl_2$ NP suspended in oil were used as cross-linkers to trigger the interfacial gelation process.

Fig. 4.5 (a) shows a selection of normalized intensity ACFs $(g_2(q,t) - B)/A$ measured at different delay times after the addition of the oil phase containing the $CaCl_2$ nanoparticles on top of an aqueous solution of PA 1.5 wt%. In contrast to what was previously reported for the gelation of PA in bulk, at the initial time $t = 0$, when the system is in the sol phase still, the dynamics of the system at the liquid/liquid interface can be captured and the exponential decay is visible. This behavior might be due to the fact that the hydrophobic SiO_2 nanoparticles are confined in a thin, two-dimensional layer, restricting their freedom of motion. For instance, the decay time of the autocorrelation function was $\tau_{0\ \mathrm{min}} = 2.0 \pm 0.2$ s which is about 40 times more than what we reported for PA in bulk in the absence of cross-linkers $\tau_{0\ \mathrm{mM}} = (4.8 \pm 0.1) \times 10^{-2}$ s. Interestingly, when we repeated the measurement at a later time point although still within the lag time window, we found that the decay time of the intensity ACF had increased by a factor 4, $\tau_{90\ \mathrm{min}} = 8.8 \pm 0.1$ s. This finding, together with the kinetic curves in Fig. 4.3 (b), suggests that the formation of gelation nuclei at a nanoscale level, accompanied by a consequent slowdown of the dynamics, takes already place during the lag phase, however this can be detected only by a sensitive technique such as GI-XPCS. On the other hand, as the number of nanometric gelation points increases, they start interacting with each other until a certain critical threshold is reached, beyond which the macroscopic transition takes place, as proved by ISR. As shown in Fig. 4.5 (b), it is remarkable that as the reaction proceeds and the GI-XPCS measurement were repeated at later delay times, the decay time of the intensity ACFs kept increasing, suggesting a further slowdown of the dynamics at a nanoscale level confined at the liquid/liquid interface. For instance, $\tau_{300\ \mathrm{min}} = 20.2 \pm 0.9$ s and $\tau_{580\ \mathrm{min}} = 45.9 \pm 1.1$ s, therefore with an overall increase of the decay time in the saturation level regime by a factor 23 compared to the one measured at t = 0. This effect can be attributed to the increase in viscosity of the polymer. From the macroscopic ISR measurements we can indeed estimate the complex interfacial viscosity $\eta^* = \frac{\sqrt{(\Delta G')^2+(\Delta G'')^2}}{\omega}$, where ω is the angular frequency. In order to compare the two experimental techniques, the complex interfacial viscosity has been estimated from the rheological measurements performed with the same experimental conditions used for GI-SAXS, at least for what concerns the [PA] and the [$CaCl_2$ nanoparticles]. Considering $\eta^* = 386$ mPa·m·s and $\eta^* = 4239$ mPa·m·s at t = 0 and t = 600 min respectively, this gives rise to an increase of a factor ~11. This one is about 2 times less than the corresponding factor of ~23 that we measured with GI-XPCS, from $\tau_{0\ \mathrm{min}} = 2.0$ s to $\tau_{580\ \mathrm{min}} = 45.9$ s. Despite this discrepancy, these findings suggest a direct connection between the increase in the interfacial viscosity and the slowdown of the dynamics at the liquid/liquid interface.

Together with the increase of the decay time of the intensity ACFs, the progress of the gelation process is also attested by the evolution of the shape exponent as shown in Fig. 4.5 (c). For instance, it increased from $\beta_{0\ \mathrm{min}} = 0.78 \pm 0.09$ to $\beta_{580\ \mathrm{min}} = 1.20 \pm 0.03$, leading from a stretched profile of the ACF to a "compressed" one, similar to what we reported for the gelation of PA in bulk. Furthermore, in Fig. 4.5 (d) the relaxation rate, $\Gamma = \tau^{-1}$, is reported, which shows a linear dependence on $\boldsymbol{q}$ for the time points t = 90, 300, 580 min. Note that the same tendency Γ *vs* $\boldsymbol{q}$ was observed for t = 0 min as well, however it was not included in Fig 4.5 (d) to improve the clarity because of the different order of magnitude (See the Appendix A1). Interestingly, the slope of the lines fitting the Γ profiles strongly decreases as the reaction carries on, which is a clear indication of the formation of the gel structure and the consequent slowdown of the dynamics. This behavior is not surprising at all; as discussed in Chapter 2 the appearance of compressed correlation functions together with a linear, $\Gamma \sim \boldsymbol{q}$, dependence is often associated with a hyper-diffusive, ballistic-type motion, emerging from the abrupt release of the strain field produced by a random distribution of slowly-evolving sources of internal stress.[182, 183] As previously mentioned by Madsen,[65] this unusual behavior is often considered as the distinct sign of out-of-equilibrium dynamics in many complex systems, like concentrated colloidal suspensions,[182] polymeric and colloidal gels,[63, 202] two-dimensional gels,[64] nanoparticles probes in glass former matrix[71, 72] and structural glasses.[67] Interestingly, a linear dependence of the relaxation rate from on $\boldsymbol{q}$ is exhibited even at the onset of the gelation transition, where the intensity ACF still decays in a stretched exponential fashion and one would expect a diffusive dynamics, thus $\Gamma \sim q^2$, as in the case of Brownian motion, that was discussed in Chapter 2. This characteristic tendency has been reported also in colloidal suspensions of Laponite[69] and in a two-dimensional gel[203] and could be related to a discontinuous hopping-induced diffusion[204] at the crossover between the sol and gel phase.

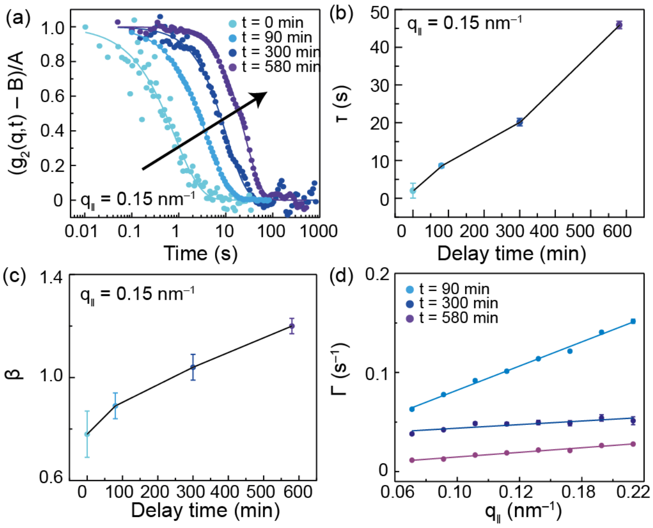

Fig. 4.5 Change in interfacial dynamics unraveled by GI-XPCS. (a) Normalized intensity autocorrelation functions (ACFs) measured at t = 0, 90, 300, and 580 min after the injection of $CaCl_2$ NP. at $q_{//} = 0.15$ nm^{-1}. Solid lines represent the fits obtained with Eq. (3.6). Temporal evolution of the (b) structural relaxation time τ and (c) form factor β. (d) Relaxation rate Γ plotted vs. $q_{//}$ at t = 90, 300

and 580 min, implying the suppression of interface dynamics by gelation. Solid lines represent linear regressions.

Thanks to the use of a two-dimensional detector, the underlying dynamics at the nanoscale level can be probed simultaneously at different scattering vectors. The $\boldsymbol{q_{//}}$ dependence (along the y-axis direction as shown in Fig. 4.4) of the intensity ACFs and their corresponding decay time τ is reported in Fig. 4.6 (a) and 4.6 (b) at the time point t = 580 min which corresponds to the achievement of the gelation saturation level. Remarkably, as $\boldsymbol{q}$ increases, the decay time, τ, of the corresponding ACF decreases. This observation can be understood in terms of the reciprocity between the scattering vector and the length scales: larger $\boldsymbol{q}$s are indeed associated to shorter length scales and *vice versa*.

In contrast to the strong dependence of τ on $\boldsymbol{q_{//}}$, the decay of the intensity ACF is independent from the perpendicular component of the exchanged momentum (along the z-axis as shown in Fig. 4.4). For instance, all normalized intensity ACFs overlap with each other and the extrapolated τ values were found to diverge of less than 10% of the standard error with respect to the mean value as shown in Fig. 5.6 (c) and 5.6 (d). These findings are a clear sign that the gelation dynamics is confined within the oil-water interfacial plane, therefore a surface phenomenon of two-dimensional nature.

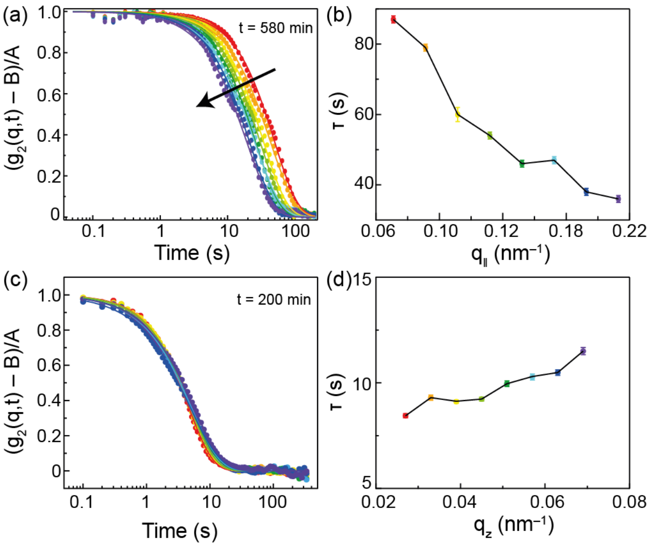

Fig. 4.6: Dependence of the relaxation time τ on $q_{//}$ and $q_{\perp}$. (a) Normalized intensity ACFs at t = 580 min. ACFs collected at various $\boldsymbol{q_{//}}$ are presented in a colored fashion. (b) Relaxation time τ plotted as a function of $\boldsymbol{q_{//}}$. (c) Normalized intensity ACFs at t = 200 min. ACFs collected at various $\boldsymbol{q_{\perp}}$ are presented in a colored fashion. (b) Relaxation time τ plotted as a function of $\boldsymbol{q_{\perp}}$.

4.2.4.The aging effect in hydro- and polymer gels.

As a general remark, when out-of-equilibrium systems, such as hydro- and polymer gels, are involved, one should always consider that the dynamics is largely affected by the time when the measurement is performed, as it was discussed in the examples given at the end of Chapter 2. Therefore, it is not surprising at all that the ACF spontaneously changes over time, simply because the underlying dynamic processes are not stationary.

Other studies on similar systems such as methylcellulose gels focused on this aspect, pointing out the presence of an underlying physical "aging effect". Interestingly, this aging can have a dramatic effect on the observed dynamics of the system, which was reflected in an increase of the decay time of the ACF up to one order of magnitude, when the same measurement was repeated one hour after temperature equilibration.[57] As presented in Fig. 4.7, a hint of a similar behavior was observed for PA in bulk, where the decay time of the ACF increased of a factor 2, when we repeated the measurement at a new position with a time shift of ca. 8 minutes. However, such a dramatic effect as reported for methylcellulose was not observed in case of polyalginate measured via GI-XPCS at the liquid/liquid interface. For instance, when we repeated the measurement at time t = 600 min, the decay time of the ACF and the $\boldsymbol{q}_{//}$ dependence were similar to what we found for t = 580 min, with the exception of the Kohlrausch exponent which increased from $\beta_{580\,\mathrm{min}} = 1.20 \pm 0.03$ to $\beta_{600\,\mathrm{min}} = 1.54 \pm 0.02$ (See Appendix A2). These findings might suggest that the time scales to be able to observe a clear sign of aging effect for our system are much longer, possibly due to the constraints imposed by the limited diffusion of the cross-linkers at the o/w interface, with a consequent slow nucleation and growth rate of the gelation sites. More investigations are required in order to be able to explain the complex underlying hyper-diffusive dynamics and the stress relaxation phenomena of the microdomains occurring in this non-trivial system.

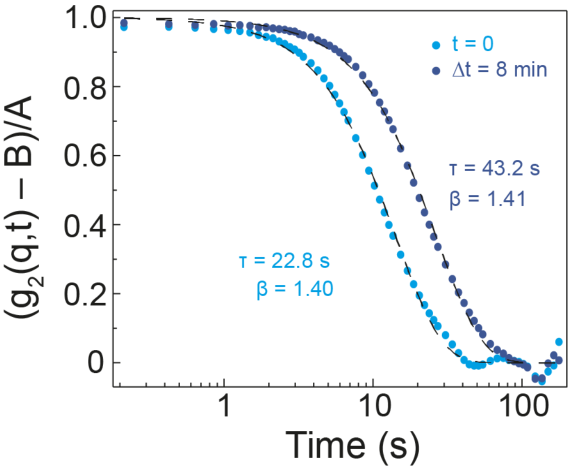

Fig. 4.7. Effect of aging in the gelation of polyalginate in bulk. Intensity ACFs measured at two different time points for the same strong gel, prepared with PA 1.7 wt% and 100 mM $CaCl_2$. of cross-linkers. The increase in decay time τ of a factor 2 between the initial (light blue), and final (dark blue) state suggests the presence of an underlying aging effect.

Chapter 5: Non-Classical Interactions of Phosphatidylcholine with Mucin Protect Intestinal Surfaces

The majority of the data presented in this chapter was published in a peer-reviewed journal:

On October 2018 on Langmuir, 34 (46), pp 14046–14057.

"Nonclassical Interactions of Phosphatidylcholine with Mucin Protect Intestinal Surfaces: A Microinterferometry Study"

Federico Amadei[1], Benjamin Fröhlich[1], Wolfgang Stremmel[2,3], and Motomu Tanaka[1,4]

[1] Physical Chemistry of Biosystems, Institute of Physical Chemistry, Heidelberg University, D69120 Heidelberg, Germany
[2] Medical Center Baden-Baden, D76530 Baden-Baden, Germany
[3] Internal Medicine IV, University Hospital Heidelberg, D69120 Heidelberg, Germany
[4] Center for Integrative Medicine and Physics, Institute for Advanced Study, Kyoto University, 606-8501 Kyoto, Japan

Author Contributions:

F.A. performed all aspects and data analysis of the experiments presented in this chapter. B.F. wrote the MATLAB script to analyze the RICM data. W.S. contributed intellectually to the discussion and interpretation of the results. M.T. participated in the conception and design of the experiments described here and was involved in manuscript writing.

5.1.Summary

Here, the question how PC interacts with its binding proteins, the mucins, which may establish the hydrophobic barrier against colonic microbiota, was addressed. The significance of interfacial interactions between phospholipids and mucin proteins was quantified by the combination of an *in vitro* intestinal surface model and label-free microinterferometry. The model of intestinal surfaces consists of planar lipid membranes deposited on solid substrates (supported membranes) that display mucin proteins at defined surface densities. Following the quantitative characterization of the systems, the vertical fluctuation of 10 µm-large particles on model intestinal surfaces by using microinterferometry were monitored, and the effective interfacial interaction potentials were calculated by analytically solving the Langevin equation. It was found that the spring constant of interfacial potentials calculated based on a harmonic approximation increased concomitantly with the increase in surface potentials, indicating the dominant role of electrostatic interactions. Intriguingly, the spring constants of particles coated with phospholipids do not follow electrostatic interactions. The spring constant of particles coated with zwitterionic phosphatidylcholine was larger compared to membranes incorporating positively or negatively charged lipids. These findings suggested the presence of another underlying molecular level interaction, such as phosphocholine-saccharide interactions. The fact that phosphatidylcholine sustains the binding capability to enzymatically degraded mucin suggests that the direct delivery of phosphatidylcholine to the damaged mucus is a promising strategy for the better treatment of patients affected by inflammatory bowel diseases.

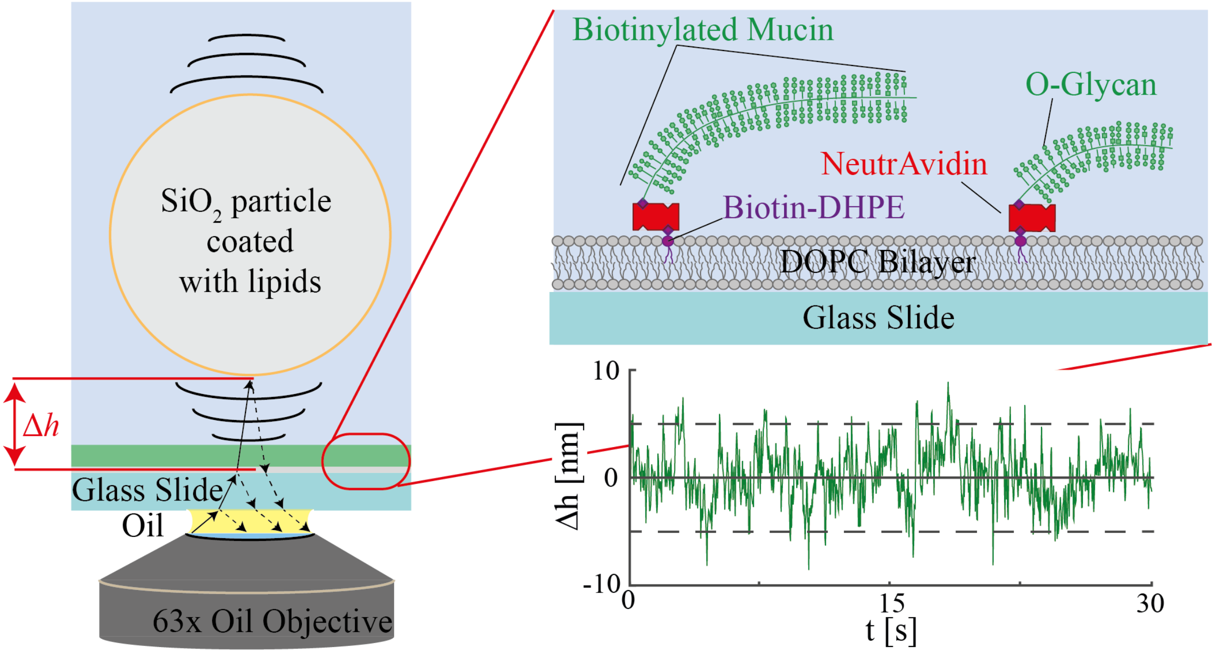

Scheme 5.1: Design of experimental systems to quantify the interfacial interaction potentials between lipids and mucin. Height fluctuation of SiO_2 particles (Ø ≈ 10 µm) coated with lipid

membranes on the mucin-displaying surface was monitored by microinterferometry. The analytical solution of Langevin equation yields the effective interfacial interaction potential.

5.2.Results and discussion

5.2.1.Fabrication of an *in vitro* intestinal model surfaces.

Fig. 5.1 represents the changes in resonant frequency Δf and dissipation ΔD from the fifth overtone monitored by QCM-D, following the subsequent incubation with (i) lipid vesicles (ii) NeutrAvidin and (iii) biotinylated mucin solutions. The first process, (i) formation of supported membranes by vesicle fusion could be fitted with the Sauerbrey equation:

$$\Delta m = -\frac{C\Delta f}{n} \text{ and } d = -\frac{C\Delta f}{\rho}. \qquad (5.1)$$

since the change in dissipation ($\Delta D \approx 0.5$ E^{-6}) was well below the threshold level 2×10^{-6}.[205] C is the mass-sensitivity constant (C = 18.06 ng Hz^{-1} cm^{-2}), n the overtone number, Δm (ng/cm^2) the adsorbed mass per unit area, Δf (Hz) the frequency shift, and ρ the density of DOPC membrane ρ_{DOPC} = 0.998 g/cm^3.[206, 207] The transient decrease in Δf $\approx$ 26 Hz coincides with the adsorption of vesicles, which is followed by the increase to a steady state. The difference between the initial state and the saturation level Δf $\approx$ 26 Hz shows an excellent agreement with those previously reported for supported lipid membranes. In fact, the thickness of the film obtained from the analysis (4.7 nm) shows good agreement with those reported for supported lipid membranes measured by high energy specular X-ray reflectivity, 3.9 - 5.4 nm.[139]

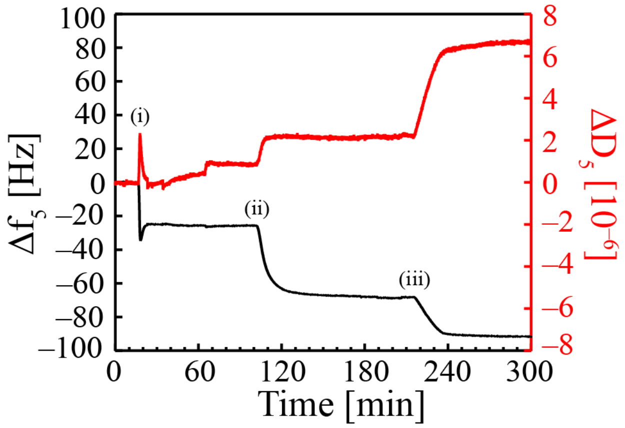

Fig. 5.1: Step-wise fabrication of an *in vitro* intestine model surface monitored by QCM-D. (i) deposition of supported membranes, (ii) coupling of NeutrAvidin cross-linkers, and (iii) binding of biotinylated mucin could be detected quantitatively by decreases in the resonant frequencies (black) and increases in the dissipations (red).

The deposition of (ii) NeutrAvidin and (iii) mucin were fitted with Voigt model:

$$\Delta f \approx -\frac{1}{2\pi\rho_0 h_0}\left\{\frac{\eta_3}{\delta_3} + h_1\rho_1\omega - 2h_1\left(\frac{\eta_3}{\delta_3}\right)^2 \frac{\eta_1\omega^2}{\mu_1^2 + \omega^2\eta_1^2}\right\}. \tag{5.2}$$

and

$$\Delta D \approx \frac{1}{\pi f \rho_0 h_0}\left\{\frac{\eta_3}{\delta_3} + 2h_1\left(\frac{\eta_3}{\delta_3}\right)^2 \frac{\eta_1\omega}{\mu_1^2 + \omega^2\eta_1^2}\right\}. \tag{5.3}$$

ρ_0 and h_0 are the density and thickness of the crystal, η_3 the viscosity of the bulk liquid, δ_3 the viscous penetration depth of the shear wave in the bulk liquid, ω the angular frequency of the oscillation. ρ_1, δ_1, η_1 and μ_1 are the density, the thickness, the viscosity and the shear elasticity of the adsorbed layer, respectively. The values obtained from the fitting are summarized in Table 5.1.

	Thickness (nm)	Viscosity (10^{-3}) (Pa·s)	Shear modulus (10^3) (Pa)
NeutrAvidin	5.8 ± 1.4	0.9 ± 0.4	1050 ± 29
Mucin	29.3 ± 1.3	1.8 ± 0.1	25 ± 7

Table 5.1: Summary of QCM-D data results presented in Fig. 5.1 using a De Voigt model to fit the experimental data.

The value for the thickness of the NeutrAvidin layer (5.8 ± 1.4 nm) is in excellent agreement with the crystallography structural data from dry protein crystals (5.3 nm),[208] and the values obtained by specular X-ray reflectivity (4.8 nm) and grazing incidence X-ray scattering (5.2 nm) measured at the air/water interface.[209] As suggested from a large increase in dissipation compared to NeutrAvidin, $\Delta D \approx 6 \times 10^{-6}$, the analysis reveals that the mucin forms a layer with a high viscosity, $\eta = (1.8 \pm 0.1) \times 10^{-3}$ Pas, and shear modulus, $\mu = (25 \pm 7) \times 10^3$ Pa. This seems to be in good agreement with previous QCM-D studies on mucin proteins that can be found in airway and gastrointestinal mucosal surfaces (MUC5B) physisorbed onto bare gold surfaces, that report values of $\eta = 1.3 \times 10^{-3}$ Pas, and shear modulus, $\mu = 9.8 \times 10^3$ Pa.[210] The thickness obtained by the Voigt model (29.3 ± 1.3 nm) seems much higher than the values reported for mucin physisorbed on Au surfaces (7 – 10 nm)[195, 211] which can be attributed to the fact that our membrane surfaces display significantly attractive anchoring points compared to Au. Note that the dissociation constant of biotin-NeutrAvidin interaction is ~ 10^{-15} M,[212] and the average distance between biotin moieties used in this study is 5 − 6 nm,[213] which is much smaller than the hydrodynamic radius of the same mucin we previously measured, $\Phi_{\mathrm{mucin}} = 46 \pm 11$ nm.[13] Although all the biotin-NeutrAvidin sites would not be occupied, it is plausible that the grafting density is much larger compared to the physisorbed mucin on Au. The stable grafting of mucin onto supported membranes was further verified by incubating dye-conjugated wheat germ agglutinin at 37 °C. Compared to the control signal detected on pure DOPC lipid membranes, we observed a clear signal that confirms the homogeneous deposition of mucin layers, as shown in Fig. 5.2.

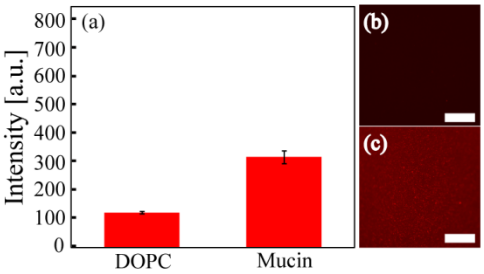

Fig. 5.2: Staining with fluorescently labeled lectin confirms the anchoring of mucin on supported membranes. Fluorescence images (b) pure DOPC membrane and (c) membrane coated with mucin after 30 min incubation at 37 °C with wheat germ agglutinin coupled to TexasRed. (a) The integrated fluorescence intensities confirm the binding of mucin. The scale bar represents 10 µm.

5.2.2.Interaction of latex microparticles with mucin follows electrostatics

The first question which was addressed aimed to determine the role of electrostatics in interfacial interactions. Here, the interactions of latex microparticles carrying different surface charges with mucin layers were first investigated. The COO^{-} latex particles show clearly negative potential $\zeta_{COO^{-}} = -79 \pm 3$ mV. The untreated latex particles possess a slightly positive zeta potential $\zeta_{untreated} = +15 \pm 1$ mV. Once the COO^{-} latex particles are coated with positively charged chitosan, the potential shifts to a positive value, $\zeta_{chitosan^{+}} = +39 \pm 9$ mV. Fig. 5.3 (a) shows the height fluctuation of latex particles on supported membranes displaying mucin, recorded over 30 s. COO^{-} latex particles exhibit the most pronounced height fluctuation with an amplitude larger than 10 nm (red). According to the increase in ζ potential from untreated (blue) to chitosan-coated ones (green), the height fluctuation amplitude decreases. As presented in Fig. 5.3 (b), the interaction potential $V(\Delta h)$ near the minimum can be well fitted as a parabola, validating the imposed harmonic approximation according to Derjaguin[75]. Namely, the second derivative of the harmonic potential, V'', is the spring constant of a harmonic oscillator, representing how sharply the particle position is confined. As shown in the Fig., the increase in ζ potential of the latex particle surfaces leads to a monotonic increase in potential curvature. Since mucin is negatively charged due to the sialic acid residues, the observed tendency implies that the increase in electrostatic attractions caused the sharpening of the potential confinement of latex particles; $V''_{COO^{-}} = 1.1 \pm 0.5$, $V''_{untreated} = 4.7 \pm 0.3$ and $V''_{chitosan^{+}} = 31 \pm 6$ $[10^{-22}$ J/nm$^{2}]$. It should be noted that the deposition of chitosan (+) on COO^{-} latex particles might change not only the net charge but also the viscoelasticity of the particle surface, which may cause an underestimation of the potential confinement. However, a recent study using quartz crystal microbalance with dissipation indicated that the thickness of chitosan layer deposited on the oppositely charged surface is merely 3 – 5 nm [214]. In fact, the chitosan-coated particles exhibit the sharper potential confinement than untreated particles which also carry positive net charges. Fig. 5.3 (c) represents the autocorrelation functions of height fluctuation for differently charged latex particles, yielding the characteristic relaxation time τ_c from the fitting with single exponential decay functions (Eq. 5). The relaxation time of particles coated with positively charged chitosan τ_{chitosan^+} $\approx$ 0.02 s is approx. 5 times shorter than the corresponding values of negatively charged COO^- latex particles $\tau_{COO^-} \approx 0.10$ s, indicating the increase in electrostatic interactions also causes an increase in hydrodynamic friction γ. Table 5.2 shows the summary of MSA, V'', τ_c, and γ calculated from more than 20 particles for each data set. The obtained results denoted that the interaction between latex particles and mucin-coated surfaces is dominated by electrostatic interactions. To modulate net charges on probe particles, latex particles were used instead of silica particles that can be functionalized with various silane derivatives. First, the use of solid silica particles with a density of 2.6 g/cm^3 was not practically possible, since the height fluctuation is damped by the gravitational force. Second, the porous silica particles with a lower density cannot be used, as the surface charges are not uniformly distributed on the surface displaying pores with the size of tens to hundreds of nm.

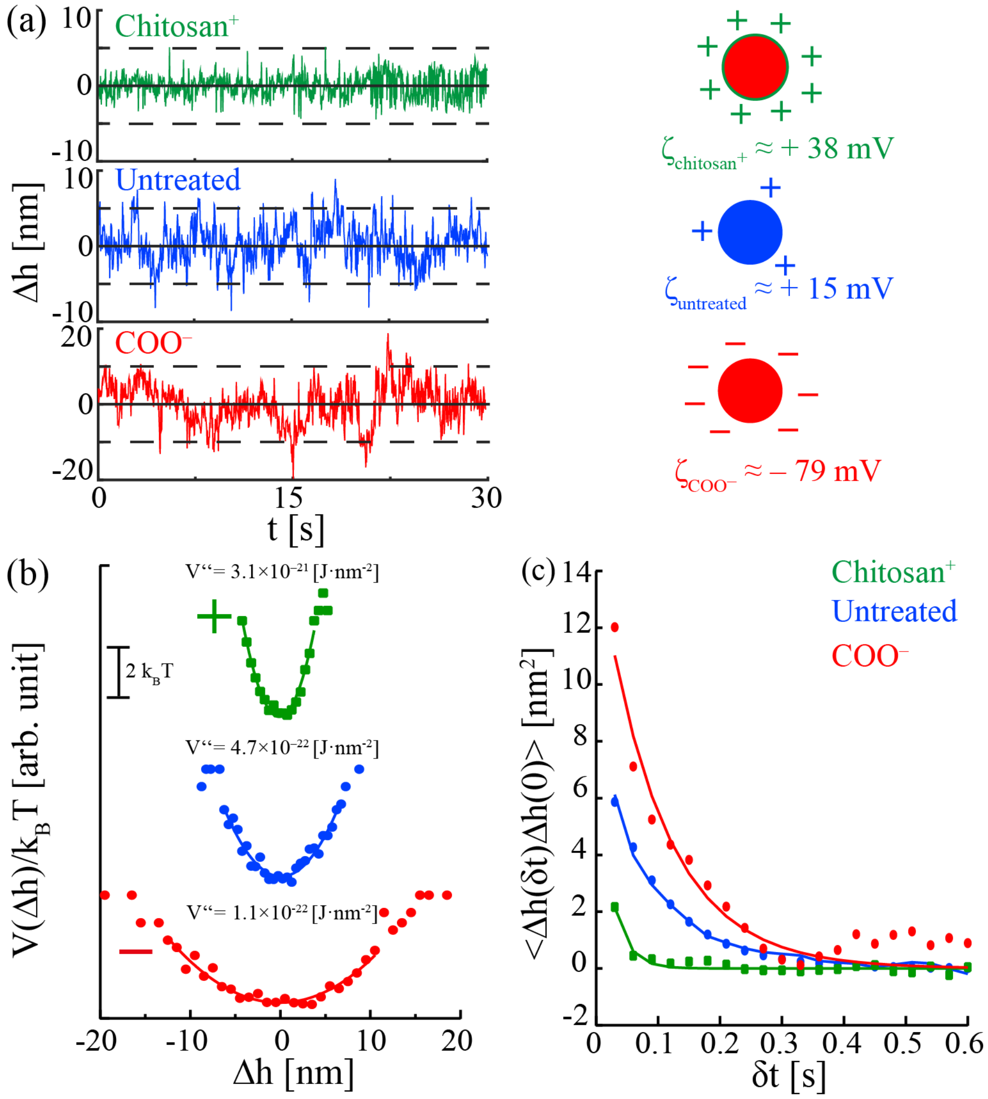

Fig. 5.3: RICM of latex particles to assess the role of electrostatics. (a) Height fluctuation Δ*h*(t) of latex particles on model intestine surfaces recorded over 30 s: red; carboxylated latex particles (–), blue; untreated latex particles, and green; carboxylated latex particles with additional chitosan layers (+). (b) Calculated interaction potentials and the parabolic fits according to the harmonic potential approximation. The spring constant (potential curvature) increases with the electrostatic interactions. (c) Autocorrelation functions of height fluctuation. Solid line represents single exponentials fits.

Latex particle	MSA [nm^2]	V'' [10^{-22} J/nm^2]	τ_c [s]	γ [10^{-22} J·s/nm^2]
COO$^-$	841 ± 58	1.1 ± 0.5	0.10 ± 0.08	0.11 ± 0.09
Untreated latex	50 ± 4	4.7 ± 0.3	0.09 ± 0.04	0.42 ± 0.19
COO$^-$ coated with chitosan	5.3 ± 0.5	31 ± 6	0.02 ± 0.01	0.62 ± 0.32

Table 5.2. Summary of latex particles. The results for the Mean Square Amplitude (MSA), the spring constant (V''), the decay of the autocorrelation function (τ_c) and friction coefficient (γ) for at least 20 particles per condition are presented.

5.2.3.Interaction of lipid-coated microparticles with mucin cannot be explained by electrostatics.

In the next step, the interfacial interactions between mucin-displaying substrates and SiO_2 particles coated with lipid membranes was investigated (Fig. 5.4 (a)). As presented in Fig. 5.4 (b), membranes based on negatively charged DOPG (−), zwitterionic DOPC (±) and positively charged DOTAP (+) were prepared. Fig. 5.4 (c) represents the phase contrast (upper panels) and fluorescence (lower panels) images of (c1) DOPG:DOPC, (c2) DOPC, and (c3) DOTAP membranes. Note that DOPG alone cannot form a stable membrane and hence was mixed with DOPC at a molar ratio of 1:1. The images captured at the same positions confirm that the surfaces of all silica particles are homogenously coated with lipid membranes. To further prove the coating and assess the modified surface charge distribution, ζ potential of the coated silica particles was measured: $\zeta_{\mathrm{DOPG:DOPC}} = -29 \pm 1.5$ mV, $\zeta_{\mathrm{DOPC}} = -8.7 \pm 0.1$ mV, and $\zeta_{\mathrm{DOTAP}} = +27.6 \pm 4.4$ mV. A slightly negative value found for DOPC-coated particles can be attributed to the partial deprotonation of the choline group at pH 7.4.[215]

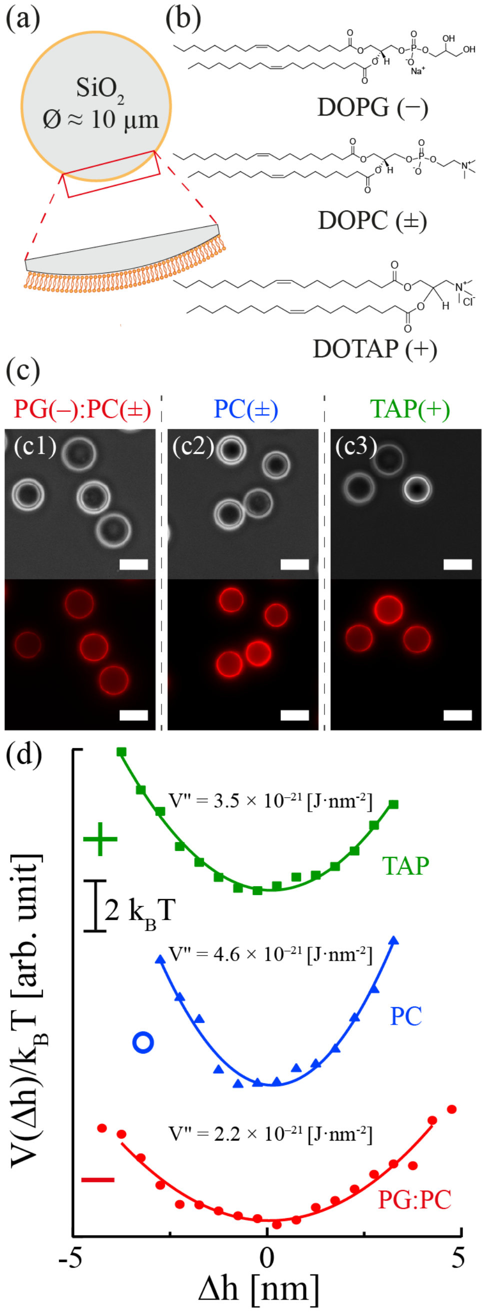

Fig. 5.4: RICM of lipid-coated SiO_2 particles. (a) Schematic illustration of lipid membrane supported on SiO_2 particle (Ø ≈ 10 µm). (b) Chemical structures of lipids used in this study. (c) Phase contrast (top) and fluorescence (bottom) images of silica particles coated with lipids with different net charges; PG (–), PC (±), and TAP (+). The scale bars: 10 µm. (d) Calculated interaction potentials between model intestine surfaces and silica particles coated with lipids. The sharpest particle confinement was found for PC-coated particles.

Fig. 5.4 (d) shows the calculated interfacial potential $V(\Delta h)$ from the height fluctuation for PG:PC (– red), PC (± blue), and TAP (+ green), fitted with parabolic functions. As obviously seen from the Fig.s, the potential curvature does not increase monotonically with the increase in ζ potential; $V''_{\text{DOPG:DOPC}(-)}$ =

2.2 ± 0.4, $V''_{\mathrm{DOPC}(\pm)} = 4.6 \pm 0.4$, and $V''_{\mathrm{DOTAP}(+)} = 3.5 \pm 0.4$ [10^{-21} J/nm^2]. It should be noted that the characteristic relaxation time of the height-height autocorrelation function is close to the detection limit ($\tau < 0.01$ s), suggesting that the hydrodynamic friction coefficient is $\gamma < 0.1$ J·s/nm^2, as shown in Fig. 5.5.

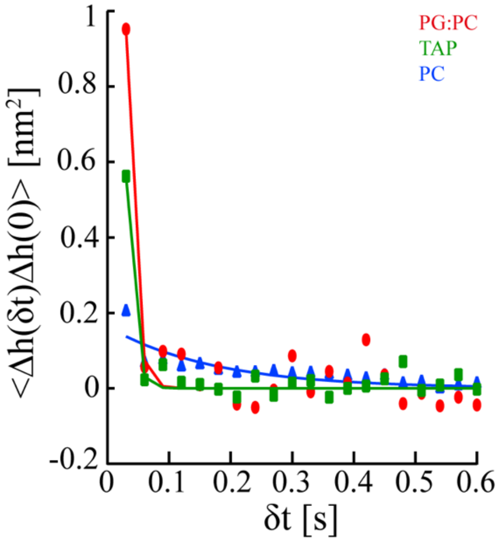

Fig. 5.5: Autocorrelation functions of height fluctuations for silica particles coated with lipid membranes on supported membranes decorated with mucin. Solid line represents single exponentials fits. It should be noted that the characteristic relaxation time of the height-height autocorrelation function is close to the detection limit ($\tau < 0.01$ s), suggesting that the hydrodynamic friction coefficient is $\gamma < 0.1$ J·s/nm^2.

The strongest potential confinement was observed for particles coated with zwitterionic DOPC membranes. This follows the line of our previous account, where we reported (a) the lipid vesicles by mucin was most pronounced for DOPC using DLS and (b) the enthalpy of interaction with DOPC was the largest compared to the other two membranes using ITC.[13] In general, the experiments at different ionic strengths would be one of the straightforward strategies to highlight the role of electrostatics, although the main focus of this study is to quantify the phospholipid-mucin interactions under physiological conditions. However, it should be noted that the electrostatics of highly charged polymer chains cannot be handled by the classical Poisson-Boltzmann theorem, as the charge distribution is never static or uniform.[216, 217] Furthermore, at low ionic strength, it has been reported that the ionic strength inside the polymer layer is significantly different from that of bulk.[218] Since mucin used in this study is not fully defined in terms of degrees of glycosylation and ionization, we focused on the experiments at the physiological ionic strength.

5.2.4. Wash-off assay confirms DOPC-mucin interactions can sustain the phospholipid barriers in intestine.

In order to understand if the phosphocholine-mucin interaction is indeed strong enough to sustain the phospholipid barrier on the intestinal mucus wash-off assays of lipid-coated particles were performed, as schematically depicted in Fig. 5.6 (a). Fig. 5.6 (b) represents the percentages of lipid-coated silica particles remaining adherent on mucin surfaces plotted as a function of shear stress. 50 % of particles coated with DOPG:DOPC (red, −) were washed off already at the shear stress of $\tau_{50\ \mathrm{DOPG:DOPC(-)}} = 0.20$ Pa. On the other hand, the corresponding value for particles coated with positively charged DOTAP (green, +) and at $\tau_{50\ \mathrm{DOTAP(+)}} = 0.34$ Pa, suggesting that positively charged lipid membranes can resist the higher shear stress than negatively charged membranes. Remarkably, more than 80 % of DOPC-coated particles remained adherent at $\tau = 0.34$ Pa. The $\tau_{50\ \mathrm{DOPC(\pm)}}$ estimated from the linear extrapolation is ≥ 0.75 Pa. Considering the typical physiological range of shear stresses in intestines, 0.1 − 0.5 Pa,[39] the obtained results suggest that the interaction of zwitterionic PC with mucin is stronger than electrostatic interactions and thus can sustain the phospholipid barrier on intestinal mucus under shear stresses.

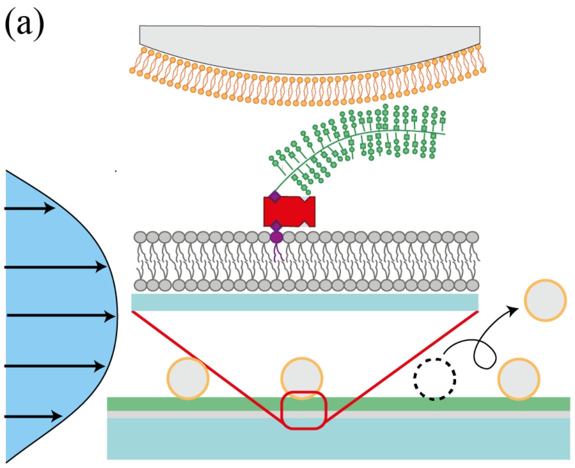

Detachment of membrane-coated particles from pre-occupied surfaces

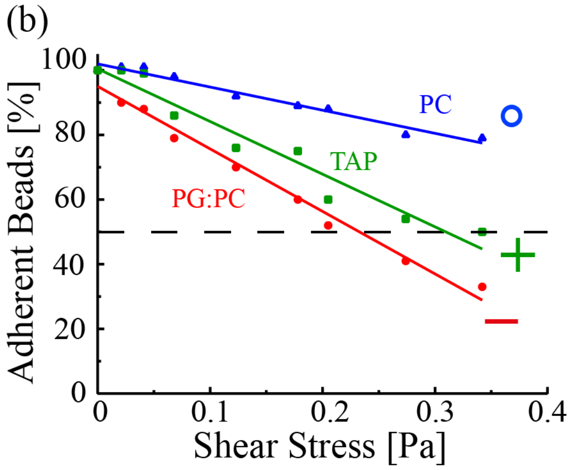

Fig. 5.6: Wash-off assay prove a higher persistence of DOPC-coated SiO_2 particles. (a) Schematic representation of wash-off assay. SiO_2 particles coated with lipid membranes were firstly allowed to adhere on the cell monolayer (30 min), the shear stress was increased step-by-step. (b) Percentages on

particles remaining on the surface plotted as a function of shear stress τ. About 50 % of particles coated with PG:PC (–) and TAP (+) were washed off already at the shear stress of $\tau = 0.20$ Pa, while more than 80 % of PC-coated particles remained adherent at $\tau = 0.34$ Pa. Solid lines represent linear fits.

5.2.5.Possible scenarios explaining PC-mucin interactions.

The obtained results clearly indicate that the pronounced interaction of PC and mucin cannot be explained only by the electrostatic interactions but by something stronger. Since mucin itself is a globular protein with no distinct structural order, the specific lock-key type interaction is not likely to take place. The hypothesis is currently advanced that the zwitterionic PC headgroups might interact with the saccharide side chains of mucin and this interaction might be stronger than the electrostatic interaction. In this case, the significant PC-mucin interaction observed here seems plausible because mucin is a heavily glycosylated protein possessing many lectin binding sites, as shown in Fig. 2. It is known that the change in glycosylation alters the surface hydration of proteins[219, 220] and organic materials,[221, 222] which plays critical roles in avoiding non-specific protein adsorption. Intriguingly, in our previous ITC experiments, we found that the mucin with a less degree of glycosylation showed a much weaker interaction with DOPC. The interaction enthalpy of mucin with a higher glycosylation degree was by a factor of 4 larger compared to the corresponding value of mucin with a lower degree of glycosylation.[13]

To date, several studies suggested the interaction of phosphatidylcholine headgroups and saccharides. For example, Curatolo et al. reported the fusion of small vesicles made out of glycolipids (lactosylceramide) was accelerated by doping them with phosphatidylcholine (egg yolk PC), suggesting the PC-saccharide interaction induces the fusion of vesicles.[223] Kreuzer et al. observed that the swelling of hyaluronic acid was limited in the presence of PC membranes.[111] It should be noted that these studies suggested that the PC-saccharide interactions might be stronger than generic and hence non-specific interactions, such as electrostatic interactions. In this paper, they proposed two possible scenarios. The first scenario assumes that hyaluronic acid chains can connect the outermost leaflet of two neighboring membranes separated by the layer of hydrating water. The second scenario suggests that a long polysaccharide chain deforms and anchors two or more headgroups within the same membrane. However, they did not systematically investigate if PC-saccharide interaction is influenced by the chemical structures of the headgroups and/or saccharides. It should be noted that it is experimentally very difficult to quantitatively determine the significance of such non-covalent interactions on the molecular level using vibrational spectroscopy or NMR.[224] Further studies by systematic alternation of lipid compositions and saccharide chains with our label-free RICM could offer a unique advantage to quantitatively determine the change in the phospholipid-mucin interactions from the interfacial potential calculation.

5.2.6.Enzymatic degradation of mucin layer *in vitro*.

The depletion of phospholipids from the intestinal mucus has been found in inflammatory bowel diseases, such as ulcerative colitis.[15] The loss of protective lipid barrier allows the attack of pathogenic microorganisms, which results in the irreversible damage to intestinal mucus.[225] In fact, the uptake of a diet enriched with fats showed a protective function against severe intestinal inflammations.[10] To verify how delivered phospholipids interact with the damaged mucin, mucin was enzymatically digested and the interfacial interaction potentials between damaged mucin and phospholipid membranes were measured. Since a previous study suggested that the efficiency of enzymatic digestion of mucin increases by the cleavage of sialic acid by the acid treatment,[83] mucin was firstly treated with neuraminidase that selectively cleaves sialic acids.[84] Fig. 5.7 shows the degradation of the mucin supported membrane followed by QCM-D. The time interval in which the treatment with each enzyme was carried out is highlighted by colored regions, neuraminidase in light blue and protease in dark blue respectively. The change in frequency and dissipation due to the action of the neuraminidase over 3 h was not very pronounced, which makes it practically impossible to quantify the amount of digested sialic acids from the QCM-D data. The small change caused by neuraminidase can be understood by the fact that the content of sialic acid in our mucin sample is 0.5 – 1.5 wt%. On the other hand, the injection of protease into the chamber at $t = 3$ h led to a more pronounced change in frequency and dissipation. At $t = 12$ h, the frequency shift reached the level ($\Delta f \approx -72.9$ Hz) close to that before the coupling of mucin ($\Delta f \approx -68.3$ Hz), suggesting the significant digestion of mucin by protease. However, it should be noted that the dissipation level after the enzymatic treatment, $\Delta D_{1260\text{min}}$, is significantly higher compared to the NeutrAvidin level, $\Delta D_{1260\text{min}} - \Delta D_{\text{NeutrAvidin}} \approx 3.2 \times 10^{-6}$. The significant difference in the dissipation clearly implies the presence of a viscoelastic layer.

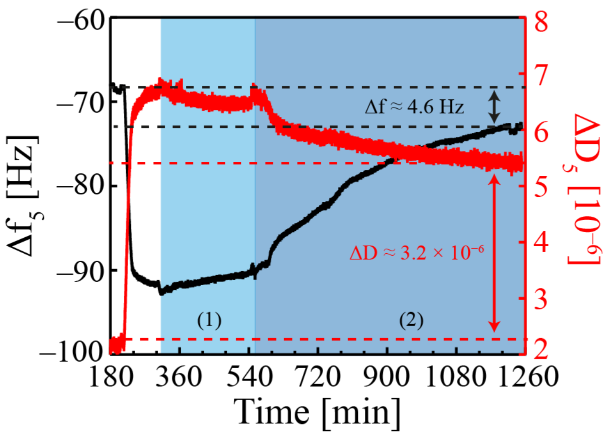

Fig. 5.7: Enzymatic degradation of mucin proteins. Mucin was first treated with (1) neuraminidase (light blue) and (2) protease (dark blue). The treatment with protease resulted in more distinct changes in both resonant frequency and dissipation. After 12 h of incubation the shift reached the level close to the one before the coupling of mucin, highlighted by broken lines.

The change in film properties after each treatment was analyzed by applying the De Voigt model (Eqs. 5.2 and 5.3), and the results are summarized in Table 5.3. Compared to the membrane displaying mucin (t = 300 min), the incubation with neuraminidase for 3 h (t = 480 min) led to an increase of the shear elasticity from $\mu_{300\text{min}} \approx$ 18 kPa to $\mu_{480\text{min}} \approx$ 360 kPa, while the layer thickness decreased from 30 nm to 19 nm. This can be interpreted as the release of water molecules bound to O-glycan chains that were digested by neuraminidase. The addition of protease further led to a decrease in layer thickness and an increase in shear modulus, suggesting the digestion of protein cores. The film thickness seemed to level off to ≈ 16 nm at t = 960 min, while the shear modulus still exhibited a slight drift even at t = 1200 min. The obtained results suggest that neither the complete digestion of mucin nor neutravidin is likely to take place. Note that the shear elasticity of membrane with NeutrAvidin, $\mu_{\text{NeutrAvidin}} \approx$ 1050 kPa, is by a factor of more than 2 compared to the value at t = 1200 min. Actually, the possibility of complete digestion of NeutrAvidin is not plausible, since the data after the enzymatic digestions can only be fitted with De Voigt model (Eqs. 5.2 and 5.3). On the other hand, the QCM-D data of supported membranes are fitted well with Sauerbrey equation (Eq. 5.1), but not with De Voigt model. Therefore, the obtained results suggest the partial digestion of mucin by the protocol used in this study, which does not jeopardize the integrity of underlying NeutrAvidin.

	t [min]	Thickness [nm]	η (× 10^{-3}) [Pa·s]	μ (× 10^{3}) [Pa]
Neutravidin	0	5.8 ± 1.4	0.9 ± 0.4	1050 ± 29
Mucin	300	30.0 ± 1.6	1.8 ± 0.1	18 ± 7
Neuraminidase	480	18.9 ± 0.6	2.9 ± 0.1	360 ± 38
Protease (i)	720	16.4 ± 0.8	2.7 ± 0.1	534 ± 29
Protease (ii)	960	15.9 ± 0.7	2.8 ± 0.1	512 ± 34
Protease (iii)	1200	15.8 ± 0.8	2.8 ± 0.2	435 ± 60

Table 5.3: Analysis of QCM-D data for mucin supported membranes digested enzymatically. The results refer to the data presented in Fig. 5.7 that were analyzed with De Voigt model (Eqs. 5.2 and 5.3).

To further verify the enzymatic digestion of mucin, biotinylated mucin was immobilized to the lipid membranes deposited on SiO_2 particles via NeutrAvidin cross-linkers, as schematically depicted in Fig. 5.8 (a), and the change in protein compositions was monitored using SDS-PAGE. Prior to the SDS-PAGE analysis, the particle-supported membranes harnessing biotinylated mucin were incubated with WGA-Texas Red. Fig. 5.8 (b1) represents the phase contrast image (upper panel) and the fluorescence image (lower panel) of the mucin-displaying membranes. As shown in the Fig., clear fluorescence signals were detected from the particle surface. On the other hand, the control samples (bare SiO_2 particles) showed no fluorescence signals (Fig. 5.8 (b2)). Fig. 5.8 (c) represents the protein patterns obtained by SDS-PAGE analysis. The protein bands were detected using the silver staining method. The lanes 2 – 5 coincide with the membrane-bound proteins, while the lanes 6 – 9 with the proteins in solutions (supernatants). As indicated by a blue box, the bands that appeared in the molecular weights beyond 50 kDa can be assigned to those of mucin, which possesses a broad distribution of the molecular weights (information from the manufacturer). The incubation with neuraminidase (lane 3) led to a smearing of protein bands in this region, suggesting the digestion of O-glycan. On the other hand, the incubation with protease alone (lane 4) and mixture of neuraminidase and protease (lane 5) resulted in almost a complete disappearance of the mucin bands. The bands corresponding to the digested protein fragments were not detectable probably due to low protein concentrations and broad distributions of molecular weights in supernatants. Intriguingly, however, the bands near 30 kDa could be detected, corresponding to the molecular weight of protease. Thus, the SDS-PAGE data denoted that not only O-glycans but also protein cores were digested enzymatically.

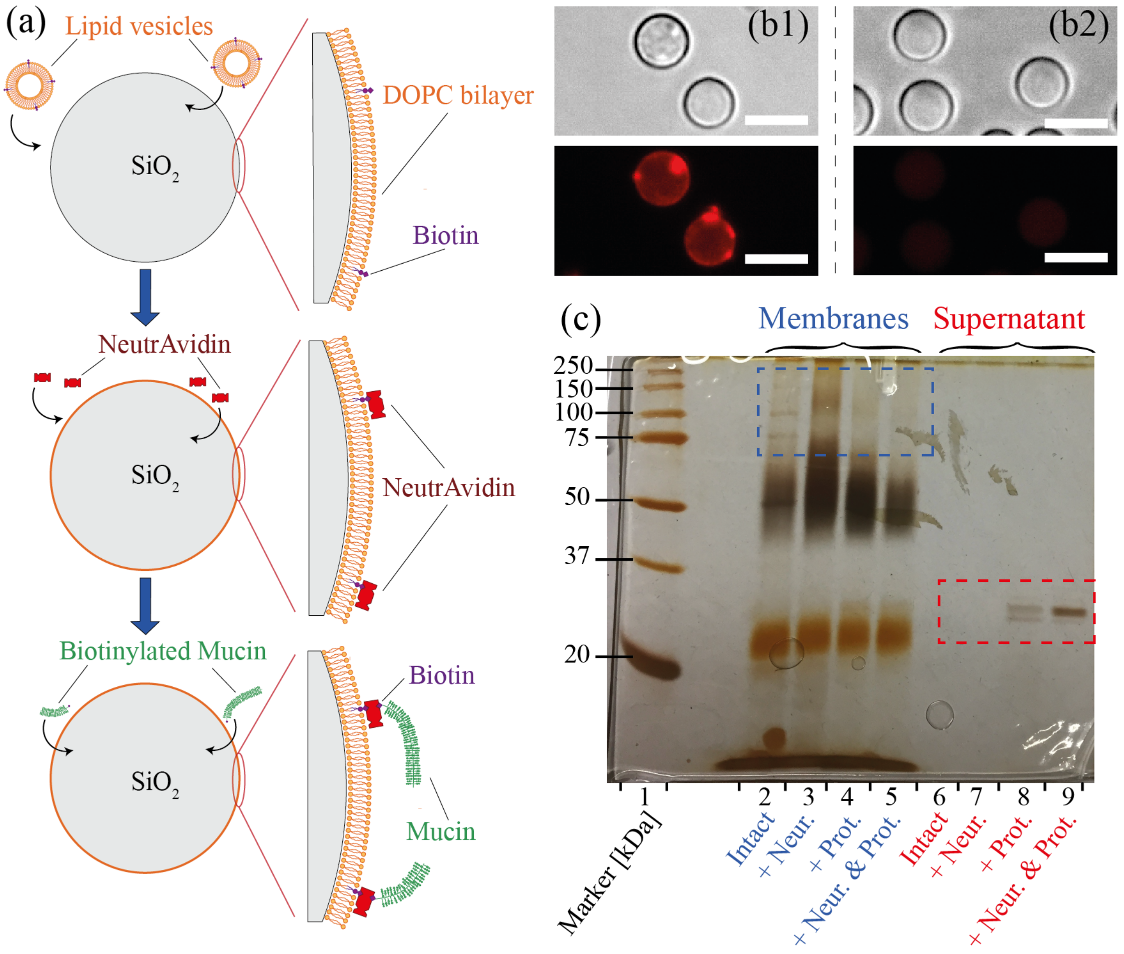

Fig. 5.8: SDS-PAGE of SiO$_2$ particles decorated with mucin supported membranes. (a) Preparation of particle-supported membranes displaying biotinylated mucin. (b) Successful immobilization of mucin was confirmed by the positive signals from WGA-TexasRed (b1), while the bare SiO2 particles (control) showed no signals (b2). (c) SDS-PAGE analysis of protein patterns. Lanes 2 – 5 correspond to the membrane-bound proteins, while lanes 6 – 9 to the proteins in solutions (supernatants). Lanes 2 and 6;

intact samples, lanes 3 and 7; samples treated with neuraminidase, lanes 4 and 8; samples treated with protease, and lanes 5 and 9; samples treated with neuraminidase and protease. The bands corresponding to mucin and protease are indicated by blue and red boxes, respectively.

Fig. 5.9 represents the interaction potentials calculated from the height fluctuations of particle-supported membranes on the surface displaying degraded mucin after 6 h of incubation with the enzymes. Here, instead of injecting enzymes one-by-one, neuraminidase and protease were applied together to model the intestinal environments. First, the confinement of particles coated with DOTAP (+, green) was found to become distinctly shallower after the enzymatic digestion of mucin ($V''_{\mathrm{DOTAP}} = 2.2 \pm 0.2$ [$\times 10^{-21}$ J/nm^2]), which could be explained by the decrease in electrostatic attraction with TAP(+) due to the digestion of negatively charged sialic acid residues by neuraminidase. Moreover, a clear increase in the potential curvature observed for DOPG:DOPC membranes (red, −) after mucin digestion ($V''_{\mathrm{DOPG:DOPC}} = 3.2 \pm 0.2$ [$\times 10^{-21}$ J/nm^2]) could also be attributed to the decrease in the electrostatic repulsions between PG(−) and sialic acid residues.

The fact that the potential confinement of particles coated with DOPG:DOPC membranes than that of DOTAP-coated particles could be explained by a high amount of PC(±) head groups that are attractive to the digested mucin. As the DOPG:DOPC membranes contain 50 mol% of DOPC, the density of PC head groups on the surface of a particle can roughly be estimated as 8.3×10^{17} PC/m^2 from the area per lipid molecule, 0.6 nm^2 [226]. Note that this coincides with the situation where 7×10^{11} PC head groups are exposed on one particle.

However, the most remarkable finding is that the enzymatic digestion of mucin resulted in a distinct increase in the potential curvature of DOPC (±, blue) membranes, $V''_{\mathrm{DOPC}} = 5.3 \pm 0.5$ [$\times 10^{-21}$ J/nm^2]. This finding suggests the following two scenarios. The first possible scenario is that PC might not interact with sialic acid residues but with neutral saccharides, which remained after the digestion by neuraminidase. The other scenario is that the enzymatic digestion of mucin reduced the entropic repulsive forces by the cleavage of saccharide chains and proteins.[227] Further investigation of interactions of other polysaccharides and phospholipid membranes would help us unravel the underlying molecular mechanism of PC-mucin interactions.

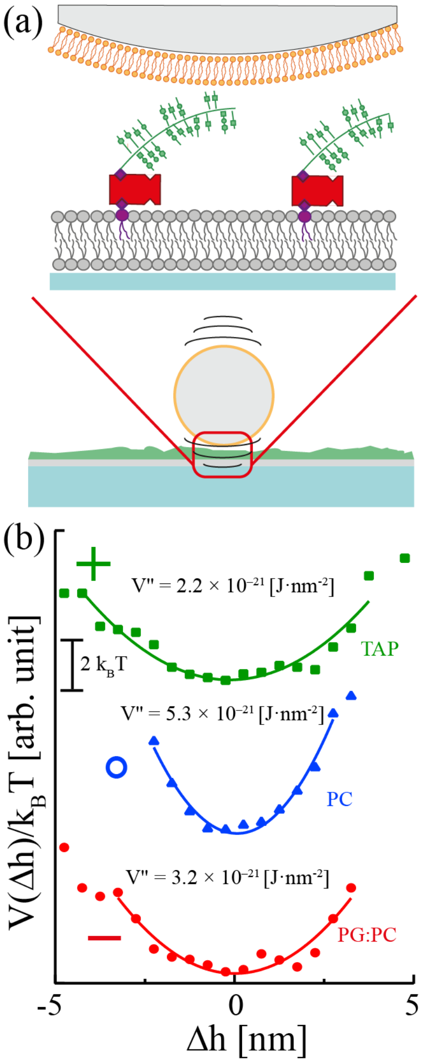

Fig: 5.9: RICM of lipid-coated SiO_2 particles on degraded mucin supported membranes. (a) Schematic representation of SiO_2 particles coated with lipids hovering on mucin supported layers after enzymatic degradation and (b) their calculated interaction potential. Compared to the spring constants on intact mucin (Fig. 5.4), the potential confinement becomes sharper for particles coated with zwitterionic PC and shallower for DOTAP.

Last but not least, the results obtained here have a clear clinical relevance towards the improved therapeutic treatment of inflammatory bowel disease patients. These findings demonstrated that the PC-mucin interaction was not retarded but even more enhanced after enzymatic digestion. This indicates that the phospholipid depletion in inflammatory bowel diseases is not caused by the loss of PC-mucin binding capability. This suggests that the phospholipid depletion is caused by the loss of functions to synthesize and transport phospholipids from the goblet cells through tight junctions.[12] An alternative scenario is the elevation of phospholipid digestion by phospholipase A_2, as reported for the case of Crohn disease.[228] Therefore, the delivery of phospholipase inhibitor[19] and zwitterionic phosphatidylcholine to the damaged mucus layer seems to be a promising strategy to assist the recovery of phospholipid barrier functions against the attack by pathogenic microorganisms.[229]

Chapter 6: Shear-Enhanced Dynamic Adhesion of *Lactobacillus rhamnosus* GG (LGG) on Polarized Intestinal Epithelial Cell Monolayers: Correlative Effect of Protein Expression and Interface Mechanics

The majority of the data presented in this chapter was published in a peer-reviewed journal:

On December 2018 on Langmuir, 35 (2), pp 529 – 537.

"Shear-Enhanced Dynamic Adhesion of *Lactobacillus rhamnosus* GG (LGG) on Polarized Intestinal Epithelial Cell Monolayers: Correlative Effect of Protein Expression and Interface Mechanics"

Maryam Eshrati[1,#], **Federico Amadei**[1,#], Simone Staffer[2], Wolfgang Stremmel[2,3], and Motomu Tanaka[1,4,*]

[1] Physical Chemistry of Biosystems, Institute of Physical Chemistry, Heidelberg University, D69120 Heidelberg, Germany

[2] Internal Medicine IV, University Hospital Heidelberg, D69120 Heidelberg, Germany

[3] Medical Center Baden-Baden, D76530 Baden-Baden, Germany

[4] Center for Integrative Medicine and Physics, Institute for Advanced Study, Kyoto University, 606-8501 Kyoto, Japan

[#] **Equal contribution**

Author Contributions:

M.E. and **F.A** performed all aspects and data analysis of the experiments presented in this chapter. M.E. took a special care of the bacteria cell cultures and optimized the staining with DAPI. F.A took special care of the AFM experiments. S.S. took care of the cell culture of Caco2 and HT29 MTX cell lines. W.S contributed intellectually to the discussion and interpretation of the results. M.T. participated in the conception and design of the experiments described here and was involved in manuscript writing.

6.1.Summary

The oral uptake of probiotic microorganisms as food additives is one widely taken strategy to sustain and improve the homeostasis of intestinal microbiota that protect the intestinal epithelia from the attack of pathogenic bacteria. Once delivered to ileum and colon, probiotics must adhere and form colonies on mucus that coats the surface of intestinal epithelial cells. Although an increasing amount of knowledge about the genetic and molecular level mechanisms of probiotics-mucus interactions has been accumulated, little is known about the physicochemical aspects of probiotics-mucus interactions under physiological shear in intestines. Here, we established the well-defined models of intestinal epithelial cell monolayers based on two major constituents of gut epithelia, enterocytes and goblet cells. First, the formation of polarized cell monolayer sealed by tight junctions was monitored by transepithelial electrical resistance over time. The establishment of tight junctions and secretion of mucus proteins (mucin) was confirmed by the immunofluorescence staining. In the next step, we measured the elasticity of cell monolayer surfaces by indentation using particle-assisted atomic force microscopy. The effective elastic modulus of goblet cell-like cells was 30 times smaller compared to the one of enterocyte-like cells, which can be attributed to the secretion of a 3 µm-thick mucin layer. As probiotics, we took *Lactobacillus rhamnosus* GG (LGG), which is one of the most widely used strains as food additives. To investigate the dynamic adhesion of LGG to the intestine model surface, we transferred the epithelial cell monolayer into a microfluidic chamber. A distinct difference in dynamic adhesion between two cell types was observed, which could be attributed to the difference in the mucin expression amount. Remarkably, we found that the dynamic LGG adhesion is enhanced by the increase in shear stress, showing the maximum binding efficiency at 0.3 Pa. Finally, we examined the persistence of LGG adhesion by step-wisely increasing the shear stress exerted on adherent LGG, demonstrating that LGG could withstand high shear stresses even beyond the physiological ones. The obtained results open a large potential to quantitatively understand the influence of engineered foods and probiotics on the homeostasis of microbiota on the surface of intestinal epithelia.

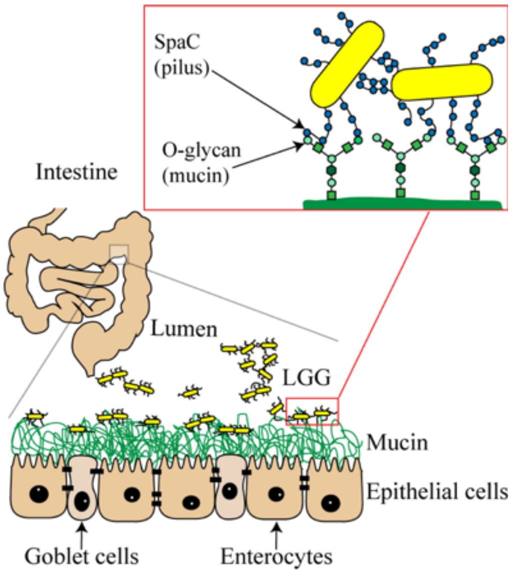

Scheme 6.1: Schematic illustration of the surface of intestinal epithelia and their interaction with LGG. Enterocytes are in charge of nutrients absorption, sharing the largest population. The surface of epithelia is covered by mucin proteins, secreted by goblet cells. Probiotic bacteria, such as *Lactobacillus rhamnosus* GG (LGG), adhere and form colonies by the binding of SpaC subunit of pilus to O-glycan of mucin.

6.2. Results and Discussion.

6.2.1. Characterization of differentiated intestinal epithelial cell monolayers.

In the first step, the growth and differentiation of HT29 MTX and Caco2 were monitored by measuring TEER over time. As presented in Fig. 6.1 (a), TEER of HT29 MTX after 2d was $\text{TEER}_{\text{HT29 MTX, 2d}} \approx 90\ \Omega\cdot\text{cm}^2$. $\text{TEER}_{\text{HT29 MTX}}$ exhibited a monotonic increase according to the growth of cells and reached $\text{TEER}_{\text{HT29 MTX, 21 d}} \approx 500\ \Omega\cdot\text{cm}^2$ after 21 d, suggesting the formation of a polarized epithelial cell layer connected by tight junctions.[230] The same tendency was observed for Caco2, showing a clear increase from $\text{TEER}_{\text{Caco2, 2d}} \approx 60\ \Omega\cdot\text{cm}^2$ to $\text{TEER}_{\text{Caco2, 21 d}} \approx 400\ \Omega\cdot\text{cm}^2$.[231] Fig. 6.1 (c) shows the immunofluorescence image of HT29 MTX monolayer with anti-ZO-1 (red) after 21 d. Cell nuclei were stained with DAPI (blue). As described in the previous section, mucin was removed prior to the immunostaining in order that the accessibility of anti-ZO-1 is not disturbed by the mucin layer. ZO-1 signals were accumulated near the borders between cells, suggesting that the cells were connected by tight junctions. Some cell borders that apparently crossed nuclei suggested the "tilt" of cell boundaries from the direction perpendicular to the substrate. The secretion of mucin was verified by immunofluorescence labeling of mucin MUC5AC. Fig. 6.1 (d) represents the side view of the HT29 MTX monolayer, confirming that the apical surface was homogeneously covered by a mucin layer (green) with the thickness of ≈ 3 µm. This seems to agree well with the previous account reporting the formation of 3 – 5 µm-thick mucin layer on the surface of HT29 MTX after 28 d.[232]

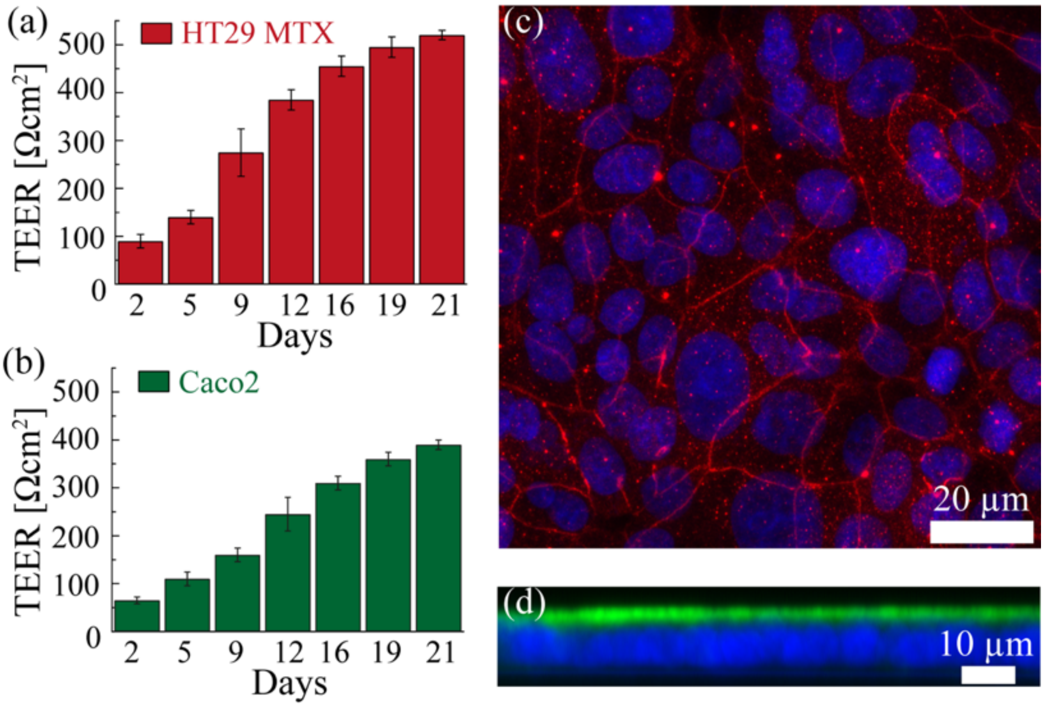

Fig. 6.1: Maturation of epithelial cell monolayers connected by tight junctions. Changes in transepithelial electrical resistance (TEER) of (a) HT29 MTX and (b) Caco2 were monitored over time.

(c) Immunofluorescence images of HT29 MTX after 21 d. Red: ZO-1 (tight junction protein), blue: cell nuclei (DAPI). (d) Cross-sectional image (side view) HT29 MTX monolayer, confirming secretion of mucin (green) on the apical surface. Blue: cell nuclei (DAPI).

Furthermore, the immunofluorescence staining of HT29 MTX cell monolayers with MUC2 antibodies was attempted by embedding the cell monolayer in paraffin to protect the secreted MUC2. However, it was found that MUC2 was only occasionally present on the apical side, as shown in Fig. 6.2. In fact, a previous study reported the destruction of MUC2 already during formalin fixation.[230]

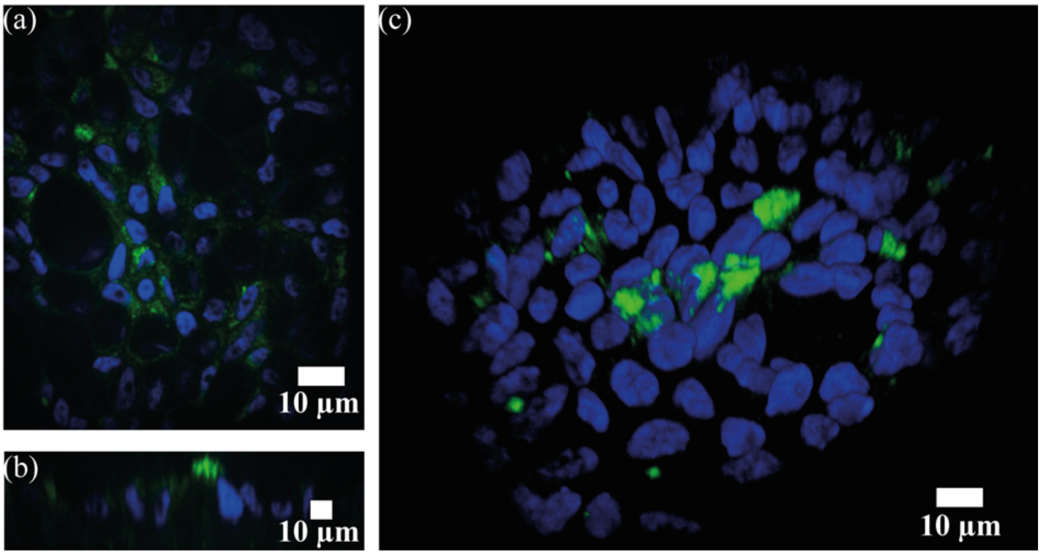

Fig. 6.2: Immunofluorescence staining of HT29 MTX with specific anti MUC2 antibodies. (a) Top view, (b) side view, and (c) 3D reconstruction of the confocal microscopy images. Green: mucin, blue: cell nuclei.

On the other hand, no ZO-1 or MUC5AC signal could be detected when the same immunofluorescence labeling was applied to polarized Caco2 monolayers (Data not shown). The fact that polarized Caco2 showed no immunoreactivity to anti-MUC5AC seems reasonable, since Caco2 does not produce thick mucin layers unless stimulated by growth factors.[232] However, the high level of TEER reached after 21 d, $\mathrm{TEER}_{\mathrm{Caco2,\ 21\ d}} \approx 400\ \Omega\cdot\mathrm{cm}^2$, cannot be explained without the establishment of a tightly connected epithelial cell sheet. Therefore, the lack of ZO-1 signal was attributed to the detachment of cells from the polycarbonate support during the fixation and staining procedures. The possibility if the collagen-coated PTFE or polyester membranes could support Caco2 monolayers better was explored. However, TEER values after 21 d always remained $< 150\ \Omega\cdot\mathrm{cm}^2$, suggesting that Caco2 were not able to undergo the correct differentiation and polarization on PTFE and polyester membranes, as reported in Table 6.1. Therefore, in the following experiments, the differentiation of Caco2 on polycarbonate membranes was always confirmed by TEER measurements, and only used the samples that reached $\mathrm{TEER}_{\mathrm{Caco2}} > 400$ $\Omega\cdot\mathrm{cm}^2$.

Cell / substrate	3 d	7 d	10 d	14 d	17 d	21 d
Caco2 / polyester membrane	60–70	80−100	90−120	90−120	90−120	90−130
Caco2 / PFTE membrane with collagen	40–50	50–80	60−80	–	–	–

Table 6.1: Influence of substrate materials on transepithelial electrical resistance (TEER) of Caco2. Unit: $\Omega\cdot\mathrm{cm}^2$. Culture on the PTFE membrane was aborted after 10 d.

6.2.2.Mechanical properties of intestinal epithelial surfaces.

Fig. 6.3 (a) represents a schematic illustration of the AFM indentation measurements using a cantilever coupled to a microparticle, and the stereo microscopy image of the cantilever is shown in Fig. 6.3 (b). The use of SiO_2 microparticles as probes enabled to minimize the artifacts due to the indentation of free voids and local defects, since the diameter of particles ($\varnothing = 10.2$ µm) is large enough compared to the characteristic mesh size of mucin hydrogels. Fig. 6.3 (c) shows a typical force-indentation curve of the model of goblet cell-like monolayer consisting of polarized HT29 MTX. The best fit result with the Hertz model,[200] (Eq. 3.8, red) yielded the effective elastic modulus of the surface of differentiated HT29 MTX, $E_{\mathrm{HT29\ MTX}} = 0.21 \pm 0.03$ kPa. Fig. 6.3 (d) represents the typical force-indentation curve of the model of enterocyte-like monolayer, which consists of polarized Caco2. The same model was applied for the fit with the Hertz model (green) yielding the effective elastic modulus, $E_{\mathrm{Caco2}} = 9.6 \pm 1.1$ kPa. It is remarkable that the effective elastic modulus of the enterocyte-like monolayer derived from Caco2 is by a factor of 30 larger than that of the monolayer of goblet cell-like cells derived from HT29 MTX. This finding suggests that the surface elasticity of goblet cell-like HT29 MTX is lower due to the secretion of a 3 µm-thick mucin layer, while that of enterocyte-like Caco2 reflects the elasticity of intestinal villi on the apical surface with conserved structural architectures. In fact, the detachment of mucin from the cell surface after many indentation measurements was observed.

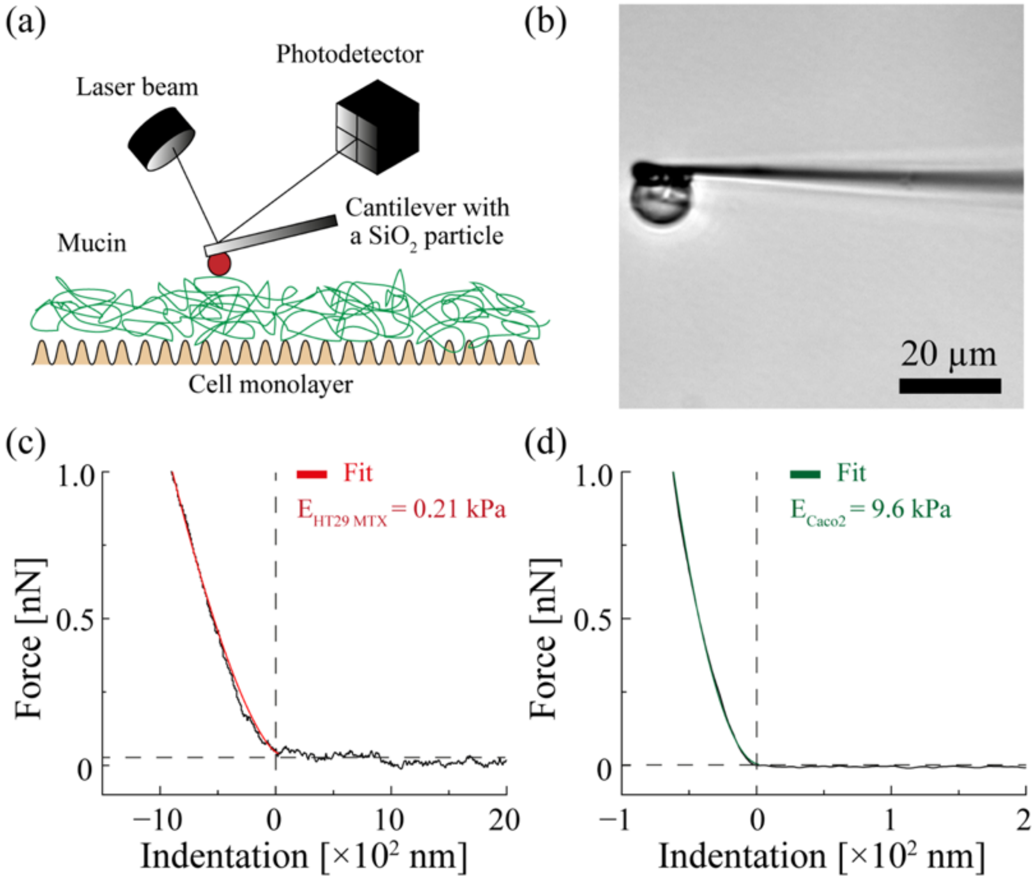

Fig. 6.3: Elastic modulus of cell monolayer measured by particle-assisted AFM indentation. (a) Scheme of the experimental setup. (b) Side view of the cantilever coupled to a SiO_2 particle (∅ = 10.2 µm). Typical force-indentation curves of polarized (c) HT29 MTX and (d) Caco2 monolayers. The experimental data (black) were fitted with the Hertz model (Eq. 3.8), yielding the elastic moduli of $E_{HT29\ MTX} \approx 0.21$ kPa and $E_{Caco2} \approx 9.6$ kPa, respectively.

It should be noted that the indentation force was set (1 nN) constant throughout the whole series of experiments and thus the indentation depth for HT29 MTX (1000 nm) was larger than Caco2 (100 nm). Nevertheless, the calculated effective elastic modulus of HT29 MTX was not influenced even by limiting the indentation depth to 100 nm, as demonstrated in Fig. 6.4.

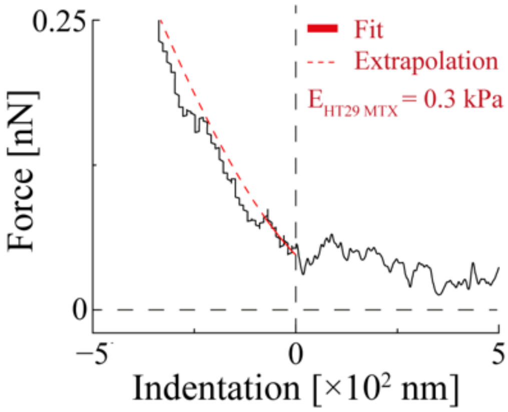

Fig. 6.4: Elastic modulus of goblet cell-like HT29 MTX cell monolayer is not influenced by the range of indentation depth. The experimental data (black) were fitted with the modified Hertz model (Eq. 1) by limiting the fitting range down to 100 nm. The fit (red) yielded the elastic modulus of $E_{\mathrm{HT29\ MTX}}$ ≈ 0.3 kPa, which confirmed our findings presented in Fig. 6.3 (c).

Last but not least, the effective elastic modulus values of HT29 MTX and Caco2 obtained from all the indentation curves subjected to the analysis implied that the effective elastic moduli of the two cell types are distinctly different, as shown in Fig. 6.5.

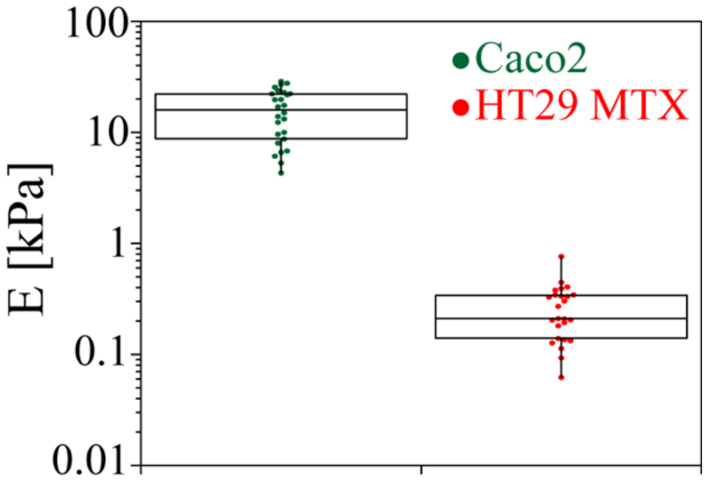

Fig. 6.5: Statistical analysis of the indentation force curves. Effective elastic modulus of enterocyte-like Caco2 monolayer (green) is distinctly larger compared to that of goblet cell-like HT29 MTX monolayer (red).

To validate the comparison of data obtained from two different cell types, the experimental conditions were carefully set constant throughout the entire series of experiments, such as the spring constant of the cantilever, indentation speed and force, SiO_2 probe particles, medium, temperature and the sample container. Several studies suggested that the comparison of indentation data, especially those of biological cells, must be handled with care, because they have shown significant deviations by altering the experimental conditions.[233] As a matter of cause, the effective elastic modulus values measured at room temperature can hardly be compared to the values measured at 37 °C.[234] Moreover, it was ensured that the biological conditions of the two cell types were kept as comparable as possible. Each cell line contains a uniform population, which has been confirmed to differentiate into a single phenotype.[235] Both types of cells underwent the differentiation into enterocyte-like cells and goblet cell-like cells in Transwell culture systems showing TEER = 400 – 500 $\Omega\cdot\text{cm}^2$ after 21 d.[230, 231] Indeed, the control of cells biological identities was extremely critical. For example, the effective elastic modulus of differentiated HT29 MTX, $E_{\text{HT29 MTX}} = 0.21 \pm 0.03$ kPa, apparently seems smaller than that of HT29 cells, $E_{\text{HT29}} \approx 1$ kPa, reported in a previous account.[236] However, in this study, it was not explicitly documented whether the cells were properly differentiated or not. Moreover, looking into the subsets, the HT29 line used in the previous study contains a heterogeneous mixture of various cells, among which < 5 % of the cells secreted mucin.[237] This is clearly different from the HT29 MTX line, which contains a homogenous subpopulation that can all undergo the differentiation into a goblet cell-like phenotype secreting mucin.[238] The differentiation of cells also seemed to influence the mechanical properties of cells significantly. The effective elastic modulus of "differentiated" enterocyte-like Caco2 monolayer obtained in this study, $E_{\text{Caco2}} = 9.6 \pm 1.1$ kPa, is almost by a factor 20 larger than the previously reported value for "single" Caco2 cells, $E_{\text{Caco2,single}} \approx 0.6$ kPa.[239] Needless to say, the comparison of the effective elastic moduli should be handled carefully, as the obtained values are strongly influenced by the measurement setups and experimental conditions. Nevertheless, it seems plausible that the effective elastic modulus of the properly differentiated, polarized enterocyte-like cells connected by tight junctions is larger than that of single cells. Actually, Schimpel et al. previously reported that the doping of membranous epithelial cells into Caco2 monolayers results in not only a significant decrease in TEER but also a distinct change in the appearance of indentation curves qualitatively, which was attributed to the softening.[240]

6.2.3. Dynamic adhesion of LGG on intestinal epithelial surface models.

To physically model the adhesion of released LGG onto intestinal mucus surfaces, the monolayer of intestinal epithelial cells was transferred to a microfluidic chamber, as presented in Fig. 6.6 (a). The shear stress near the surface can be calculated from the height h and the width w of the channel, the viscosity of the medium η, and the volume flux Φ (Eqs. 3.5 – 3.7). As shown in Fig. 6.6 (b), the "blank" surface of polarized HT29 MTX and Caco2 monolayers was exposed to the flow of LGG suspension (5 mL) at a defined shear stress, and the number of adherent LGG was counted. The range of shear stresses from $\tau = 0.1 - 0.5$ Pa was selected because it corresponds to physiological shear stress conditions in the human gastrointestinal tract.[39] In order to gain a better visualization and make the counting easier, LGG were stained with DAPI (Fig. 6.6 (c)). Fig. 6.6 (d) shows the number of LGG adherent on the polarized HT29 MTX monolayer (red) and Caco2 monolayer (green) plotted as a function of shear stress. First, it was found that the adhesion of LGG was more significant on HT29 MTX compared to Caco2 under all the shear conditions, which qualitatively agrees with the data obtained under static conditions.[241] The more significant adhesion on HT29 MTX could be attributed to the amount of glycan expressed on the surface of each cell monolayer. HT29 MTX secrete a 3 μm-thick mucin layer enriched with O-glycan side chains (Fig. 6.1 (d)), while the surface of Caco2 is covered by glycocalyx mainly consisting of transmembrane mucins (MUC3, MUC12 and MUC17).[242] Although both O-glycan side chains on HT29 MTX and transmembrane mucin of Caco2 can serve as the binding ligands to lectin-like SpaC, AFM indentation results denoted that the surface of HT29 MTX is coated with a softer layer of highly glycosylated mucin (Fig. 6.4 (c)). The more significant adhesion of LGG on HT29 MTX compared to Caco2 was also reported for the monolayers cultured in well plates for 15 d under static conditions,[241, 243] but the influence of flow and hence shear stress has never been discussed.

More remarkably, it was found that the dynamic adhesion of LGG to the intestinal model surface does not monotonically increase or decrease as the shear stress was increased, taking the maxima at $\tau^* = 0.3$ Pa on both surfaces. Intriguingly, the number of adherent cells on polarized HT29 MTX at 0.3 Pa (≈ 700) is one order of magnitude larger compared to that observed at 0.1 Pa. Although the number of adherent LGG on polarized Caco2 is distinctly less, the number of adherent LGG was enhanced by one order of magnitude by increasing the shear stress from 0.1 to 0.3 Pa. This is, to the best of what has been reported so far, the first study demonstrating that the dynamic binding of LGG is shear-dependent and there is an optimal shear stress τ^* for the LGG adhesion. This finding is fully complementary to the single molecular force spectroscopy study proposing that external shear forces acting on pili can cause the structural change of SpaC, which results in an enhancement of pili-glycan binding.[37] The fact that a larger shear stress than 0.3 Pa led to a decrease in the adhesion events suggests that the flux corresponding to this condition is too high for LGG to establish pili-glycan binding.

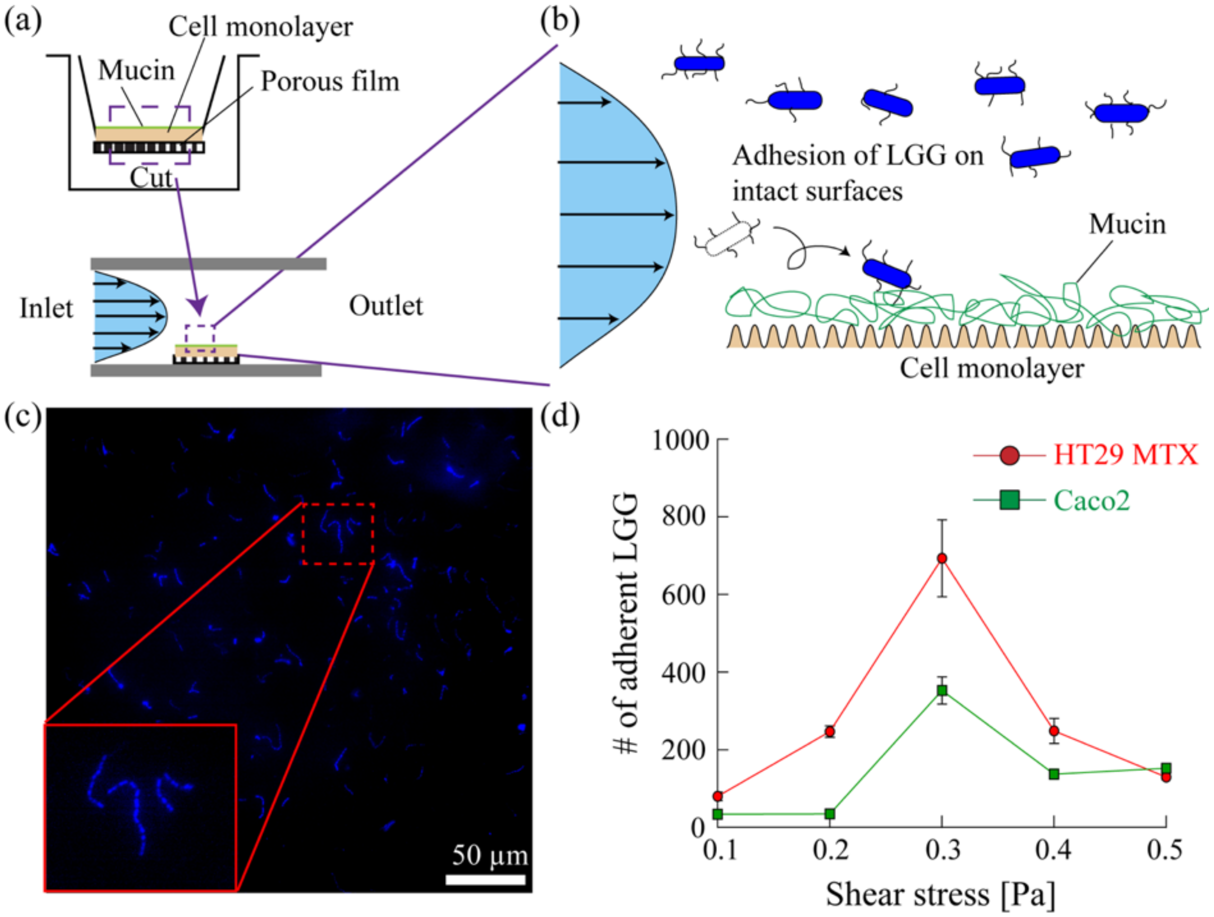

Fig. 6.6: Dynamic adhesion of LGG on intestinal epithelial surface models. (a) Schematic representation of the experimental system. Polarized cell monolayer on porous polymer membrane was transferred into microfluidic chamber. (b) "Blank" surface was exposed to LGG suspension at different shear stresses. (c) Typical snapshot of DAPI-stained LGG adherent on epithelial surface model. (d) Number of adherent LGG in the field of view (332.8 × 332.8 μm^2) plotted as a function of shear stress.

6.2.4.Persistence of LGG adhesion against flow-induced detachment.

Once LGG adhere, they must withstand the shear in order to able to form colonies. To assess the persistence of LGG adhesion against shear, the flow-induced detachment of the cell monolayer pre-occupied with LGG, called "wash-off experiments" was monitored (Fig. 6.7 (a)). Prior to the application of shear, LGG were allowed to adhere on the cell monolayers for 30 min. The fraction of remaining DAPI-stained LGG (Fig. 6.7 (b)) was monitored during the step-wise increase in the shear stress from τ = 0.03 to 1.2 Pa by fluorescence microscopy. Fig. 6.7 (c) represents the percentage of remaining cells on the surface of cell monolayer plotted as a function of shear stress. First, no sign of LGG detachment in the full range of applied shear stresses (green) was observed. Note that the maximum stress exerted on LGG was τ_{max} = 1.2 Pa, which is much larger than the typical shear stress in intestines (0.1 – 0.5 Pa). This clearly indicates that LGG firmly stay on the mucus surface once they adhere. The fraction of adherent LGG on HT29 MTX seemed to take its maximum at 0.1 Pa. However, it should be noted that this point is beyond the initial level (100 %) suggesting that this “apparent” maximum can be attributed to LGG flowing into the field of observation. Actually, this one levels off to ≈100 % at elevated shear stresses. On the other hand, on polarized Caco2 monolayer, it was found that approximately 25 % of LGG were detached already at the shear stress of 0.1 Pa, denoting that LGG adhesion is much less persistent compared to HT29 MTX. The increase in shear stress led to further detachment events, but more than 50 % of LGG remained even at $\tau = 0.8$ Pa, beyond which the whole cell monolayer was detached from the polymer membrane. The obtained results implied that the LGG adherent on the model of intestinal epithelial monolayer is persistent at a wide range of shear stresses even beyond the level of physiological ones, which can be attributed to the shear-enhanced pili-glycan binding. Furthermore, the more significant persistence that LGG exhibited on polarized HT29 MTX compared to Caco2 could be attributed to the larger amount of glycan expressed on the surface of HT29 MTX as well as to the physical entrapment of LGG in the three-dimensional gel of secreted mucin.

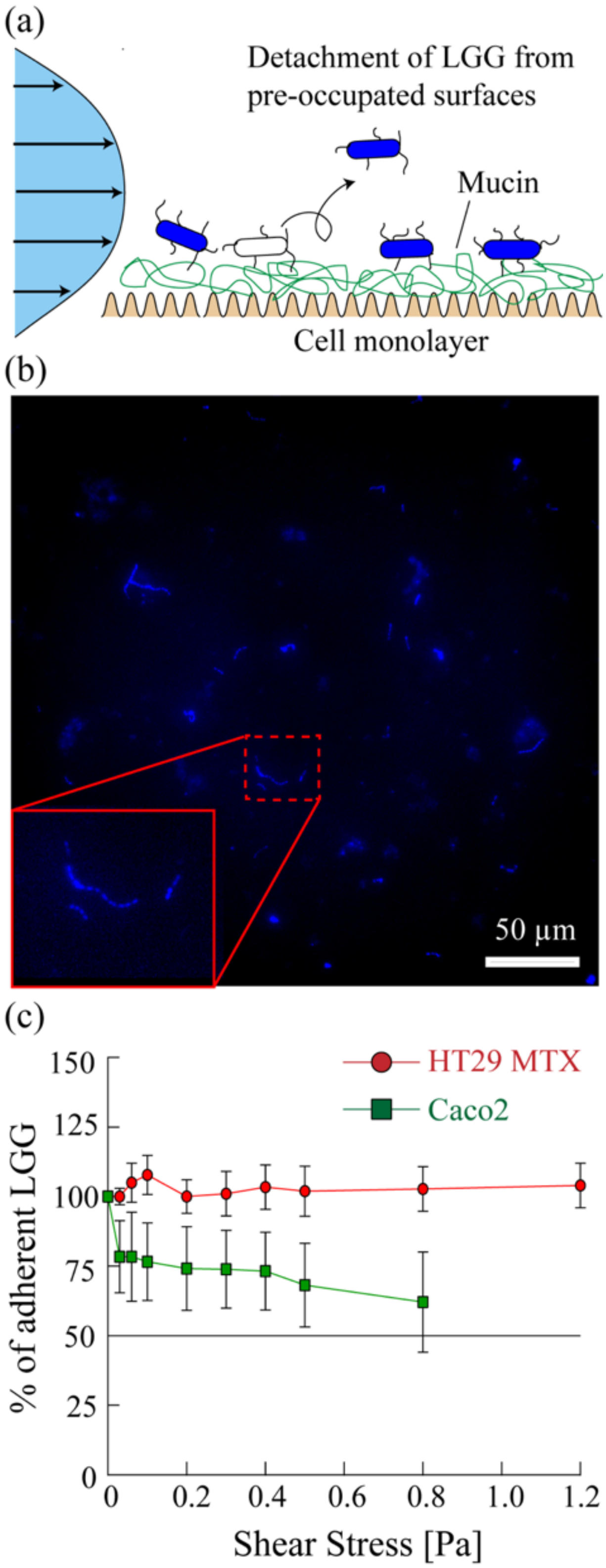

Fig. 6.7: Persistence of LGG on intestinal epithelial surface models via wash-off assays. (a) Schematic representation of wash-off assay. LGG were firstly allowed to adhere on the cell monolayer (30 min), the shear stress exerted on adherent LGG was increased step-by-step. (b) Typical snapshot of DAPI-stained LGG under shear. (c) Percentage of LGG remaining on cell surfaces plotted as a function of shear stress. The level of 50 % (black line) was added to guide the eye.

Conclusions

The aim of this thesis was to quantitatively investigate the fundamental interactions that govern processes to better understand how the homeostasis in the gastrointestinal tract is maintained. This was achieved by means of a combination of experimental techniques including grazing incidence X-ray photon correlation spectroscopy (GI-XPCS), reflection interference contrast microscopy (RICM) and microfluidic experiments, together with the design and application of novel *in vitro* gut models. The novelty of this work consisted in the application for the first time of the GI-XPCS technique to investigate the sol-gel transition of a biopolymer at the liquid/liquid interface, which still remains an open challenge.

In Chapter 4 the gelation dynamics of sodium alginate was investigated by means of interfacial stress rheometry in combination with a cutting-edge application of the XPCS technique at the liquid/liquid interface. Preliminary SAXS-XPCS measurements performed to test the gelation of polyalginate in bulk showed a clear difference in the decay time of the intensity autocorrelation function, which increased by a factor 200 from the sol to the gel state, accompanied by an alteration of the function shape from a "stretched" to a "compressed" profile. Subsequently, the gelation of polyalginate at the oil/water interface was monitored by means of interfacial stress rheometry. The experimental curves where fitted with an asymmetrical sigmoidal model and it was found that the reaction lag time was $t^{lag} = 168$ min for PA 1.5 wt%, after which the elastic modulus increased rapidly, hinting to a clear sign of interfacial gelation. Interestingly, the reaction reached the saturation level after approx. 600 min of delay time, the former being proportional to the polyalginate concentration. The same time window was kept for GI-XPCS experiments. It was found that the structural relaxation process slows down as the reaction proceeds, which is reflected in an increase of the decay time τ of the intensity autocorrelation functions of approx. 23 times between $t = 0$ and $t = 580$ min. Interestingly, the increase of τ within the initial lag time suggested that the slowdown of the structural relaxation process occurs already at a nanoscale level, in contrast to what was observed macroscopically via ISR. On the other hand, the interfacial gelation is accompanied by an increase in the Kohlrausch shape parameter of the intensity ACFs, similar to what was observed for PA in bulk. Furthermore, the relaxation rate showed a linear dependence on the probed scattering vector in all investigated cases. This finding, together with the fact that the decay time of the intensity ACFs did not show any dependence on the perpendicular component of the scattering vector, was a clear sign that the gelation is confined at the liquid/liquid two-dimensional interface.

In Chapter 5, the underlying mechanism governing the accumulation of PC on mucosal surfaces was investigated. Here, the significance of PC-mucin interaction was quantitatively determined by using *in vitro* model of intestinal surfaces and label-free microinterferometry. The model of intestinal mucus surfaces was fabricated by the quantitative functionalization of supported lipid membranes with mucin. The step-wise fabrication of the surrogate surfaces was monitored by QCM-D and fluorescent labeling, confirming the formation of a uniform mucin layer with the thickness of ≈ 30 nm. The potential of interfacial interactions $V(\Delta h)$ between microparticles (diameter: 10 μm) and mucin was calculated by analytically solving the Langevin equation of the height fluctuation of the particles, monitored by RICM. Within the framework of Derjaguin's approximation, $V(\Delta h)$ in the vicinity of the minimum was approximated as a harmonic potential, and the second derivative of the potential and thus the spring constant $V''(\Delta h)$ was used to assess the sharpness of the potential confinement. Since mucins are highly glycosylated proteins containing a large amount of sialic acid residues, the interactions of latex microparticles carrying different surface charges was first investigated and found that the spring constant V'' follows the classical electrostatic interactions. The spring constant of carboxy-terminated latex particle (−) increased by a factor of 30 by the deposition of an additional chitosan layer (+). On the other hand, silica particles coated with lipids with differently charged headgroups exhibited a completely different tendency. The particles coated with zwitterionic DOPC (±) showed a much sharper confinement compared to the particles coated with DOPC/DOPG (−) and DOTAP (+). The wash-off experiments further confirmed that only particles coated with DOPC (±) could remain stable under physiological shear stresses (0.1 − 0.5 Pa). Finally, to simulate the damaged mucus surfaces in inflammatory bowel diseases, mucin was enzymatically digested by neuraminidase and protease. The fact that the PC-mucin interaction was not retarded but even more enhanced after the enzymatic digestion of mucin suggests that the phospholipid depletion in inflammatory bowel diseases is caused either by the loss of functions to synthesis and transfer of phospholipids through intestinal epithelia or by the elevated digestion of phospholipids by ectophospholipase A_2. Therefore, the obtained results have demonstrated that the luminal supply of PC together with ectophospholipase inhibitors by a delayed release in the damaged intestine is a straightforward strategy to refill and repair the damaged phospholipid barrier in the colon.

In Chapter 6, *in vitro* models of enterocytes (Caco2) and goblet cells (HT29 MTX) were fabricated, to investigate the influence of the mucin expressions levels on the adhesive properties of the probiotic strain *Lactobacillus rhamnosus*. In a first step, the *in vitro* systems were characterized. Caco2 and HT29 MTX cultured in the Transwell culture systems underwent the differentiation into enterocyte-like cells and goblet cell-like cells connected by tight junctions, which was monitored by the increase in TEER. After 21 d, both Caco2 and HT29 MTX reached TEER ≥ 400 $\Omega\cdot\text{cm}^2$, which is the typical level for a tightly connected, polarized epithelial cell monolayer. The formation of tight junctions and the secretion of mucin in HT29 MTX monolayer was verified by immunofluorescence labeling of tight junction proteins ZO-1 and mucin MUC5AC. The mucin layer was localized on the apical surface of HT29 MTX monolayer, whose thickness was about 3 μm. In the next step, the mechanical properties of the surfaces of polarized cell monolayers were characterized by particle-assisted AFM indentation. The cantilever was coupled to a 10.2 μm-large SiO_2 particle, which minimizes the artifacts caused by indenting free voids or defects. The bulk elastic modulus of polarized HT29 MTX monolayer calculated from the Hertz

model was $E_{\mathrm{HT29\ MTX}} \approx 0.21$ kPa, which can be attributed to the layer of secreted mucin. On the other hand, the elastic modulus of Caco2 monolayer was, $E_{\mathrm{Caco2}} \approx 9.6$ kPa, which is by a factor of 30 larger than that of HT29 MTX monolayer. As the experimental conditions were set constant, the large discrepancy in elasticity was interpreted in terms of the difference in mucin expression: goblet cell-like cells derived from HT29 MTX secrete 3 μm-thick mucin (MUC2 and MUC5AC), while mucin secreted by Caco2 (MUC3, MUC12 and MUC17) are membrane-bound mucins that constitute the glycocalyx.
In a second step, the interaction of LGG microorganisms with these intestinal epithelial models were investigated under shear stresses mimicking the environment *in vivo*. The epithelial cell monolayer cultured on a porous polymer membrane was transferred into a microfluidic chamber, and the dynamic adhesion of DAPI-labeled LGG to the "blank" surface of cell monolayers was monitored by fluorescence microscopy at different shear stresses covering the physiological ones, $\tau = 0.1 - 0.5$ Pa. The number of LGG adhering on polarized HT29 MTX was higher than that on polarized Caco2 monolayer under every shear condition, which could correspond to the larger amount of glycosylated mucin secreted by goblet cell-like HT29 MTX. Furthermore, the LGG-mucin interaction exhibited a distinct shear enhancement, taking the maximum values at $\tau^* = 0.3$ Pa on both surfaces. This finding agrees well with a single molecule force spectroscopy study, implying that the binding of SpaC to O-glycan is enhanced by shear-induced conformational change of SpaC. The adhesion of LGG was found to be highly persistent, when the shear stress exerted on adherent LGG was step-wisely increased in the wash-off assays. These results did not only demonstrate that there is an optimal shear stress for the dynamic adhesion of LGG to the intestinal epithelial surface, $\tau^* = 0.3$ Pa, but also unraveled the significant persistence of adherent LGG against high shear stresses.

In conclusion, the results of this study demonstrated that the application of advanced experimental techniques in combination with *in vitro* models can provide new insights on one hand, on the investigation of microscopic transition phenomena taking at soft liquid/liquid interfaces; on the other hand, to quantitatively understand how engineered supplements, foods, and probiotics can influence the intestinal microbiota and the intestine homeostasis altogether.

Appendix

AI Additional Fig. to Chapter 4.

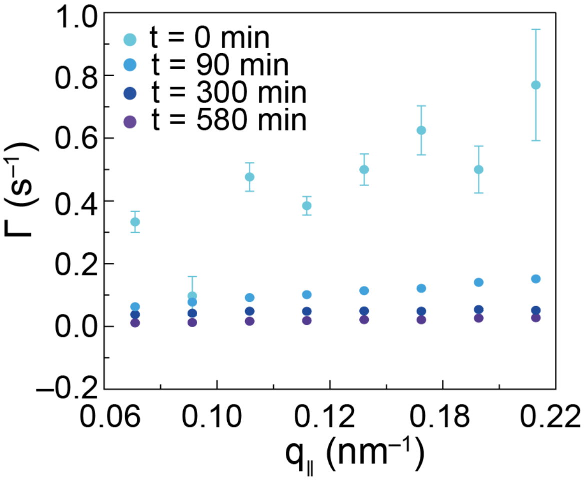

A1: Slowdown of the structural relaxation process proved by the relaxation rate Γ plotted vs. $q_{//}$. Zoom-out of Fig. 4.5 (d) presenting the relaxation rate Γ plotted vs. $\boldsymbol{q_{//}}$ including the data at t = 0 min, which also shows a linear dependence on the scattering vector.

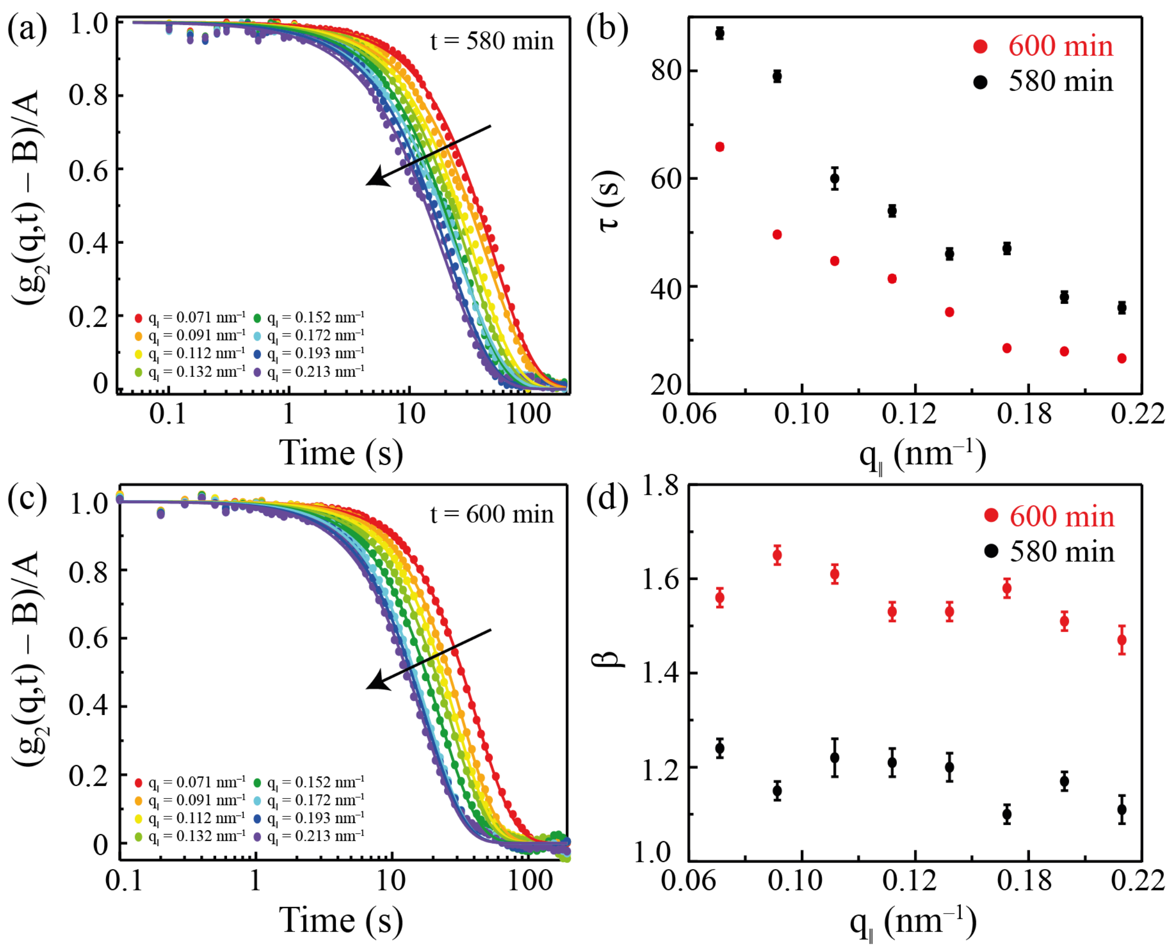

A2: GI-XPCS of PA at the o/w interface and the aging effect. (a) The intensity ACFs measured at t = 580 min showed a strong dependency on $\boldsymbol{q}_{//}$. (b) The same trend is observed for t =600. (c) Remarkably the decay times of the $g_2(\boldsymbol{q},t)$ for t = 600 min are smaller than those for t = 580, therefore they do not follow the observed trend so far. (d) However, this could be related to the fact that the form factor increases from $\beta \approx 1.2$ to $\beta \approx 1.5$ for all $\boldsymbol{q}$s, that is reflected in a more "compressed" form of the ACFs and suggests the presence of a complex underlying dynamics.

List of Publications

1. Korytowski, A., Abuillan, W., **Amadei, F.**, Makky, A., Gumiero, A., Sinning, I., ... & Tanaka, M. (2017). Accumulation of phosphatidylcholine on gut mucosal surface is not dominated by electrostatic interactions. *Biochimica et Biophysica Acta (BBA)-Biomembranes,* 1859(5), 959-965.

2. Eshrati, M., **Amadei, F.**, Van de Wiele, T., Veschgini, M., Kaufmann, S., & Tanaka, M. (2018). Biopolymer-Based Minimal Formulations Boost Viability and Metabolic Functionality of Probiotics Lactobacillus rhamnosus GG through Gastrointestinal Passage. *Langmuir*, *34*(37), 11167-11175.

3. Pavel, I. A., Girardon, M., El Hajj, S., Parant, S., **Amadei, F.**, Kaufmann, S., ... & Pasc, A. (2018). Lipid-coated mesoporous silica microparticles for the controlled delivery of β-galactosidase into intestines. *Journal of Materials Chemistry B*, *6*(35), 5633-5639.

4. Eshrati, M., **Amadei, F.**, Staffer, S., Stremmel, W., & Tanaka, M. (2018). Shear-Enhanced Dynamic Adhesion of Lactobacillus rhamnosus GG on Intestinal Epithelia: Correlative Effect of Protein Expression and Interface Mechanics. *Langmuir*, *35*(2), 529-537.

5. **Amadei, F.**, Fröhlich, B., Stremmel, W., & Tanaka, M. (2018). Nonclassical Interactions of Phosphatidylcholine with Mucin Protect Intestinal Surfaces: A Microinterferometry Study. *Langmuir*, *34*(46), 14046-14057.

6. Masuda, S., Mielke, S., **Amadei, F.**, Yamamoto, A., Wang, P., Taniguchi, T., ... & Tanaka, M. (2018). Nonlinear Viscoelasticity of Highly Ordered, Two-Dimensional Assemblies of Metal Nanoparticles Confined at the Air/Water Interface. *Langmuir*, *34*(43), 13025-13034.

7. Falco, C. Y., **Amadei, F.**, Dhayal, S. K., Cárdenas, M., Tanaka, M., & Risbo, J. (2019). Hybrid coating of alginate microbeads based on protein-biopolymer multilayers for encapsulation of probiotics. *Biotechnology Progress*. e2806

8. Bentele, T., **Amadei, F.**, Kimmle, E., Veschgini, M., Linke, P., Sontag Gonzales, M., Tennigkeit, J., Ho, A. D., Özbek, S., & Tanaka, M. (2019). New Class of Crosslinker-Free Nanofiber Biomaterials from *Hydra* Nematocyst Proteins. *Scientific reports*, SUBMITTED

References.

1. Collins JK, Thornton G, Sullivan GO. Selection of Probiotic Strains for Human Applications*. Int. Dairy J.* 1998, 8:487-490.
2. Sonnenburg JL, Angenent LT, Gordon JI. Getting a Grip on Things: How do Communities of Bacterial Symbionts Become Established in our Intestine? *Nat. Immunol.* 2004, 5:569-673.
3. Williams JM, Duckworth CA, Burkitt MD, Watson AJM, Campbell BJ, Pritchard DM. Epithelial Cell Shedding and Barrier Function: A Matter of Life and Death at the Small Intestinal Villus Tip*. Vet. Pathol.* 2015, 52:445-455.
4. Pelaseyed T, Bergström JH, Gustafsson JK, Ermund A, Birchenough GMH, Schütte A, van der Post S, Svensson F, Rodríguez-Piñeiro AM, Nyström EEL, et al. The Mucus and Mucins of the Goblet Cells and Enterocytes Provide the First Defense Line of the Gastrointestinal Tract and Interact with the Immune System*. Immunol. rev.* 2014, 260:8-20.
5. Forstner J, Taichman N, Kalnins V, Forstner G. Intestinal Goblet Cell Mucus: Isolation and Identification by Immunofluorescence of a Goblet Cell Glycoprotein*. J. Cell Sci.* 1973, 12:585-601.
6. Thornton DJ, Rousseau K, McGuckin MA. Structure and Function of the Polymeric Mucins in Airways Mucus*. Annu. Rev. Physiol.* 2008, 70:459-486.
7. Perez-Vilar J, Hill RL. The Structure and Assembly of Secreted Mucins*. J. Biol. Chem.* 1999, 274:31751-31754.
8. Specian RD, Oliver MG. Functional Biology of Intestinal Goblet Cells*. Am. J. Physiol. Cell Ph.* 1991, 260:C183-C193.
9. Stremmel W, Ehehalt R, Staffer S, Stoffels S, Mohr A, Karner M, Braun A. Mucosal Protection by Phosphatidylcholine*. Digest. Dis.* 2012, 30(suppl 3):85-91.
10. Lugea A, Salas A, Casalot J, Guarner F, Malagelada J-R. Surface Hydrophobicity of the Rat Colonic Mucosa is a Defensive Barrier Against Macromolecules and Toxins*. Gut* 2000, 46:515-521.
11. Ehehalt R, Jochims C, Lehmann W-D, Erben G, Staffer S, Reininger C, Stremmel W. Evidence of Luminal Phosphatidylcholine Secretion in Rat Ileum*. BBA-Mol. Cell. Biol. L.* 2004, 1682:63-71.
12. Stremmel W, Staffer S, Gan-Schreier H, Wannhoff A, Bach M, Gauss A. Phosphatidylcholine Passes Through Lateral Tight Junctions for Paracellular Transport to the Apical Side of the Polarized Intestinal Tumor Cell-Line CaCo2*. BBA-Mol. Cell. Biol. L.* 2016, 1861:1161-1169.
13. Korytowski A, Abuillan W, Amadei F, Makky A, Gumiero A, Sinning I, Gauss A, Stremmel W, Tanaka M. Accumulation of Phosphatidylcholine on Gut Mucosal Surface is not Dominated by Electrostatic Interactions*. BBA-Biomembranes* 2017, 1859:959-965.
14. Eshrati M, Amadei F, Staffer S, Stremmel W, Tanaka M. Shear-Enhanced Dynamic Adhesion of Lactobacillus rhamnosus GG on Intestinal Epithelia: Correlative Effect of Protein Expression and Interface Mechanics*. Langmuir* 2018, 35:529-537.
15. Braun A, Treede I, Gotthardt D, Tietje A, Zahn A, Ruhwald R, Schoenfeld U, Welsch T, Kienle P, Erben G, et al. Alterations of Phospholipid Concentration and Species Composition of the Intestinal Mucus Barrier in Ulcerative Colitis: A Clue to Pathogenesis*. Inflam. Bowel Dis.* 2009, 15:1705-1720.
16. Stremmel W, Merle U, Zahn A, Autschbach F, Hinz U, Ehehalt R. Retarded Release Phosphatidylcholine Benefits Patients with Chronic Active Ulcerative Colitis. *Gut* 2005, 54:966.
17. Stremmel W, Ehehalt R, Autschbach F, Karner M. Phosphatidylcholine for Steroid-Refractory Chronic Ulcerative Colitis: A Randomized Trial*. Ann. Intern. Med.* 2007, 147:603-610.
18. Karner M, Kocjan A, Stein J, Schreiber S, von Boyen G, Uebel P, Schmidt C, Kupcinskas L, Dina I, Zuelch F, et al. First Multicenter Study of Modified Release Phosphatidylcholine "LT-02" in Ulcerative Colitis: A Randomized, Placebo-Controlled Trial in Mesalazine-Refractory Courses*. Am. J. Gastroenterol.* 2014, 109:1041.
19. Stremmel W, Staffer S, Stuhrmann N, Gan-Schreier H, Gauss A, Burger N, Hornuss D. Phospholipase A2 of Microbiota as Pathogenetic Determinant to Induce Inflammatory States

in Ulcerative Colitis: Therapeutic Implications of Phospholipase A2 Inhibitors. *Inflamm. Intest. Dis.* 2017, 2:180-187.

20. Reid G, Chan RC, Bruce AW, Costerton JW. Prevention of Urinary Tract Infection in Rats with an Indigenous Lactobacillus casei Strain. *Infect. Immun.* 1985, 49:320-324.
21. Bernet-Camard MF, Liévin V, Brassart D, Neeser JR, Servin AL, Hudault S. The Human *Lactobacillus acidophilus* Strain LA1 Secretes a Nonbacteriocin Antibacterial Substance(s) Active in vitro and in vivo. *Appl. Environ. Microb.* 1997, 63:2747-2753.
22. Stiles ME, Holzapfel WH. Lactic Acid Bacteria of Foods and Their Current Taxonomy. *Int. J. Food Microbiol.* 1997, 36:1-29.
23. Hill C, Guarner F, Reid G, Gibson GR, Merenstein DJ, Pot B, Morelli L, Canani RB, Flint HJ, Salminen S, et al. The International Scientific Asssociation for Probiotics and Prebiotics Consensus Statement on the Scope and Appropriate Use of the Term Probiotic. *Nat. Rev. Gastroenterol. Hepatol.* 2014, 11:506-514.
24. Schultz M. Clinical Use of *E. coli* Nissle 1917 in Inflammatory Bowel Disease. *Inflamm. Bowel Dis.* 2008, 14:1012-1018.
25. Ouwehand AC, Salminen S. *In vitro* Adhesion Assays for Probiotics and Their *in vivo* Relevance: a Review. *Microb. Ecol. Health Dis.* 2003, 15:175-184.
26. Cohen PS, Laux DC. Bacterial Adhesion to and Penetration of Intestinal Mucus in vitro. *Methods Enzymol.* 1995, 253:309-314.
27. Kirjavainen PV, Ouwehand AC, Isolauri E, Salminen SJ. The Ability of Probiotic Bacteria to Bind to Human Intestinal Mucus. *FEMS Microbiol. Lett.* 1998, 167:185-189.
28. Ouwehand AC, Kirjavainen PV, Grönlund MM, Isolauri E, Salminen SJ. Adhesion of Probiotic Micro-Organisms to Intestinal Mucus. *Int. Dairy J.* 1999, 9:623-630.
29. Carasi P, Ambrosis NM, De Antoni GL, Bressollier P, Urdaci MC, Serradell MdlA. Adhesion Properties of Potentially Probiotic *Lactobacillus kefiri* to Gastrointestinal Mucus. *J. Dairy Res.* 2014, 81:16-23.
30. Tuomola EM, Ouwehand AC, Salminen SJ. The Effect of Probiotic Bacteria on the Adhesion of Pathogens to Human Intestinal Mucus. *FEMS Immunol. Med. Microbiol.* 1999, 26:137-142.
31. Collado MC, Meriluoto J, Salminen S. Role of Commercial Probiotic Strains Against Human Pathogen Adhesion to Intestinal Mucus. *Lett. Appl. Microbiol.* 2007, 45:454-460.
32. Tytgat HLP, Douillard FP, Reunanen J, Rasinkangas P, Hendrickx APA, Laine PK, Paulin L, Satokari R, de Vos WM. *Lactobacillus rhamnosus* GG Outcompetes *Enterococcus faecium* via Mucus-Binding Pili: Evidence for a Novel and Heterospecific Probiotic Mechanism. *Appl. Environ. Microbiol.* 2016, 82:5756.
33. Kankainen M, Paulin L, Tynkkynen S, von Ossowski I, Reunanen J, Partanen P, Satokari R, Vesterlund S, Hendrickx APA, Lebeer S, et al. Comparative Genomic Analysis of *Lactobacillus rhamnosus* GG Reveals Pili Containing a Human- Mucus Binding Protein. *Proc. Natl. Acad. Sci. U S A.* 2009, 106:17193.
34. von Ossowski I, Reunanen J, Satokari R, Vesterlund S, Kankainen M, Huhtinen H, Tynkkynen S, Salminen S, de Vos WM, Palva A. Mucosal Adhesion Properties of the Probiotic *Lactobacillus rhamnosus GG* SpaCBA and SpaFED Pilin Subunits. *Appl. Environ. Microbiol.* 2010, 76:2049-2057.
35. Lebeer S, Claes I, Tytgat HLP, Verhoeven TLA, Marien E, von Ossowski I, Reunanen J, Palva A, de Vos WM, De Keersmaecker SCJ, et al. Functional Analysis of *Lactobacillus rhamnosus GG* Pili in Relation to Adhesion and Immunomodulatory Interactions with Intestinal Epithelial Cells. *Appl. and Environ. Microbiol.* 2012, 78:185-193.
36. Robbe C, Capon C, Coddeville B, Michalski J-C. Structural Diversity and Specific Distribution of O-Glycans in Normal Human Mucins Along the Intestinal Tract. *Biochem. J.* 2004, 384:307-316.
37. Tripathi P, Beaussart A, Alsteens D, Dupres V, Claes I, von Ossowski I, de Vos WM, Palva A, Lebeer S, Vanderleyden J, et al. Adhesion and Nanomechanics of Pili from the Probiotic *Lactobacillus rhamnosus* GG. *ACS Nano* 2013, 7:3685-3697.

38. Lippok S, Radtke M, Obser T, Kleemeier L, Schneppenheim R, Budde U, Netz RR, Rädler JO. Shear-Induced Unfolding and Enzymatic Cleavage of Full-Length VWF Multimers. *Biophys. J.* 2016, 110:545-554.
39. Marzorati M, Vanhoecke B, De Ryck T, Sadaghian Sadabad M, Pinheiro I, Possemiers S, Van den Abbeele P, Derycke L, Bracke M, Pieters J, et al. The HMI™ Module: a New Tool to Study the Host-Microbiota Interaction in the Human Gastrointestinal Tract in vitro. *BMC Microbiol.* 2014, 14:133-133.
40. Gouin S. Microencapsulation: Industrial Appraisal of Existing Technologies and Trends. *Trends Food Sci. Technol.* 2004, 15:330-347.
41. Champagne CP, Fustier P. Microencapsulation for the Improved Delivery of Bioactive Compounds into Foods. *Curr. Opin. in Biotechnol.* 2007, 18:184-190.
42. Gasperini L, Mano JF, Reis RL. Natural Polymers for the Microencapsulation of Cells. *J. R. Soc., Interface* 2014, 11.
43. Eshrati M, Amadei F, Van de Wiele T, Veschgini M, Kaufmann S, Tanaka M. Biopolymer-Based Minimal Formulations Boost Viability and Metabolic Functionality of Probiotics *Lactobacillus rhamnosus* GG through Gastrointestinal Passage. *Langmuir* 2018.
44. Yucel Falco C, Amadei F, Dhayal SK, Cárdenas M, Tanaka M, Risbo J. Hybrid Coating of Alginate Microbeads based on Protein-Biopolymer Multilayers for Encapsulation of Probiotics. *Biotechnology progress* 2019:e2806.
45. Lee KY, Mooney DJ. Alginate: Properties and biomedical applications. *Progress in Polymer Science* 2012, 37:106-126.
46. Ching SH, Bansal N, Bhandari B. Alginate gel particles–A review of production techniques and physical properties. *Critical Reviews in Food Science and Nutrition* 2017, 57:1133-1152.
47. Cook MT, Tzortzis G, Khutoryanskiy VV, Charalampopoulos D. Layer-by-layer coating of alginate matrices with chitosan-alginate for the improved survival and targeted delivery of probiotic bacteria after oral administration. *Journal of Materials Chemistry B* 2013, 1:52-60.
48. Orive G, Ponce S, Hernández RM, Gascón AR, Igartua M, Pedraz JL. Biocompatibility of microcapsules for cell immobilization elaborated with different type of alginates. *Biomaterials* 2002, 23:3825-3831.
49. Voo W-P, Ooi C-W, Islam A, Tey B-T, Chan E-S. Calcium alginate hydrogel beads with high stiffness and extended dissolution behaviour. *European Polymer Journal* 2016, 75:343-353.
50. Lucinda-Silva RM, Salgado HRN, Evangelista RC. Alginate–chitosan systems: In vitro controlled release of triamcinolone and in vivo gastrointestinal transit. *Carbohydrate Polymers* 2010, 81:260-268.
51. Lee JS, Cha DS, Park HJ. Survival of Freeze-Dried Lactobacillus bulgaricus KFRI 673 in Chitosan-Coated Calcium Alginate Microparticles. *Journal of Agricultural and Food Chemistry* 2004, 52:7300-7305.
52. Teixeira A, Deladino L, Fernandes C, Martino M, Molina-García A. Application of Chitosan Coating on Alginate Beads for Cryopreservation Uses. *Journal of Chitin and Chitosan Science* 2014, 2:46-54.
53. Ding WK, Shah NP. Effect of Homogenization Techniques on Reducing the Size of Microcapsules and the Survival of Probiotic Bacteria Therein. *Journal of Food Science* 2009, 74:M231-M236.
54. Heidebach T, Först P, Kulozik U. Microencapsulation of Probiotic Cells for Food Applications. *Critical Reviews in Food Science and Nutrition* 2012, 52:291-311.
55. Poncelet D, Lencki R, Beaulieu C, Halle JP, Neufeld RJ, Fournier A. Production of alginate beads by emulsification/internal gelation. I. Methodology. *Applied Microbiology and Biotechnology* 1992, 38:39-45.
56. SHEU TY, MARSHALL RT. Microentrapment of Lactobacilli in Calcium Alginate Gels. *Journal of Food Science* 1993, 58:557-561.
57. Ruta B, Czakkel O, Chushkin Y, Pignon F, Nervo R, Zontone F, Rinaudo M. Silica nanoparticles as tracers of the gelation dynamics of a natural biopolymer physical gel. *Soft Matter* 2014, 10:4547-4554.

58. Kobayashi K, Huang C-i, Lodge TP. Thermoreversible Gelation of Aqueous Methylcellulose Solutions. *Macromolecules* 1999, 32:7070-7077.
59. Li L, Fang Y, Vreeker R, Appelqvist I, Mendes E. Reexamining the Egg-Box Model in Calcium−Alginate Gels with X-ray Diffraction. *Biomacromolecules* 2007, 8:464-468.
60. Stokke BT, Draget KI, Smidsrød O, Yuguchi Y, Urakawa H, Kajiwara K. Small-Angle X-ray Scattering and Rheological Characterization of Alginate Gels. 1. Ca−Alginate Gels. *Macromolecules* 2000, 33:1853-1863.
61. Liu L, Wu F, Ju X-J, Xie R, Wang W, Niu CH, Chu L-Y. Preparation of monodisperse calcium alginate microcapsules via internal gelation in microfluidic-generated double emulsions. *Journal of colloid and interface science* 2013, 404:85-90.
62. Grübel G, Zontone F. Correlation spectroscopy with coherent X-rays. *Journal of Alloys and Compounds* 2004, 362:3-11.
63. Czakkel O, Madsen A. Evolution of dynamics and structure during formation of a cross-linked polymer gel. *EPL (Europhysics Letters)* 2011, 95:28001.
64. Orsi D, Cristofolini L, Baldi G, Madsen A. Heterogeneous and Anisotropic Dynamics of a 2D Gel. *Physical Review Letters* 2012, 108:105701.
65. Anders M, Robert LL, Hongyu G, Michael S, Orsolya C. Beyond simple exponential correlation functions and equilibrium dynamics in x-ray photon correlation spectroscopy. *New Journal of Physics* 2010, 12:055001.
66. Shinohara Y, Kishimoto H, Yagi N, Amemiya Y. Microscopic Observation of Aging of Silica Particles in Unvulcanized Rubber. *Macromolecules* 2010, 43:9480-9487.
67. Ruta B, Chushkin Y, Monaco G, Cipelletti L, Pineda E, Bruna P, Giordano VM, Gonzalez-Silveira M. Atomic-Scale Relaxation Dynamics and Aging in a Metallic Glass Probed by X-Ray Photon Correlation Spectroscopy. *Physical Review Letters* 2012, 109:165701.
68. Ruta B, Baldi G, Chushkin Y, Rufflé B, Cristofolini L, Fontana A, Zanatta M, Nazzani F. Revealing the fast atomic motion of network glasses. *Nature Communications* 2014, 5:3939.
69. Angelini R, Zulian L, Fluerasu A, Madsen A, Ruocco G, Ruzicka B. Dichotomic aging behaviour in a colloidal glass. *Soft Matter* 2013, 9:10955-10959.
70. Leheny RL. XPCS: Nanoscale motion and rheology. *Current Opinion in Colloid & Interface Science* 2012, 17:3-12.
71. Caronna C, Chushkin Y, Madsen A, Cupane A. Dynamics of Nanoparticles in a Supercooled Liquid. *Physical Review Letters* 2008, 100:055702.
72. Guo H, Bourret G, Corbierre MK, Rucareanu S, Lennox RB, Laaziri K, Piche L, Sutton M, Harden JL, Leheny RL. Nanoparticle Motion within Glassy Polymer Melts. *Physical Review Letters* 2009, 102:075702.
73. Guo H, Bourret G, Lennox RB, Sutton M, Harden JL, Leheny RL. Entanglement-Controlled Subdiffusion of Nanoparticles within Concentrated Polymer Solutions. *Physical Review Letters* 2012, 109:055901.
74. Papagiannopoulos A, Waigh TA, Fluerasu A, Fernyhough C, Madsen A. Microrheology of polymeric solutions using x-ray photon correlation spectroscopy. *Journal of Physics: Condensed Matter* 2005, 17:L279.
75. Derjaguin BV. Some Results From 50 Years' Research on Surface Forces. In: *Surface Forces and Surfactant Systems*. Darmstadt: Steinkopff; 1987, 17-30.
76. Rensing L, Rippe V. *Altern*: Springer; 2014.
77. Britannica TEoE. Large Intestine. 2018. Available at: https://www.britannica.com/science/large-intestine.
78. Khutoryanskiy VV. Supramolecular materials: Longer and safer gastric residence. *Nature materials* 2015, 14:963.
79. Kierszenbaum AL, Tres L. *Histology and Cell Biology: an introduction to pathology E-Book*: Elsevier Health Sciences; 2015.
80. Bansil R, Turner BS. Mucin structure, aggregation, physiological functions and biomedical applications. *Current opinion in colloid & interface science* 2006, 11:164-170.
81. Allen A, Snary D. The structure and function of gastric mucus. *Gut* 1972, 13:666.

82. Perez-Vilar J, Hill RL. Mucin family of glycoproteins. 2004.
83. Hashimoto Y, Tsuiki S, Nisizawa K, Pigman W. Action of Proteolytic Enzymes on Purified Bovine Submaxillary Mucin. *Ann. N. Y. Acad. Sci.* 1963, 106:233-246.
84. Corfield AP, Wagner SA, Clamp JR, Kriaris MS, Hoskins LC. Mucin Degradation in the Human Colon: Production of Sialidase, Sialate O-Acetylesterase, N-Acetylneuraminate Lyase, Arylesterase, and Glycosulfatase Activities by Strains of Fecal Bacteria. *Infect. Immun.* 1992, 60:3971-3978.
85. Lennarz WJ, Lane MD. *Encyclopedia of biological chemistry*: Academic Press; 2013.
86. Nishiyama K, Sugiyama M, Mukai T. Adhesion properties of lactic acid bacteria on intestinal mucin. *Microorganisms* 2016, 4:34.
87. Cummings JH, Macfarlane GT. Role of intestinal bacteria in nutrient metabolism. *Clinical nutrition* 1997, 16:3-11.
88. Eckburg PB, Bik EM, Bernstein CN, Purdom E, Dethlefsen L, Sargent M, Gill SR, Nelson KE, Relman DA. Diversity of the human intestinal microbial flora. *science* 2005, 308:1635-1638.
89. Sommer F, Bäckhed F. The gut microbiota—masters of host development and physiology. *Nature Reviews Microbiology* 2013, 11:227.
90. Wilson M. *Microbial inhabitants of humans: their ecology and role in health and disease*: Cambridge University Press; 2005.
91. Barlament JD. Healthy Fear: Bacteria and Culture in America at the Turn of the Twentieth Century. 2005.
92. Nell S, Suerbaum S, Josenhans C. The impact of the microbiota on the pathogenesis of IBD: lessons from mouse infection models. *Nature Reviews Microbiology* 2010, 8:564.
93. Sears CL. A dynamic partnership: Celebrating our gut flora. *Anaerobe* 2005, 11:247-251.
94. Fuller R. Probiotics in human medicine. *Gut* 1991, 32:439-442.
95. Metchnikoff II. *The prolongation of life: optimistic studies*: Springer Publishing Company; 2004.
96. Vaughan RB. THE ROMANTIC RATIONALIST: A STUDY OF ELIE METCHNIKOFF. *Medical history* 1965, 9:201-215.
97. Coconnier M-H, Lievin V, Hemery E, Servin AL. Antagonistic Activity againstHelicobacter Infection In Vitro and In Vivo by the HumanLactobacillus acidophilus Strain LB. *Applied and Environmental Microbiology* 1998, 64:4573.
98. Afrc RF. Probiotics in man and animals. *Journal of Applied Bacteriology* 1989, 66:365-378.
99. FAO/WHO WG. Guidelines for the evaluation of probiotics in food. 2002.
100. Rijkers GT, de Vos WM, Brummer R-J, Morelli L, Corthier G, Marteau P. Health benefits and health claims of probiotics: bridging science and marketing. *British Journal of Nutrition* 2011, 106:1291-1296.
101. Senaka Ranadheera C, Evans CA, Adams MC, Baines SK. Production of probiotic ice cream from goat's milk and effect of packaging materials on product quality. *Small Ruminant Research* 2013, 112:174-180.
102. Islam MA, Yun C-H, Choi Y-J, Cho C-S. Microencapsulation of live probiotic bacteria. *J Microbiol Biotechnol* 2010, 20:1367-1377.
103. Barba AA, d'Amore M, Chirico S, Lamberti G, Titomanlio G. A general code to predict the drug release kinetics from different shaped matrices. *European Journal of Pharmaceutical Sciences* 2009, 36:359-368.
104. Pawar SN, Edgar KJ. Alginate derivatization: a review of chemistry, properties and applications. *Biomaterials* 2012, 33:3279-3305.
105. Remminghorst U, Rehm BH. Bacterial alginates: from biosynthesis to applications. *Biotechnology letters* 2006, 28:1701-1712.
106. Yang J-S, Xie Y-J, He W. Research progress on chemical modification of alginate: A review. *Carbohydrate polymers* 2011, 84:33-39.
107. Smidsrød O, Skja G. Alginate as immobilization matrix for cells. *Trends in biotechnology* 1990, 8:71-78.

108. Braccini I, Pérez S. Molecular basis of Ca2+-induced gelation in alginates and pectins: the egg-box model revisited. *Biomacromolecules* 2001, 2:1089-1096.
109. Slomiany A, Yano S, Slomiany BL, Glass G. Lipid composition of the gastric mucous barrier in the rat. *Journal of Biological Chemistry* 1978, 253:3785-3791.
110. Wirtz K. Phospholipid transfer proteins. *Annual review of biochemistry* 1991, 60:73-99.
111. Kreuzer M, Strobl M, Reinhardt M, Hemmer MC, Hauß T, Dahint R, Steitz R. Impact of a Model Synovial Fluid on Supported Lipid Membranes. *BBA-Biomembranes* 2012, 1818:2648-2659.
112. Higgins JP, Flicker L. Lecithin for dementia and cognitive impairment. *Cochrane database of systematic reviews* 2000.
113. Attwood S, Choi Y, Leonenko Z. Preparation of DOPC and DPPC supported planar lipid bilayers for atomic force microscopy and atomic force spectroscopy. *International journal of molecular sciences* 2013, 14:3514-3539.
114. Tanford C. *The hydrophobic effect: formation of micelles and biological membranes 2d ed*: J. Wiley.; 1980.
115. McAuliffe C. Solubility in water of paraffin, cycloparaffin, olefin, acetylene, cycloolefin, and aromatic hydrocarbons1. *The Journal of Physical Chemistry* 1966, 70:1267-1275.
116. van der Spoel D, van Maaren PJ, Larsson P, Tîmneanu N. Thermodynamics of hydrogen bonding in hydrophilic and hydrophobic media. *The Journal of Physical Chemistry B* 2006, 110:4393-4398.
117. Sackmann E. Biological membranes architecture and function. *Structure and Dynamics of Membranes* 1995, 1:1-63.
118. Tanaka M, Sackmann E. Polymer-supported membranes as models of the cell surface. *Nature* 2005, 437:656.
119. Groves JT, Dustin ML. Supported planar bilayers in studies on immune cell adhesion and communication. *Journal of immunological methods* 2003, 278:19-32.
120. Groves JT, Boxer SG. Micropattern formation in supported lipid membranes. *Accounts of chemical research* 2002, 35:149-157.
121. Sackmann E. Supported membranes: scientific and practical applications. *Science* 1996, 271:43-48.
122. Watts TH, Gaub HE, McConnell HM. T-cell-mediated association of peptide antigen and major histocompatibility complex protein detected by energy transfer in an evanescent wave-field. *Nature* 1986, 320:179.
123. Kalb E, Frey S, Tamm LK. Formation of supported planar bilayers by fusion of vesicles to supported phospholipid monolayers. *Biochimica et Biophysica Acta (BBA)-Biomembranes* 1992, 1103:307-316.
124. Bayerl TM, Bloom M. Physical properties of single phospholipid bilayers adsorbed to micro glass beads. A new vesicular model system studied by 2H-nuclear magnetic resonance. *Biophysical journal* 1990, 58:357-362.
125. Tatulian SA, Hinterdorfer P, Baber G, Tamm LK. Influenza hemagglutinin assumes a tilted conformation during membrane fusion as determined by attenuated total reflection FTIR spectroscopy. *The EMBO Journal* 1995, 14:5514-5523.
126. Terrettaz S, Stora T, Duschl C, Vogel H. Protein binding to supported lipid membranes: investigation of the cholera toxin-ganglioside interaction by simultaneous impedance spectroscopy and surface plasmon resonance. *Langmuir* 1993, 9:1361-1369.
127. Kjaer K, Als-Nielsen J, Helm CA, Laxhuber LA, Möhwald H. Ordering in Lipid Monolayers Studied by Synchrotron X-Ray Diffraction and Fluorescence Microscopy. *Physical Review Letters* 1987, 58:2224-2227.
128. Kalb E, Engel J, Tamm LK. Binding of proteins to specific target sites in membranes measured by total internal reflection fluorescence microscopy. *Biochemistry* 1990, 29:1607-1613.
129. Johnson SJ, Bayerl TM, McDermott DC, Adam GW, Rennie AR, Thomas RK, Sackmann E. Structure of an adsorbed dimyristoylphosphatidylcholine bilayer measured with specular reflection of neutrons. *Biophysical Journal* 1991, 59:289-294.

130. Brian AA, McConnell HM. Allogeneic stimulation of cytotoxic T cells by supported planar membranes. *Proceedings of the National Academy of Sciences of the United States of America* 1984, 81:6159-6163.
131. Chan PY, Lawrence MB, Dustin ML, Ferguson LM, Golan DE, Springer TA. Influence of receptor lateral mobility on adhesion strengthening between membranes containing LFA-3 and CD2. *The Journal of Cell Biology* 1991, 115:245.
132. Erb E-M, Tangemann K, Bohrmann B, Müller B, Engel J. Integrin αIIbβ3 Reconstituted into Lipid Bilayers Is Nonclustered in Its Activated State but Clusters after Fibrinogen Binding. *Biochemistry* 1997, 36:7395-7402.
133. Kloboucek A, Behrisch A, Faix J, Sackmann E. Adhesion-Induced Receptor Segregation and Adhesion Plaque Formation: A Model Membrane Study. *Biophysical Journal* 1999, 77:2311-2328.
134. Qi SY, Groves JT, Chakraborty AK. Synaptic pattern formation during cellular recognition. *Proceedings of the National Academy of Sciences* 2001, 98:6548.
135. Grakoui A, Bromley SK, Sumen C, Davis MM, Shaw AS, Allen PM, Dustin ML. The Immunological Synapse: A Molecular Machine Controlling T Cell Activation. *Science* 1999, 285:221.
136. Tamm LK, McConnell HM. Supported phospholipid bilayers. *Biophysical Journal* 1985, 47:105-113.
137. Bruinsma R, Behrisch A, Sackmann E. Adhesive switching of membranes: Experiment and theory. *Physical Review E* 2000, 61:4253-4267.
138. Sackmann E, Bruinsma RF. Cell Adhesion as Wetting Transition? *ChemPhysChem* 2002, 3:262-269.
139. Frenkel N, Makky A, Sudji IR, Wink M, Tanaka M. Mechanistic Investigation of Interactions Between Steroidal Saponin Digitonin and Cell Membrane Models. *J. Phys. Chem. B* 2014, 118:14632-14639.
140. Frenkel N, Wallys J, Lippert S, Teubert J, Kaufmann S, Das A, Monroy E, Eickhoff M, Tanaka M. High Precision, Electrochemical Detection of Reversible Binding of Recombinant Proteins on Wide Bandgap GaN Electrodes Functionalized with Biomembrane Models. *Advanced Functional Materials* 2014, 24:4927-4934.
141. Wagner ML, Tamm LK. Reconstituted Syntaxin1A/SNAP25 Interacts with Negatively Charged Lipids as Measured by Lateral Diffusion in Planar Supported Bilayers. *Biophysical Journal* 2001, 81:266-275.
142. Sackmann E, Tanaka M. Supported membranes on soft polymer cushions: fabrication, characterization and applications. *Trends in Biotechnology* 2000, 18:58-64.
143. Knoll W, Frank CW, Heibel C, Naumann R, Offenhäusser A, Rühe J, Schmidt EK, Shen WW, Sinner A. Functional tethered lipid bilayers. *Reviews in Molecular Biotechnology* 2000, 74:137-158.
144. Hassan YI, Zempleni J. Epigenetic Regulation of Chromatin Structure and Gene Function by Biotin1,2. *The Journal of Nutrition* 2006, 136:1763-1765.
145. Burkholder PR, McVeigh I. Synthesis of vitamins by intestinal bacteria. *Proceedings of the National Academy of Sciences of the United States of America* 1942, 28:285.
146. Said HM. Biotin: the forgotten vitamin. 2002.
147. Boenisch T, Henne C. *Handbuch Immunchemische Färbemethoden*: DakoCytomation; 2003.
148. Green NM. AVIDIN. 1. THE USE OF (14-C)BIOTIN FOR KINETIC STUDIES AND FOR ASSAY. *The Biochemical journal* 1963, 89:585-591.
149. Bayer EA, Skutelsky E, Wynne D, Wilchek M. Preparation of ferritin-avidin conjugates by reductive alkylation for use in electron microscopic cytochemistry. *Journal of Histochemistry & Cytochemistry* 1976, 24:933-939.
150. Durance T. Residual avid in activity in cooked egg white assayed with improved sensitivity. *Journal of food science* 1991, 56:707-709.
151. Wilchek M, Bayer EA. A universal affinity column using avidin-biotin technology. *Protein Recognition of Immobilized Ligands* 1989:83-90.

152. Repo S, Paldanius TA, Hytönen VP, Nyholm TK, Halling KK, Huuskonen J, Pentikäinen OT, Rissanen K, Slotte JP, Airenne TT. Binding properties of HABA-type azo derivatives to avidin and avidin-related protein 4. *Chemistry & biology* 2006, 13:1029-1039.
153. Swack JA, Zander GL, Utter MF. Use of avidin-sepharose to lsolate and identify biotin polypeptides from crude extracts. *Analytical Biochemistry* 1978, 87:114-126.
154. Manning J, Pellegrini M, Davidson N. A method for gene enrichment based on the avidin-biotin interaction. Application to the Drosophila ribosomal RNA genes. *Biochemistry* 1977, 16:1364-1370.
155. Raedler J, Sackmann E. On the measurement of weak repulsive and frictional colloidal forces by reflection interference contrast microscopy. *Langmuir* 1992, 8:848-853.
156. Bongrand P. *Physical Basis of Cell-Cell Adhesion*: Boca Raton: CRC Press; 1988.
157. Marra J, Israelachvili J. Direct measurements of forces between phosphatidylcholine and phosphatidylethanolamine bilayers in aqueous electrolyte solutions. *Biochemistry* 1985, 24:4608-4618.
158. Evans E, Needham D. Physical properties of surfactant bilayer membranes: thermal transitions, elasticity, rigidity, cohesion and colloidal interactions. *The Journal of Physical Chemistry* 1987, 91:4219-4228.
159. Filler TJ, Peuker ET. Reflection contrast microscopy (RCM): a forgotten technique? *The Journal of Pathology* 2000, 190:635-638.
160. Limozin L, Sengupta K. Quantitative reflection interference contrast microscopy (RICM) in soft matter and cell adhesion. *ChemPhysChem* 2009, 10:2752-2768.
161. Curtis A. The mechanism of adhesion of cells to glass: a study by interference reflection microscopy. *The Journal of cell biology* 1964, 20:199-215.
162. Albersdörfer A, Sackmann E. Swelling Behavior and Viscoelasticity of Ultrathin Grafted Hyaluronic Acid Films. *Eur. Phys. J. B* 1999, 10:663-672.
163. Monzel C, Veschgini M, Madsen J, Lewis AL, Armes SP, Tanaka M. Fine Adjustment of Interfacial Potential between pH-Responsive Hydrogels and Cell-Sized Particles. *Langmuir* 2015, 31:8689-8696.
164. Higaki Y, Fröhlich B, Yamamoto A, Murakami R, Kaneko M, Takahara A, Tanaka M. Ion-specific modulation of interfacial interaction potentials between solid substrates and cell-sized particles mediated via zwitterionic, super-hydrophilic poly (sulfobetaine) brushes. *The Journal of Physical Chemistry B* 2017, 121:1396-1404.
165. Sengupta K, Limozin L. Adhesion of soft membranes controlled by tension and interfacial polymers. *Physical review letters* 2010, 104:088101.
166. Ploem J. *Reflection-contrast microscopy as a tool for investigation of the attachment of living cells to a glass surface*: Blackwell, Oxford; 1975.
167. Burk AS. Quantifying Adhesion and Morphological Dynamics of Human Hematopoietic Stem and Progenitor Cells on Novel In Vitro Models of Bone Marrow Niche. 2015.
168. Wiegand G, Neumaier KR, Sackmann E. Microinterferometry: three-dimensional reconstruction of surface microtopography for thin-film and wetting studies by reflection interference contrast microscopy (RICM). *Applied Optics* 1998, 37:6892-6905.
169. Amadei F, Fröhlich B, Stremmel W, Tanaka M. Nonclassical Interactions of Phosphatidylcholine with Mucin Protect Intestinal Surfaces: A Microinterferometry Study. *Langmuir* 2018, 34:14046-14057.
170. Reynolds O. An Experimental Investigation of the Circumstances Which Determine Whether the Motion of Water Shall Be Direct or Sinuous, and of the Law of Resistance in Parallel Channels. *Proc. Royal Soc. Lond.* 1883, 35:84-99.
171. Pincus P. Colloid Stabilization with Grafted Polyelectrolytes. *Macromolecules* 1991, 24:2912-2919.
172. Kühner M, Sackmann E. Ultrathin Hydrated Dextran Films Grafted on Glass: Preparation and Characterization of Structural, Viscous, and Elastic Properties by Quantitative Microinterferometry. *Langmuir* 1996, 12:4866-4876.

173. Motomu T, Florian R, Matthias FS, Gerald M, Antero A, Klaus RN, Oliver P, Erich S. Wetting and Dewetting of Extracellular Matrix and Glycocalix Models. *J. Phys. Condens. Matter* 2005, 17:S649.
174. Daillant J, Gibaud A. *X-ray and neutron reflectivity: principles and applications*. Vol. 770: Springer; 2008.
175. Als-Nielsen J, McMorrow D. *Elements of modern X-ray physics*: John Wiley & Sons; 2011.
176. National Aeronautics and Space Administration SMD. X-Rays. Available at: https://web.archive.org/web/20121122024930/http://missionscience.nasa.gov/ems/11_xrays.html. (Accessed Retrieved May 03, 2019)
177. Abuillan W. Fine-Structures, Lateral Correlation and Diffusion of Membrane-Associated Proteins on Biological Membrane Surfaces. 2013.
178. Attwood D, Halbach K, Kim K-J. Tunable coherent X-rays. *Science* 1985, 228:1265-1272.
179. Klein M, Furtak T. Optics, John Wiley Ltd. *New York* 1986:236.
180. Abernathy DL, Grübel G, Brauer S, McNulty I, Stephenson GB, Mochrie SGJ, Sandy AR, Mulders N, Sutton M. Small-Angle X-ray Scattering Using Coherent Undulator Radiation at the ESRF. *Journal of Synchrotron Radiation* 1998, 5:37-47.
181. Duri A, Cipelletti L. Length scale dependence of dynamical heterogeneity in a colloidal fractal gel. *EPL (Europhysics Letters)* 2006, 76:972.
182. Cipelletti L, Ramos L, Manley S, Pitard E, Weitz DA, Pashkovski EE, Johansson M. Universal non-diffusive slow dynamics in aging soft matter. *Faraday Discussions* 2003, 123:237-251.
183. Bouchaud J-P, Pitard E. Anomalous dynamical light scattering in soft glassy gels. *The European Physical Journal E* 2001, 6:231-236.
184. Malik A, Sandy A, Lurio L, Stephenson G, Mochrie S, McNulty I, Sutton M. Coherent X-ray study of fluctuations during domain coarsening. *Physical review letters* 1998, 81:5832.
185. Glenister DA, Salamon KE, Smith K, Beighton D, Keevil CW. Enhanced Growth of Complex Communities of Dental Plaque Bacteria in Mucin-Limited Continuous Culture. *Microbial Ecology in Health and Disease* 1988, 1:31-38.
186. Herrmann M, Schneck E, Gutsmann T, Brandenburg K, Tanaka M. Bacterial lipopolysaccharides form physically cross-linked, two-dimensional gels in the presence of divalent cations. *Soft Matter* 2015, 11:6037-6044.
187. Paques JP, van der Linden E, Sagis LMC, van Rijn CJM. Food-Grade Submicrometer Particles from Salts Prepared Using Ethanol-in-Oil Mixtures. *Journal of Agricultural and Food Chemistry* 2012, 60:8501-8509.
188. Ponchut C, Rigal JM, Clément J, Papillon E, Homs A, Petitdemange S. MAXIPIX, a fast readout photon-counting X-ray area detector for synchrotron applications. *Journal of Instrumentation* 2011, 6:C01069.
189. Cipelletti L, Weitz DA. Ultralow-angle dynamic light scattering with a charge coupled device camera based multispeckle, multitau correlator. *Review of Scientific Instruments* 1999, 70:3214-3221.
190. Bartsch E, Frenz V, Baschnagel J, Schärtl W, Sillescu H. The glass transition dynamics of polymer micronetwork colloids. A mode coupling analysis. *The Journal of Chemical Physics* 1997, 106:3743-3756.
191. Sze A, Erickson D, Ren L, Li D. Zeta-potential measurement using the Smoluchowski equation and the slope of the current–time relationship in electroosmotic flow. *J. Colloid Interf. Sci.* 2003, 261:402-410.
192. Matsuzaki T, Ito H, Chevyreva V, Makky A, Kaufmann S, Okano K, Kobayashi N, Suganuma M, Nakabayashi S, Yoshikawa HY, et al. Adsorption of Galloyl Catechin Aggregates Significantly Modulates Membrane Mechanics in the Absence of Biochemical Cues. *Phys. Chem. Chem. Phys.* 2017, 19:19937-19947.
193. Körner A, Deichmann C, Rossetti FF, Köhler A, Konovalov OV, Wedlich D, Tanaka M. Cell Differentiation of Pluripotent Tissue Sheets Immobilized on Supported Membranes Displaying Cadherin-11. *PLOS ONE* 2013, 8:e54749.

194. Voinova MV, Rodahl M, Jonson M, Kasemo B. Viscoelastic Acoustic Response of Layered Polymer Films at Fluid-Solid Interfaces: Continuum Mechanics Approach. *Phys. Scr.* 1999, 59:391.

195. Oh S, Wilcox M, Pearson JP, Borrós S. Optimal Design for Studying Mucoadhesive Polymers Interaction with Gastric Mucin Using a Quartz Crystal Microbalance with Dissipation (QCM-D): Comparison of Two Different Mucin Origins. *Eur. J. Pharm. Biopharm.* 2015, 96:477-483.

196. Blum H, Beier H, Gross HJ. Improved Silver Staining of Plant Proteins, RNA and DNA in Polyacrylamide Gels. *Electrophoresis* 1987, 8:93-99.

197. Rädler JO, Feder TJ, Strey HH, Sackmann E. Fluctuation Analysis of Tension-Controlled Undulation Forces Between Giant Vesicles and Solid Substrates. *Phys. Rev. E* 1995, 51:4526-4536.

198. Cornish RJ. Flow in a Pipe of Rectangular Cross-Section. *Proc. Royal Soc. Lond. A* 1928, 120:691-700.

199. Alemka A, Clyne M, Shanahan F, Tompkins T, Corcionivoschi N, Bourke B. Probiotic Colonization of the Adherent Mucus Layer of HT29MTXE12 Cells Attenuates *Campylobacter jejuni* Virulence Properties. *Infect. Immun.* 2010, 78:2812-2822.

200. Radmacher M. Measuring the Elastic Properties of Biological Samples with the AFM. *IEEE Eng. Med. Biol.* 1997, 16:47-57.

201. Shoffner SK, Schnell S. Estimation of the lag time in a subsequent monomer addition model for fibril elongation. *Physical Chemistry Chemical Physics* 2016, 18:21259-21268.

202. Bandyopadhyay R. R. Bandyopadhyay, D. Liang, H. Yardimci, DA Sessoms, MA Borthwick, SGJ Mochrie, JL Harden, and RL Leheny, Phys. Rev. Lett. 93, 228302 (2004). *Phys. Rev. Lett.* 2004, 93:228302.

203. Orsi D, Ruta B, Chushkin Y, Pucci A, Ruggeri G, Baldi G, Rimoldi T, Cristofolini L. Controlling the dynamics of a bidimensional gel above and below its percolation transition. *Physical Review E* 2014, 89:042308.

204. Bhattacharyya SM, Bagchi B, Wolynes PG. Subquadratic wavenumber dependence of the structural relaxation of supercooled liquid in the crossover regime. *The Journal of chemical physics* 2010, 132:104503.

205. Vogt BD, Lin EK, Wu W-l, White CC. Effect of Film Thickness on the Validity of the Sauerbrey Equation for Hydrated Polyelectrolyte Films. *J. Phys. Chem. B* 2004, 108:12685-12690.

206. Murugova TN, Balgavy P. Molecular Volumes of DOPC and DOPS in Mixed Bilayers of Multilamellar Vesicles. *Phys. Chem. Chem. Phys.* 2014, 16:18211-18216.

207. Migliorini E, Thakar D, Sadir R, Pleiner T, Baleux F, Lortat-Jacob H, Coche-Guerente L, Richter RP. Well-Defined Biomimetic Surfaces to Characterize Glycosaminoglycan-Mediated Interactions on the Molecular, Supramolecular and Cellular Levels. *Biomaterials* 2014, 35:8903-8915.

208. Livnah O, Bayer EA, Wilchek M, Sussman JL. Three-Dimensional Structures of Avidin and the Avidin-Biotin Complex. *Proc. Natl. Acad. Sci. U S A* 1993, 90:5076-5080.

209. Abuillan W, Vorobiev A, Hartel A, Jones NG, Engstler M, Tanaka M. Quantitative Determination of the Lateral Density and Intermolecular Correlation Between Proteins Anchored on the Membrane Surfaces Using Grazing Incidence Small-Angle X-Ray Scattering and Grazing Incidence X-Ray Fluorescence. *J. Chem. Phys.* 2012, 137:204907-204908.

210. Radicioni G, Cao R, Carpenter J, Ford AA, Wang TT, Li Y, Kesimer M. The Innate Immune Properties of Airway Mucosal Surfaces are Regulated by Dynamic Interactions Between Mucins and Interacting Proteins: the Mucin Interactome. *Mucosal Immunol.* 2016, 9:1442.

211. Wiecinski PN, Metz KM, Mangham AN, Jacobson KH, Hamers RJ, Pedersen JA. Gastrointestinal Biodurability of Engineered Nanoparticles: Development of an *in vitro* Assay. *Nanotoxicol.* 2009, 3:202-214.

212. Helm CA, Knoll W, Israelachvili JN. Measurement of Ligand-Receptor Interactions. *Proc. Natl. Acad. Sci.* 1991, 88:8169-8173.

213. Burk AS, Monzel C, Yoshikawa HY, Wuchter P, Saffrich R, Eckstein V, Tanaka M, Ho AD. Quantifying Adhesion Mechanisms and Dynamics of Human Hematopoietic Stem and Progenitor Cells*. Sci. Rep.* 2015, 5:9370.
214. Eshrati M, Amadei F, Van de Wiele T, Veschgini M, Kaufmann S, Tanaka M. Biopolymer-Based Minimal Formulations Boost Viability and Metabolic Functionality of Probiotics Lactobacillus rhamnosus GG through Gastrointestinal Passage*. Langmuir* 2018, 34:11167-11175.
215. Matos C, de Castro B, Gameiro P, Lima JLFC, Reis S. Zeta-Potential Measurements as a Tool To Quantify the Effect of Charged Drugs on the Surface Potential of Egg Phosphatidylcholine Liposomes*. Langmuir* 2004, 20:369-377.
216. Netz RR, Andelman D. Neutral and Charged Polymers at Interfaces*. Phys. Rep.* 2003, 380:1-95.
217. Tanaka M. Physics of Interactions at Biological and Biomaterial Interfaces*. Curr. Opin. Colloid Interface Sci.* 2013, 18:432-439.
218. Ahrens H, Förster S, Helm CA. Charged Polymer Brushes: Counterion Incorporation and Scaling Relations*. Phys. Rev. Lett.* 1998, 81:4172-4175.
219. Schuster B, Sleytr UB. Relevance of Glycosylation of S-Layer Proteins for Cell Surface Properties*. Acta Biomater.* 2015, 19:149-157.
220. Maiolo D, Del Pino P, Metrangolo P, Parak WJ, Baldelli Bombelli F. Nanomedicine Delivery: Does Protein Corona Route to the Target or Off Road? *Nanomedicine* 2015, 10:3231-3247.
221. Kim HI, Kushmerick JG, Houston JE, Bunker BC. Viscous "interphase" Water Adjacent to Oligo (Ethylene Glycol)-Terminated Monolayers*. Langmuir* 2003, 19:9271-9275.
222. Hayashi T, Tanaka Y, Koide Y, Tanaka M, Hara M. Mechanism Underlying Bioinertness of Self-Assembled Monolayers of Oligo (Ethyleneglycol)-Terminated Alkanethiols on Gold: Protein Adsorption, Platelet Adhesion, and Surface Forces*. Phys. Chem. Chem. Phys.* 2012, 14:10196-10206.
223. Curatolo W, Yau AO, Small DM, Sears B. Lectin-Induced Agglutination of Phospholipid/Glycolipid Vesicles*. Biochemistry* 1978, 17:5740-5744.
224. Geyer A, Gege C, Schmidt RR. Carbohydrate–Carbohydrate Recognition Between LewisX Glycoconjugates*. Angew. Chem. Int. Edit.* 1999, 38:1466-1468.
225. Johansson MEV, Sjovall H, Hansson GC. The Gastrointestinal Mucus System in Health and Disease*. Nat. Rev. Gastroenterol. Hepatol.* 2013, 10:352-361.
226. Sackmann E, Lipowsky R. *Structure and dynamics of membranes*: Elsevier Science; 1995.
227. Bruinsma R, Sackmann E. Bioadhesion and the Dewetting Transition*. CR. Acad. Sci. IV-Phys.* 2001, 2:803-815.
228. Minami T, Tojo H, Shinomura Y, Matsuzawa Y, Okamoto M. Increased Group II Phospholipase A2 in Colonic Mucosa of Patients with Crohn's Disease and Ulcerative Colitis*. Gut* 1994, 35:1593.
229. Gibson PR, Muir JG. Reinforcing the Mucus: a New Therapeutic Approach for Ulcerative Colitis? *Gut* 2005, 54:900-903.
230. Dolan B, Naughton J, Tegtmeyer N, May FEB, Clyne M. The Interaction of Helicobacter pylori with the Adherent Mucus Gel Layer Secreted by Polarized HT29-MTX-E12 Cells*. PLOS ONE* 2012, 7:e47300.
231. Quaroni A, Hochman J. Development of Intestinal Cell Culture Models for Drug Transport and Metabolism Studies*. Adv. Drug Deliv. Rev.* 1996, 22:3-52.
232. Navabi N, McGuckin MA, Lindén SK. Gastrointestinal Cell Lines Form Polarized Epithelia with an Adherent Mucus Layer when Cultured in Semi-Wet Interfaces with Mechanical Stimulation. *PLOS ONE* 2013, 8:e68761.
233. Haase K, Pelling AE. Investigating Cell Mechanics with Atomic Force Microscopy*. J. Royal Soc. Interface* 2015, 12:104.
234. Sunyer R, Trepat X, Fredberg JJ, Farré R, Navajas D. The Temperature Dependence of Cell Mechanics Measured by Atomic Force Microscopy*. Phys. Biol.* 2009, 6:025009.
235. Liévin-Le Moal V, Servin AL. Pathogenesis of Human Enterovirulent Bacteria: Lessons from Cultured, Fully Differentiated Human Colon Cancer Cell Lines*. Microbiol. Mol. Biol. Rev.* 2013, 77:380-439.

236. Lekka M, Pogoda K, Gostek J, Klymenko O, Prauzner-Bechcicki S, Wiltowska-Zuber J, Jaczewska J, Lekki J, Stachura Z. Cancer Cell Recognition – Mechanical Phenotype. *Micron* 2012, 43:1259-1266.

237. Huet G, Kim I, de Bolos C, Lo-Guidice JM, Moreau O, Hemon B, Richet C, Delannoy P, Real FX, Degand P. Characterization of Mucins and Proteoglycans Synthesized by a Mucin-Secreting HT-29 Cell Subpopulation. *J. Cell Sci.* 1995, 108:1275.

238. Lesuffleur T, Barbat A, Dussaulx E, Zweibaum A. Growth Adaptation to Methotrexate of HT-29 Human Colon Carcinoma Cells Is Associated with Their Ability to Differentiate into Columnar Absorptive and Mucus-Secreting Cells. *Cancer Res.* 1990, 50:6334-6343.

239. Hui TH, Zhou ZL, Fong HW, Ngan RKC, Lee TY, Au JSK, Ngan AHW, Yip TTC, Lin Y. Characterizing the Malignancy and Drug Resistance of Cancer Cells from Their Membrane Resealing Response. *Sci. Rep.* 2016, 6:26692.

240. Schimpel C, Werzer O, Fröhlich E, Leitinger G, Absenger-Novak M, Teubl B, Zimmer A, Roblegg E. Atomic Force Microscopy as Analytical Tool to Study Physico-Mechanical Properties of Intestinal Cells. *Beilstein J. Nanotechnol.* 2015, 6:1457-1466.

241. Gopal PK, Prasad J, Smart J, Gill HS. In vitro Adherence Properties of *Lactobacillus rhamnosus* DR20 and *Bifidobacterium lactis* DR10 Strains and Their Antagonistic Activity Against an Enterotoxigenic *Escherichia coli. Int. J. Food Microbiol.* 2001, 67:207-216.

242. Johansson MEV, Ambort D, Pelaseyed T, Schütte A, Gustafsson JK, Ermund A, Subramani DB, Holmén-Larsson JM, Thomsson KA, Bergström JH, et al. Composition and Functional Role of the Mucus Layers in the Intestine. *Cell. Mol. Life Sci.* 2011, 68:3635-3641.

243. Bernet MF, Brassart D, Neeser JR, Servin AL. *Lactobacillus acidophilus* LA 1 Binds to Cultured Human Intestinal Cell Lines and Inhibits Cell Attachment and Cell Invasion by Enterovirulent Bacteria. *Gut* 1994, 35:483-489.